Adaptive Approaches for Fault Detection and Diagnosis With Applications

by

Gang Li

A thesis submitted in partial fulfillment of the requirements for the degree of

Doctor of Philosophy

in

Control Systems

Department of Electrical and Computer Engineering
University of Alberta

Abstract

Adaptive approaches for model-based fault detection, diagnosis and control are the focus of this research. Both analytical and data-driven model-based techniques are studied along with the investigation of their practical applications.

This thesis is organized in two parts. In Part I, adaptive fault estimation (FE) and fault tolerant shape control (FTSC) designs are proposed for stochastic distribution systems. First, an adaptive FE and dynamic output feedback FTSC scheme is designed for a class of nonlinear non-Gaussian stochastic systems subject to time-varying loss of control effectiveness faults, where time-varying faults, Lipschitz nonlinear property and general stochastic characteristics are taken into consideration simultaneously. Then, the FE and FTSC schemes are extended to particle size distribution (PSD) processes subject to simultaneous time-varying actuator and sensor faults. The proposed adaptive FE and FTSC schemes are validated in both simulation and application examples.

In Part II, adaptive data-driven model-based fault detection and diagnosis (FDD) methods are proposed for rotating machinery. First, a novel sinusoidal synthesis based adaptive tracking (SSBAT) technique is proposed based on a data-driven rotating machinery model identified using time-series vibration data and incorporating physical constraints of rotating equipment; the SSBAT model is then used as an adaptive predictor to generate residual for FDD. Then, a minimum entropy deconvolution based sinusoidal synthesis (MEDSS) model is proposed to improve the fault diagnosis performance of the SSBAT scheme; a time-weighted-error Kalman filter is designed to estimate the MEDSS model parameters

adaptively. Both methods are tested and proved to be effective through simulation examples and a practical case study for rubbing fault diagnosis in an industrial steam turbine.

Preface

Chapter 4 of this thesis has been published as G. Li, G. L. McDonald, and Q. Zhao, Sinusoidal synthesis based adaptive tracking for rotating machinery fault detection, *Mechanical Systems and Signal Processing*, vol. 83, pp. 356 - 370, 2017. I was responsible for the analysis and design as well as the manuscript composition. G. L. McDonald assisted with the data collection and data preprocessing. Dr. Q. Zhao was the supervisory author and was involved with concept formation and manuscript composition.

Chapter 5 of this thesis has been published as G. Li and Q. Zhao, Minimum entropy deconvolution optimized sinusoidal synthesis and its application to vibration based fault detection, *Journal of Sound and Vibration*, vol. 390, pp. 218 - 231, 2017. I was responsible for the analysis and design as well as the manuscript composition. Dr. Q. Zhao was the supervisory author and provided suggestions on the results and the manuscript composition.

The ideas, technical derivations, and case studies in Chapters 2 and 3 are my original work, as well as the introduction in Chapter 1.

Acknowledgements

I would like to express my sincere gratitude to my supervisor, Dr. Qing Zhao for her continuous contributions to my research work, and for her motivation, guidance and support. Dr. Zhao steered me in the right direction whenever I ran into a trouble spot or had a question about my research or writing. I am grateful to Dr. Zhao for her support of trips to several international conferences where I shared my research results and met people who were interested in the same topic. I also want to give my gratitude to Dr. Zhao for her understanding and encouragement in my difficult times.

I would like to thank the PhD final examination committee and candidacy examination committee members: Dr. Yang Shi from University of Victoria, Dr. Michael Lipsett and Dr. Xiaodong Wang from Department of Mechanical Engineering, Dr. Tongwen Chen, Dr. Mahdi Tavakoli, Dr. Alan F. Lynch and Dr. Ryan(Yunwei) Li for their comments and suggestions with respect to this thesis.

I am grateful to my academic collaborator, Dr. Tao Li, professor of the School of Information and Control, Nanjing University of Information Science and Technology. I would like to thank Dr. Li for his contribution to the research on stochastic fault tolerant shape control. I wish to thank my colleagues, Mr. Rui Pan and Mr. Geoff L. McDonald, for their contribution to the research on rotating machine modeling.

I must express my deepest gratitude to my parents and to my sister for their unconditional love and support, and continuous encouragement throughout my years of study. A special thanks to my mother for all the sacrifices she has made for me. Last but not the least, I would like to express appreciation to my beloved wife Tuo Liu , who is always there to support me and look after our son Oliver.

Contents

List of Tables

List of Figures

List of Abbreviations

AIC	Akaike information criterion
AO	Adaptive observer
AR	Autoregressive
ARMED	Autoregressive minimum entropy deconvolution
DFT	Discrete Fourier transform
FAFE	Fast adaptive fault estimation
FDD	Fault detection and diagnosis
FDF	Failure detection filter
FDI	Fault detection and isolation
FE	Fault estimation
FTC	Fault-tolerant control
FTSC	Fault-tolerant shape control
LMI	Linear matrix inequality
LOCE	loss of control effectiveness
LS	Least-Squares
LTV	Linear time varying
MED	Minimum entropy deconvolution
MEDSS	Minimum entropy deconvolution based sinusoidal synthesis
MPC	Model predictive control
OT	Order-tracking
PBE	Population balance equation
PCA	Principal component analysis
PDF	Probability density function
PSD	Particle size distribution
RMS	Root mean square
SDC	Stochastic distribution control
SK	Spectral Kurtosis

SMO	Sliding mode observer
SNR	Signal to noise ratio
SS	Sinusoidal synthesis
SSBAT	Sinusoidal synthesis based adaptive tracking
TSA	Time synchronous average
VKF	Vold-Kalman-filter
WFT	Windowed Fourier transform

Chapter 1

Introduction

1.1 Background of Model-Based Fault Detection and Diagnosis (FDD)

The complexity and automation level of industrial systems and processes has been growing rapidly in the past several decades, along with the ever-increasing demands for enhanced performance and reduced operation costs. This trend has made modern systems more vulnerable to system faults or errors than ever. Therefore, one of the most critical issues facing control engineers is the system reliability and safety. As an effective tool to detect system/component malfunctions and further mitigate harmful fault effects, fault detection and diagnosis (FDD), along with fault-tolerant control (FTC), has recently received considerable attention, both in industries and research communities.

Generally, there are three tasks for an FDD scheme: (i) fault detection, which indicates the occurrence of a fault and the time of fault occurrence; (ii) fault isolation, which determines the location and the type of the fault; and (iii) fault identification, which determines the size of the fault. Usually, fault isolation and identification are referred to as fault diagnosis or fault estimation (FE) in literature [1]. FDD approaches can be generally categorized into five classes as [2]: (i) model-based techniques, (ii) hardware redundancy based techniques, (iii) signal processing based techniques, (iv) statistical data based techniques, and (v) artificial intelligence based technique. This thesis is focused on the first category, i.e. model-based FDD.

As one topic closely related to FDD, fault-tolerant control (FTC) is considered to be an important part of reliable and safety control systems. Depending on how the redundancy is used, FTC schemes can be classified as either passive FTC or active FTC. In a passive

FTC, a single controller is designed with consideration of both normal conditions and the expected faults. With this scheme, the system will be robust to the class of faults which have been taken into account in the design step. In contrast, in an active FTC scheme, the information from the monitoring system is utilized to perform FDD. The results are then used to reconfigure the controller or compensate the system, ensuring the stability and certain performance, possibly degraded.

For both FDD and FTC, there is no doubt that an accurate system model representation is crucial. Therefore, for model based FDD and FTC, the first and fundamental step is to obtain a plant model. There are two branches in model based FDD and FTC, namely, first-principles model-based and data-driven model-based. The former one attempts to incorporate physical constitutive relations of the system into a mathematical formulation. On the contrary, data-driven model-based techniques utilize input-output data to identify the system model; they can be beneficial when understanding of first principles of system operation is not straightforward or when the system is so complex that developing an accurate analytical model is prohibitively expensive. Data-driven approaches can often be deployed quickly and cost-effectively. By incorporating partial information of physical mechanism, data-driven model-based techniques are able to provide a sufficient and accurate coverage of system behavior. Both of the analytical model-based and the data-driven model-based FDD are studied in this thesis.

1.1.1 Model-Based FDD

The core idea of model-based FDD techniques is to replace the hardware redundancy by a system model such that process behavior can be reconstructed in an on-line fashion. This system model is referred to as software redundancy as opposed to the hardware redundancy in literature. In practice, the software redundant system model is driven by the same inputs and runs in parallel with the real process. Under fault-free condition, the estimated process variables are expected to follow the measured ones with small errors like white noise. On the contrary, an evident deviation will be observed by the comparison between the estimated and the measured variables if there exists any fault. The result of such comparison, which is called residual, plays a vital role in FDD. Residual generation refers to the procedure of making the estimates of the process variables and then calculating the difference between the measured variables and their estimates [3].

There have been a variety of approaches to model-based fault detection since the early 1970s [4, 5]. The first model-based fault detection method, the so-called failure detection filter (FDF), was proposed by Beard [6] and Jones [7]. Since then, model-based FDD

theories such as diagnostic observer scheme [8], parity space approach [9] and parameter estimation based method [10], have received a wide attention. Especially during the last two decades, research on model-based FDD has undergone extensive development and it now becomes an important branch of automatic control theory [3]. The efficiency of the model-based fault detection technique has been demonstrated by many successful applications in automatic control systems such as vehicle control systems, power systems, process control systems and so on [11].

Since the 1990s, the so-called observer-based fault detection method, among the existing model-based fault detection schemes, has received much attention due to the substantial results on observer design in control theory [12]. The fundamental theory of observer-based approach for fault detection and isolation (FDI) is about constructing a residual signal and determining a residual evaluation function to compare with a predefined threshold. In the literature, results on observer-based FDI approach in time domain and for linear systems are rich [13, 14, 15]. Design of model based FDI can also be done in the frequency domain [16, 17]. In addition, adaptive observer [18, 19, 20] and nonlinear robust observer-based schemes [21, 22] are developed for FDI purposes. It is worth noting that the diagnostic observers used for FDI are different from the well-known state observers. The diagnostic observer design is not focused on state estimation, instead, output estimators are needed that are generally realized as filters [19].

For many systems in industrial processes, modeling from physical principles is usually cumbersome, time-consuming and sometimes not realistic. Moreover, the reliability of the first-principles model-based FDI may be difficult to guarantee. As no technical process can be modeled exactly and there often exist unknown disturbances, the fault message in the residual signal is usually masked by model uncertainties and unknown disturbances. Another challenge facing first-principles model-based approaches is the loss of fidelity over time when a dynamic system experiences variations in operation conditions. To overcome these drawbacks of first-principles model-based approaches and save the effort and time spent in modeling the plant, identified model-based fault detection methods have been widely adopted in recent years [23, 24, 25]. As mentioned above, input-output relationships are required for FDI, which can be obtained directly from the input-output data. Thus, the motivation of data-driven model-based FDI is to bypass the cumbersome, time-consuming and possibly inaccurate modeling process from first-principles, and build an identified model-based on input-output data for fault detection and diagnosis purposes. Because of increased automation level, faster sampling rate and advances in computing, a large amount of data is available on-line. Many researchers have attached great importance to identified model-based methods in diagnosis and prognosis [5, 10, 25, 26]. The Part II

of this thesis is focused on data-driven model-based fault detection and diagnosis.

It is generally difficult to obtain the exact information of the size of a fault from an FDI strategy alone. For this reason, fault estimation scheme is designed to provide an estimate of accurate size and shape of the fault to achieve the required fault diagnosis. Fault estimation, by definition, is the ability to estimate the magnitude of a fault and its time history. So far, various types of fault estimation approaches have been proposed in literature, such as the sliding mode observer (SMO) based techniques [27, 28, 29, 30], the adaptive observer-based approaches [31, 32, 33, 34], the unknown input observer-based approaches [35], and the descriptor observer-based methods [36, 37, 38]. Based on the estimated faults, FTC can be implemented. Compared to a fault detection problem, fault estimation is a more challenging task because it is required to identify the fault type and estimate the size of the fault.

1.1.2 Adaptive Techniques for Fault Detection and Estimation

Since process operation conditions can change due to disturbances and varying environmental conditions, an on-line update of model parameters during process operation is of practical interests. The goal is to gradually change the scope of the system dynamics as new cases and problems emerge, or as more information becomes available. Among the existing adaptive schemes, the recursive technique least squares methods have been well developed and widely applied [39, 40, 41].

In the recent decade, the well-developed adaptive observer theory is successfully applied to FDI, due to its robustness against model uncertainties and sensitivity to faults. This is the result of a reasonable integration and extension of the observer-based and parameter identification-based fault detection schemes. A number of adaptive observer-based FDI approaches have been proposed for the case of linear systems and several results are available [18, 19, 20]. The work in [42, 43] extended the earlier research to the case of nonlinear systems .

Application of advanced adaptive observer techniques to fault identification and estimation was originated in the 1990s [44, 45]. Based on the assumptions of quasi-constant or slowly varying faults, fault estimation was realized successfully and reliably in the early results. Since then, a number of research results have been published. To name a few, the adaptive observer techniques are used for fault estimation in linear time varying (LTV) systems [46], non-linear systems [47, 48, 49, 50], Takagi-Sugeno fuzzy systems [51], stochastic Markovian jumping systems (MJSs)[52, 53], and multi-agent systems [54]. A fast fault estimation scheme was proposed in [31] and it was successfully applied for estimating

time-varying faults.

1.2 FDD and FTC for Stochastic Distribution Systems

In practical applications, almost all control systems are subject to random noises in various forms, such as system parameter variations and sensor noise, etc. Therefore, stochastic systems deserve special attentions in control engineering design. In the existing research work on stochastic systems, linear systems subject to Gaussian noises are mainly considered. However, these assumptions are not realistic for most of the practical systems, where nonlinearities naturally exist and as a result non-Gaussian property exists as well, namely, first or second moments of the output distribution are not sufficient enough to represent all the stochastic properties [55]. In order to handle the nonlinearity and non-Gaussian nature, output distribution shape or probability density function (PDF), rather than output signal itself, is utilized to develop new system representations. This type of systems is referred to as stochastic distribution systems in literature [56, 57]. Control objectives for stochastic distribution systems can be represented by achieving a desirable distribution shape (or PDF) of the system output, which leads to shape control [57, 58, 59, 60, 61] or stochastic distribution control (SDC). Thanks to the improvement in sensing technology, the output distribution or PDFs become measurable [62, 63], and research on SDC has received wide attention and been regarded as a new branch of stochastic control. In literature, B-spline approximation is commonly used to construct the dynamic relationships between the input and the output distribution shapes (or PDF) of stochastic distribution systems. There has been a growing interest in square-root rational B-spline models [64], due to great simplicity resulted from mutually independent weights inherent to the square-root B-spline models. One of the most important advantages of using B-spline approximation is that the distribution shape tracking problem can then be naturally reduced to a tracking problem of the weights in B-spline models.

Nonlinear stochastic shape control also finds its application in the particle size distribution (PSD) problem in many industries, e.g. chemical processes, paper industries, geotechnical engineering processes [58]. In these processes, a controller is formulated in such a way that the controlled output distribution can track the target distributions assuming the availability of particle distribution measurements.

Recently, monitoring techniques are greatly improved by the combination of spectroscopic methods and fiber optics technology like the near infrared spectroscopy (NIRS), which allow for the in-situ and in-line acquisition of process data [65]. Here are some PSD

shape control examples:

- *Crystallizers*: Control the PSD shape to allow pharmaceutical products have the desired physiological effects [66].
- *Emulsion Polymerization Reactors*: Control the PSD shape to ensure the manufacture of coatings, adhesives, pigments and latex paints with the desired physiochemical properties [67].
- *Biochemical Reactors*: Control of the cell PSD shape to increase the production of key metabolites produced by microbial and mammalian cells [68].

Safety and reliability are of paramount importance for general stochastic distribution processes. However, compared to the more conventional state and/or output measurement based control, the research on SDC systems in the existing literature of FDD and FTC is still new and has fewer results. The first attempt was made in [69] by applying standard observer-based fault detection technique to the fault detection of output probability density functions for a retention system in the paper making. In [70], an adaptive fault diagnosis method was provided to estimate the fault for general stochastic systems. In [71], two optimization measures, namely guaranteed cost performance and H_∞ performance, were applied in an optimal FDD scheme for stochastic dynamic systems with time delays. B-spline neural networks and nonlinear filters were used to perform FDD for time-delay SDC systems in [72]. In [73], an FTC scheme was proposed for singular stochastic distribution systems based on an iterative learning observer. In [74], an FD algorithm based on a neural network observer was proposed for stochastic distribution systems, and a PI controller reconfiguration scheme was implemented to achieve fault tolerance.

1.3 Fault Diagnosis for Rotating Components

Rotating machinery has been considered as one of the most important classes of machinery. It is extensively used in the industrialized world, and various application can be found in literature [75]. From the large scale, rotating machines are used in aircraft engines, centrifuges, and marine propulsion systems. They have also enjoyed popularity in household accessories. The correct functioning of rotating systems is of great importance. Failure of rotor components may cause huge economic losses [76]. Moreover, it can endanger human lives or lead to catastrophic consequences [77] [78]. Therefore, it is critical to make sure that the rotating machines operate reliably.

It is well known that rotor systems can exhibit instability for large angular velocities due to internal damping, unbalanced weight, or imperfect lubrication in the rotor bearings [79]. Early detection of faults in the full speed operating phase is very crucial for these machines due to safety concerns. Even for the normal operation, significant vibration may take place during start-up and coast-down processes as the rotational speed goes through critical speeds corresponding to the vibration modes of the system.

Excessive vibration cannot be avoided even with the best design practices. Since many rotor vibration causes are so subtle and pervasive, a vibration model of high fidelity is desirable. There are mainly two different types of models to describe the vibration of the rotating machine: theoretical model based on first-principle laws and data-driven model based on input-output data. The former is focused on building a model which describes machine dynamics and structural behavior. Physical modeling methods include lumped-parameter models (e.g. transfer matrix based) [80, 81, 82] , and more commonly used, distributed-parameter model approximation based methods (e.g. finite element models) [75, 83]. However, the physical model may be too complex to use for the complicated machine, especially when describing nonlinear behaviors and when the model parameters are varying along the rotating speed. Data-driven modeling can make full use of the vibration data and significantly simplify the model. Moreover, it can be updated on-line to adapt to the changing condition.

With the development of miniature sensors, wireless communication, and high-efficiency computing techniques, data-driven methods based on time-series vibration signal become more popular and applicable in machine fault diagnosis applications [84]. Autoregressive (AR) model is a commonly used data-driven model, which is usually a linear model identified from the signal under no-fault condition. An accurate AR model can reflect the characteristics of a dynamic system [78][85][86], and the model parameters carry important information of the system condition. The residual between predicted value by the AR model and measured value is well-suited to extract features associated with a vibration fault. AR models are data driven in nature so that faults can be detected or even isolated without knowledge about the physical model of the system. On the other hand, AR models may be of high dimensions. For a vibration signal composed of M sinusoids, at least a $2M$ order model is shown to be suitable [78]. In addition, the AR method normally requires a priori knowledge of the vibration under no-fault conditions for data-fitting.

Over the past two decades, the order-tracking (OT) technique has been actively researched. The conventional order tracking approaches use orders (i.e. multiples of the rotating speed) as the frequency base [87], which are mainly based on Fourier analysis, such as windowed Fourier transform (WFT) and the resampling methods [87][88]. These

approaches have limited resolution in some situations and suffer from a number of shortcomings. In particular, they are ineffective when there exists multiple components rotating at independent speeds. For performance improvement, model-based methods have been proposed, where OT problems are formulated based on state space models. A well-known scheme is Vold-Kalman-filter(VKF) OT [89][90][91], in which the order amplitudes are calculated off-line using a least-squares approach. Therefore, the VKF OT method is generally implemented as a post-processing scheme. Both the conventional OT and the model based OT methods require information of shaft speed. Gabor OT is another technique which can extract specific order components in addition to characterizing the processed signal in rpm-frequency domain [92]. However, The Gabor OT can be used for applications where rotational speed information is not available.

Linear models are preferably identified in data-driven methods to conduct fault detection and fault diagnosis. However, it can be inappropriate when dealing with nonlinear and multi-mode processes, where it is likely leading to an FDD method with poor performance; also, the process operation conditions and the environment around the process under monitoring may change with time. In order to handle the time varying process behavior, an adaptive update of the model parameters is of paramount importance in data-driven FDD [93, 94, 95]. Inspired by the known adaptive observer scheme in the control theory, adaptive data-driven model-based FDD technique provides an efficient and powerful tool to handle FDD in highly dynamic systems and control loops, which are generally located at the process level. Among the existing adaptive schemes, the recursive technique has been well developed and widely applied to data-driven models. However, it is worth mentioning that in the existing literature, the convergence or stability properties of recursive and adaptive data-driven FDD methods have not received enough attention, while they actually play a central role when a dynamic process is under consideration and a fault diagnostic observer is applied.

1.4 Summary of Contributions

The main results of this thesis can be organized into two parts. New results of adaptive FDD and FTC for stochastic distribution system based on the analytical model is given in Part I, which consists of Chapter 2 and Chapter 3. Adaptive FDD for rotating machinery based on the data-driven model are illustrated in Part II, which consists of Chapter 4 and Chapter 5.

PART I. Adaptive FDD and FTC for Stochastic Distribution Systems

Chapter 2 studies the problem of adaptive fault estimation and fault tolerant control for a class of nonlinear non-Gaussian stochastic systems subject to time-varying loss of control effectiveness faults. The output distribution, rather than the system output signal itself, is adopted for FDD and FTC, and square root rational B-spline approximation is used to fit the distribution shape. A unified framework is proposed, where time-varying faults, Lipschitz nonlinear property and general stochastic characteristics are taken into consideration. Both the states and faults are simultaneously estimated in an adaptive observer. Then, a fault tolerant shape controller is formulated to compensate for the faults and realize stochastic output distribution tracking. Both the fault estimation and the fault tolerant control schemes are designed based on linear matrix inequality (LMI) technique. Satisfactory performance is achieved in a numerical simulation example; further, the proposed scheme is successfully tested in a practical example of soil particle gradation control in the geotechnical application.

Chapter 3 investigates the problem of fault-tolerant shape control for particle size distribution (PSD) process subject to simultaneous time-varying actuator and sensor faults. Actuator and sensor faults are taken into consideration in a unified framework based on adaptive observer (AO) technique. An innovative on-line fault estimation scheme is proposed for simultaneous actuator fault and sensor fault estimation. Then an augmented controller based on the virtual actuator and virtual sensor techniques is designed to compensate for the faults and further realize PSD shape tracking. A simulation example of emulsion polymerization is used to validate the proposed scheme and satisfactory performance is obtained.

PART II. Adaptive FDD for Rotating Machinery

Chapter 4 presents a novel sinusoidal synthesis based adaptive tracking (SSBAT) technique for vibration-based rotating machinery fault detection and diagnosis. The proposed SSBAT algorithm is an adaptive data-driven model-based FDD technique that takes advantage of the sinusoidal nature of vibration signals and transfers the nonlinear problem into a linear adaptive problem in the time domain based on a state-space realization. It has low computation burden and does not need a priori knowledge of the machine under the no-fault condition which makes the algorithm ideal for on-line fault detection. A modified Least-Squares (LS) algorithm is adopted to estimate the model parameters. Signal tracking is then realized by applying adaptive sinusoidal synthesis to the vibration signal. In addition to tracking, the proposed data-driven model is mainly used as an adaptive predictor. The health condition of the rotating machine is monitored by checking the residual between the predicted and measured signals. The convergence of the parameter estimation

and the stability of entire system are proved. The method is validated using both numerical simulation and practical application data.

In Chapter 5, a minimum entropy deconvolution based sinusoidal synthesis (MEDSS) model is proposed to improve the FDD performance of the regular sinusoidal synthesis (SS) method in Chapter 4. The minimum entropy deconvolution (MED) technique is used to optimize the SS filter during the model construction process by taking phase information of the harmonic components into consideration, due to the fact that phase relationships are important in differentiating noise from characteristic impulsive fault signatures. A time-weighted-error Kalman filter is used to estimate the MEDSS model parameters adaptively. Three simulation examples and a practical application case study are provided to illustrate the effectiveness of the proposed method. The regular SS method and the autoregressive MED (ARMED) method are also implemented for comparison purposes.

Part I

Adaptive FDD and FTC for Stochastic Distribution Systems

Most of the existing observer-based FDD results in literature for stochastic systems are based on Gaussian assumption, and thus, the optimization objective is naturally focused on first and second statistical moments, i.e. mean and variance. However, due to the presence of nonlinearities, hardly any variables strictly obey a Gaussian distribution in practice. Meanwhile, conventional FE methods are generally designed based on the input-output mathematical models, where output signals are normally required. These limitations make it invalid to apply conventional FDD and FE methods to stochastic distribution systems due to their nonlinearity nature and the fact that output distributions or PDFs, rather than output signal itself, can be measured [73]. Therefore, new observer-based FDD design algorithms are required for general stochastic systems using the output stochastic distributions.

In this part, the stochastic distribution system model is firstly characterized using B-spline approximation following a two-step procedure for further FDD and FTC scheme design. In the first step, B-spline based method is used to approximate a general stochastic distribution (Gaussian or non-Gaussian); the output distributions or PDFs of the system are expected to be represented by the weight dynamics corresponding to some basis functions. In the second step, a further dynamical model is established to relate system input and the dynamical weight vector of the B-spline expansion. Nonlinear weight dynamical models are considered instead of linear ones in this part.

In Chapter 2, an innovative fault tolerant shape control (FTSC) scheme based on output feedback is proposed. A specific type of actuator faults, namely, loss of control effectiveness (LOCE) faults, are considered in a nonlinear non-Gaussian stochastic process. A fast adaptive fault estimation (FAFE) algorithm is designed considering time-varying LOCE faults and the nonlinear effect. Based on the estimation results, a dynamic output feedback FTSC scheme is proposed such that the resulting closed-loop tracking system is stable and an optimized control performance is guaranteed.

Chapter 3 presents an FTSC scheme based on adaptive FE for more general fault scenarios. An innovative adaptive observer-based FE algorithm is designed to simultaneously estimate the actuator and sensor faults for stochastic distribution control systems. The shape control strategy is further introduced in the application of PSD distribution control.

Notation: $\mathbb{R}$ is the set of real numbers. $P > 0$ denotes that P is a symmetric positive definite matrix. $\|\cdot\|$ denotes the Euclidean norm of a vector or the spectral norm of a matrix. $\lambda_{max}(A)$ and $\lambda_{min}(A)$ represent the maximum and minimum eigenvalues of matrix A, respectively. In LMIs, "$*$" represents a term that is induced by symmetry. The superscripts "$\top$" and "-1" stand for matrix transposition and matrix inverse, respectively. Matrices, if their dimensions are not explicitly stated, are assumed to be compatible with related algebraic operations.

Chapter 2

Adaptive Fault-Tolerant Shape Control for Nonlinear Lipschitz Stochastic Distribution Systems

2.1 Introduction

Compared to the more conventional state and/or output measurement based control, in the existing literature on fault estimation and fault-tolerant control, the research on shape control systems with Lipschitz nonlinear and general stochastic characteristics is still new. In [58], a fault-tolerant stochastic shape control scheme based on adaptive control compensation for stochastic distribution systems was proposed. A specific type of actuator faults, namely the loss of control effectiveness (LOCE), was considered. However, it was assumed all states available in the work, which is a strong limitation in many control problems. Also, the nonlinear effects were assumed to be known, which is not practical in some applications. Moreover, in that work, the time-varying faults were not considered, which means all the faults are assumed to be constants or slowly changing.

To improve the existing results, this chapter aims to provide an innovative fault-tolerant shape control scheme based on output feedback. The main difficulty in this study is to estimate and accommodate the time varying LOCE faults in a nonlinear non-Gaussian stochastic process. In this chapter, a new fast adaptive fault estimation (FAFE) algorithm is proposed considering time-varying LOCE faults and the nonlinear effect. Based on the estimation results, a dynamic output feedback fault-tolerant shape control (FTSC) scheme

is proposed such that the resulting closed-loop tracking system is stable and an optimized control performance is guaranteed.

The remainder of this chapter is organized as follows: Section 2.2 provides some preliminary results. The adaptive observer-based fault estimation and the dynamic output feedback FTSC are presented in Section 2.3 and Section 2.4, respectively, as the main results. In Section 2.5, a numerical example and a practical application example of soil particle gradation control in the geotechnical application are provided to demonstrate the feasibility of the proposed approach. Finally, the conclusion is drawn in Section 2.6.

2.2 Preliminaries and Problem Formulation

2.2.1 Distribution Approximation With B-spline Functions

For a dynamic stochastic system, denote $u(t)$ as the control input, and $y(t) \in [\alpha,\ \beta]$ as the output at time t. Assume $y(t)$ is uniformly bounded. With the input $u(t)$, the conditional probability P of the output $y(t) \in [\alpha,\ \gamma]$ $(\alpha \leq \gamma \leq \beta)$, at time t, is defined by,

$$P(\alpha \leq y(t) \leq \gamma | u(t)) = \int_{\alpha}^{\gamma} \rho_{y|u}(\eta,\ t) d\eta, \tag{2.1}$$

where $\rho_{y|u}(\eta,\ t)$ denotes the PDF of $y(t) = \eta$, and η is the specific output value. For simplicity, $\rho_u(\eta)$ and $\rho_u(\eta,\ t)$ are used by dropping the subscript y. The output PDF $\rho_u(\eta)$ is assumed to be measurable, continuous and bounded (see [64] and references therein). In many engineering applications, on-line measurement of the distribution of output variables is essential and can be achieved by using proper instrumentation [65, 96, 97].

The commonly adopted square-root rational B-spline model is proposed here to approximate PDF $\rho_u(\eta)$ [64]

$$\sqrt{\rho_u(\eta)} = \frac{\sum_{i=1}^{n} \omega_i \Gamma_i(\eta)}{\sqrt{\sum_{i=1,j=1}^{n} \omega_i \omega_j \int_{\alpha}^{\beta} \Gamma_i(\eta)\Gamma_j(\eta) d\eta}} = \frac{\Gamma(\eta)\omega}{\sqrt{\omega^{\top}\Gamma_f \omega}}, \quad \forall \eta \in [\alpha,\ \beta], \tag{2.2}$$

where $\Gamma(\eta) = [\Gamma_1(\eta), \cdots, \Gamma_n(\eta)]$, $\Gamma_i(\eta) \geq 0$, is the pre-specified basis function. $\Gamma_f = \int_{\alpha}^{\beta} \Gamma^{\top}(\eta)\Gamma(\eta) d\eta$, and $\omega = [\omega_1, \cdots, \omega_n]^{\top}$, represents the corresponding weight coefficient vector. Here $\omega_i \geq 0$, $(i = 1, ..., n)$ is independent from each other. They are called pseudo weights as they have no physical meanings and are only used to form the desirable PDFs. A preliminary study [98] has shown that the output PDF function can be approximated by Eq.(2.2) to a desired accuracy.

2.2.2 System Model With LOCE Faults

In this thesis, using the square-root rational B-spline approximation model for the output distribution, the whole dynamic system can be characterized by the model Σ_1 in (2.3). Firstly, the dynamic relationship between the input $u(t)$ and the measured pseudo weights $\omega(t)$ is characterized. Then the output PDF $\sqrt{\rho_u(\eta,\, t)}$ is determined based on the output pseudo weights.

$$\Sigma_1 : \begin{cases} \dot{x}(t) = Ax(t) + Gg(x(t)) + BF(t)u(t) \\ \omega(t) = Cx(t) \\ \sqrt{\rho_u(\eta,\, t)} = \frac{\Gamma(\eta)\omega(t)}{\sqrt{\omega^\top(t)\Gamma_f\omega(t)}} \end{cases}, \tag{2.3}$$

where $x(t) \in \mathbb{R}^m$ is the unmeasurable state vector, $\omega(t) \in \mathbb{R}^n$ is the measurable output vector. $u(t) \in \mathbb{R}^p$ is the control input vector. $A \in \mathbb{R}^{m\times m}$, $G \in \mathbb{R}^{m\times m}$, $B \in \mathbb{R}^{m\times p}$, $C \in \mathbb{R}^{n\times m}$ are the known matrices. Herein the control effectiveness factor $F(t) \in \mathbb{R}^{p\times p}$ is described by the following diagonal matrix form:

$$\begin{aligned} F(t) &= \mathrm{diag}\{f_1(t),\, f_2(t), \ldots, f_p(t)\}, \\ f_i(t) &\in [\underline{f}_i\ \overline{f}_i],\ i = 1, 2 \ldots, p,\ 0 < \underline{f}_i \le \overline{f}_i \le 1 \end{aligned} \tag{2.4}$$

where p is the number of inputs, $f_i(t)$ represents the effectiveness loss of the ith actuator channel at time t. $\underline{f}_i$ and $\overline{f}_i$ represent the known lower and upper bounds of $f_i(t)$, respectively.

Remark 2.2.1 *It should be noted that the assumption* $0 < \underline{f}_i \le \overline{f}_i \le 1$ *is mainly for describing the loss of control effectiveness. The fault-free condition can be represented with* $\underline{f}_i = \overline{f}_i = 1$*, while* $f_i = 0$ *represents a total failure (complete loss) of the ith actuator. When* $0 < f_i < 1$*, the ith actuator is considered to be partial loss of control effectiveness. For simplicity, the complete loss condition is not considered in this work.*

Assumption 2.2.1 *The nonlinear function* $g(x(t)) \in \mathbb{R}^m$ *is assumed to be Lipschitz about x uniformly, that is:*

$$\begin{cases} g(0) = 0 \\ ||g(x(t_1)) - g(x(t_2))||_2 \le ||l_f[x(t_1) - x(t_2)]||_2 \end{cases} \tag{2.5}$$

for any $x(t_1)$, $x(t_2) \in \mathbb{R}^m$*, where* l_f *is a Lipschitz constant. Moreover, it is assumed that the corresponding coefficient matrix* $G > 0$*.*

Assumption 2.2.2 *All pairs $(A, BF(t))$ are uniformly completely controllable for all the LOCE faults $F(t)$ under consideration.*

Assumption 2.2.3 *The pair (A, C) is observable.*

Assumption 2.2.4 *The LOCE faults $F(t)$ are differentiable, and $\| \dot{F}(t) \|$ is bounded as $\| \dot{F}(t) \| \leq f_m I$, where f_m is a positive constant and I is an identity matrix.*

Assumption 2.2.5 *The input vector $u_i(t), i = 1, \ldots, p$ satisfies the persistent excitation condition. It means that there exist scalars $\mu_1 > 0$ and $\mu_2 > 0$, such that for any time t and time constant t_0, the following condition holds [32]:*

$$\mu_1 \leq \int_t^{t+t_0} u_i(\tau) u_i(\tau) d\tau \leq \mu_2. \tag{2.6}$$

It can be clearly seen that for the actuator faults considered in this chapter, the control effectiveness matrix $F(t)$ is naturally a diagonal matrix. This is consistent with the fault-free case, where $F(t) = I$ is an identity matrix. Such a formulation can cover several fault cases: (1) At each time only one $f_i(t)$ changes, meaning that only one actuator is faulty; (2) when one fault affects different actuators, for example, when several actuators have control effectiveness losses at the same time, such a case is modeled as simultaneous changes in several factors $f_i(t)$ (from their nominal value of 1) and these changes can be same or different, constant or time-varying. It is worthwhile to note that, using the model Σ_1 in (2.3), uncertainties in B matrix can also be handled, which is also pointed out in *Remark* 3 of [58] .

2.2.3 Control Objectives

The target PDF distribution can be approximated as:

$$\sqrt{\rho^*(\eta, t)} = \frac{\Gamma(\eta)\omega_g(t)}{\sqrt{\omega_g^\top(t)\Gamma_f \omega_g(t)}}, \ \forall \eta \in [\alpha, \ \beta] \tag{2.7}$$

where $\omega_g(t)$ is the vector of target pseudo weights corresponding to the given B-spline basis function $\Gamma(\eta)$. Therefore, the shape control objective is simplified to find the control input $u(t)$ such that $\rho_u(\eta, t)$ follows $\rho^*(\eta, t)$. If $e_\omega(t) = \omega(t) - \omega_g(t) \to 0$, then $\sqrt{\rho_u(\eta, t)} - \sqrt{\rho^*(\eta, t)} \to 0$. The considered FTSC can be formulated as the tracking of $\omega_g(t)$.

The optimal controller is designed by minimizing the upper bound of the following cost function

$$J_t = \int_0^\infty [\xi^\top(t) Z_1 \xi(t) + x^\top(t) Z_2 x(t) + u^\top(t) Z_3 u(t)] \, dt, \tag{2.8}$$

where $\xi(t) = \int_0^t (\omega(\tau) - \omega_g(\tau))d\tau$, $Z_1 > 0$, $Z_2 > 0$ and $Z_3 > 0$ ($Z_1 \in \mathbb{R}^{n\times n}, Z_2 \in \mathbb{R}^{m\times m}$ and $Z_3 \in \mathbb{R}^{p\times p}$).

2.3 Adaptive Fault Estimation

In this section, a novel fast adaptive fault estimation algorithm is presented considering the time-varying LOCE faults. In addition to the pure integral term in conventional adaptive fault estimation method, a proportional term is included in the fault estimation process. Hence, the FAFE algorithm has a faster convergence rate and is appropriate for time-varying LOCE fault estimation.

Let $\hat{x}(t), \hat{F}(t)$ and $\hat{\omega}(t)$ be the estimates of the states, faults and output, respectively. $L \in \mathbb{R}^{m\times n}$ is the observer gain matrix. The fault estimation observer is obtained:

$$\Sigma_2 : \begin{cases} \dot{\hat{x}}(t) = A\hat{x}(t) + Gg(\hat{x}(t)) + B\hat{F}(t)u(t) - L(\hat{\omega}(t) - \omega(t)) \\ \hat{\omega}(t) = C\hat{x}(t) \end{cases}. \tag{2.9}$$

Denote $e_x(t) = \hat{x} - x$, $e_F(t) = \hat{F}(t) - F(t)$, $\dot{e}_F(t) = \dot{\hat{F}}(t) - \dot{F}(t)$, $e_\omega(t) = \hat{\omega}(t) - \omega(t) = Ce_x(t)$, and $g_e(t) = g(\hat{x}(t)) - g(x(t))$. Then the error equation between the system Σ_1 in (2.3) and the observer Σ_2 in (2.9) is described as:

$$\dot{e}_x(t) = (A - LC)e_x(t) + Gg_e(t) + Be_F(t)u(t). \tag{2.10}$$

Lemma 2.3.1 *For a given positive scalar μ_0 and a symmetric positive definite matrix $R_0 \in \mathbb{R}^{r_0\times r_0}$, the following conditions holds [31]:*

$$2a^\top b \le \frac{1}{\mu_0} a^\top R_0 a + \mu_0 b^\top R_0^{-1} b, \tag{2.11}$$

where $a, b \in \mathbb{R}^{r_0}$.

Based on *Lemma* 2.3.1, *Theorem* 2.3.1 is given to provide the main results for the on-line estimation of states and faults. Then, both the estimated states and time-varying faults will be adopted to carry out fault-tolerant stochastic shape control in the following section.

Theorem 2.3.1 *For the error system (2.10), given small positive scalar $\mu > 0$ and $v > 0$, if there exist symmetric positive definite matrices $P_1 \in \mathbb{R}^{m\times m}$, $P_2 \in \mathbb{R}^{p\times p}$, $R \in \mathbb{R}^{p\times n}$, and any matrix $M \in \mathbb{R}^{m\times n}$ such that the following optimization problem exists an solution*

$$\min_{P_1, P_2, R, M} \quad \sigma \tag{2.12}$$

subject to the following matrix inequalities

$$\Omega_1 = \begin{bmatrix} \sigma I & P_1 B - C^\top R^\top \\ (P_1 B - C^\top R^\top)^\top & \sigma I \end{bmatrix} > 0, \tag{2.13}$$

and

$$\Omega_2 = \begin{bmatrix} \Delta_1 & P_1 G & -vA^\top P_1 B + vC^\top M^\top B \\ * & -I & -vG^\top P_1 B \\ * & * & -2vB^\top P_1 B + \frac{1}{\mu} P_2 \end{bmatrix} < 0, \tag{2.14}$$

where $\Delta_1 = P_1 A + A^\top P_1 - MC - C^\top M^\top + l_f^2 I_m$, $M = P_1 L$, *then the following adaptive estimation algorithm:*

$$\dot{\hat{f}}_i(t) \quad = Proj_{[\underline{f}_i \ \overline{f}_i]} \{ -p_{3i} R_i [v\dot{e}_\omega(t) + e_\omega(t)] u_i(t) \} \tag{2.15}$$

can render $e_x(t)$ *and* $e_f(t)$ *uniformly ultimately bounded so that the error system is stabilized, where* $Proj_{[\underline{f}_i \ \overline{f}_i]}$ *represents the projection operator to project the estimated* $\dot{\hat{f}}_i(t)$ *to the interval* $[\underline{f}_i \ \overline{f}_i]$. R_i *is the ith row of* R. u_i *is the ith input channel and* $p_{3i} > 0$ *is the learning rate for the ith fault.*

Proof. The following Lyapunov candidate is chosen here:

$$V_e(t) = e_x^\top(t) P_1 e_x(t) + trace[e_F(t) P_3^{-1} e_F(t)], \tag{2.16}$$

where $P_3 = diag(p_{31}, p_{32}, \ldots, p_{3p})$.

According to (2.10) and (2.15), the derivative along the trajectory of the state error (2.10) can be written as

$$\begin{aligned} \dot{V}_e(t) &= 2e_x^\top(t) P_1 [(A - LC) e_x(t) + G g_e(t) + B e_F(t) u(t)] \\ &\quad + 2trace(e_F(t) P_3^{-1} [\dot{\hat{F}}(t) - \dot{F}(t)]) \\ &= 2e_x^\top(t) P_1 [(A - LC) e_x(t) + G g_e(t) + B e_F(t) u(t)] \\ &\quad - 2trace[v e_F(t) RC\dot{e}_x(t) u^\top(t)] - 2trace[e_F(t) RC e_x(t) u^\top(t)] \\ &\quad - 2trace[e_F(t) P_3^{-1} \dot{F}(t)]. \end{aligned} \tag{2.17}$$

As assumed in (2.5), $\| g(x_1(t)) - g(x_2(t)) \|_2 \leq \| l_f(x_1(t) - x_2(t)) \|_2$. Therefore,

$$\| l_f e_x(t) \|^2 - \| g_e(t) \|^2 \geq 0. \tag{2.18}$$

Hence,

$$\begin{aligned}\dot{V}_e(t) \leq & 2e_x^\top(t)P_1[(A-LC)e_x(t)+Gg_e(t)+Be_F(t)u(t)] \\ & -2trace[ve_F(t)RC\dot{e}_x(t)u^\top(t)]-2trace[e_F(t)RCe_x(t)u^\top(t)] \\ & -2trace[e_F(t)P_3^{-1}\dot{F}(t)]+e_x^\top(t)l_f^\top l_f e_x(t)-g_e^\top(t)g_e(t).\end{aligned} \tag{2.19}$$

Let

$$P_1B = C^\top R^\top. \tag{2.20}$$

Then

$$\begin{aligned}2trace[ve_F(t)RC\dot{e}_x(t)u^\top(t)] =& 2trace[vu^\top(t)e_F(t)RC\dot{e}_x(t)] \\ =& 2v\dot{e}_x^\top(t)P_1Be_F(t)u(t).\end{aligned} \tag{2.21}$$

Similarly,

$$2trace[e_F(t)RCe_x(t)u^\top(t)] = 2e_x^\top(t)P_1Be_F(t)u(t). \tag{2.22}$$

Eq. (2.20) represents an equality constraint that is difficulty to satisfy together with the condition (2.14). Alternatively, it can be approximated in the LMI form of minimizing σ subject to the following inequality[31]:

$$\begin{bmatrix} \sigma I & P_1B-C^\top R^\top \\ (P_1B-C^\top R^\top)^\top & \sigma I \end{bmatrix} > 0. \tag{2.23}$$

Then Eq. (2.19) becomes:

$$\begin{aligned}\dot{V}_e(t) \leq & 2e_x^\top(t)P_1[(A-LC)e_x(t)+Gg_e(t)]-2v\dot{e}_x^\top(t)P_1Be_F(t)u(t) \\ & -2trace[e_F(t)P_3^{-1}\dot{F}(t)]+e_x^\top(t)l_f^\top l_f e_x(t)-g_e^\top(t)g_e(t).\end{aligned} \tag{2.24}$$

From *Lemma* 2.3.1 and *Assumption* 2.2.4, the following can be derived:

$$\begin{aligned}-2trace[e_F(t)P_3^{-1}\dot{F}(t)] \leq & \frac{1}{\mu}(-(e_F(t)u(t))\top(U^{-1}P_4U^{-1})(-e_F(t)u(t))) \\ & +\mu[P_3^{-1}\dot{F}(t)u(t)]^\top(U^{-1}P_4U^{-1})^{-1}P_3^{-1}\dot{F}(t)u(t) \\ & \leq \frac{1}{\mu}[e_F(t)u(t)]^\top P_2[e_F(t)u(t)]+\mu f_m^2\bar{u}^2\lambda_{max}[(P_3^{-1})^\top P_2^{-1}P_3^{-1}],\end{aligned} \tag{2.25}$$

where $P_2 = U^{-1}P_4U^{-1}$, $U = diag(\underline{u},\ldots,\underline{u})$, $\underline{u}$ and $\bar{u}$ are the minimum and maximum constant value of the input among all the input channels, respectively. $\lambda_{max}[(P_3^{-1})^\top P_2^{-1}P_3^{-1}]$ is

the maximum eigenvalue of $[(P_3^{-1})^\top P_2^{-1} P_3^{-1}]$. Then, Eq. (2.24) becomes:

$$\begin{aligned}\dot{V}_e(t) \leq & 2e_x^\top(t)P_1[(A-LC)e_x(t)+Gg_e(t)] - 2ve_x^\top(t)(A-LC)^\top P_1 B e_F(t)u(t) \\ & - 2vg_e^\top(t)G^\top P_1 B e_F(t)u(t) - 2vu^\top(t)e_F(t)B^\top P_1 B e_F(t)u(t) \\ & + \frac{1}{\mu}[e_F(t)u(t)]^\top P_2[e_F(t)u(t)] + \mu f_m^2 \bar{u}^2 \lambda_{max}[(P_3^{-1})^\top P_2^{-1} P_3^{-1}] \\ & + e_x^\top(t)l_f^\top l_f e_x(t) - g_e^\top(t)g_e(t) \\ = & \bar{e}(t)^\top \Omega_2 \bar{e}(t) + \mu f_m^2 \bar{u}^2 \lambda_{max}[(P_3^{-1})^\top P_2^{-1} P_3^{-1}],\end{aligned} \tag{2.26}$$

where $\bar{e}(t) = \begin{bmatrix} e_x^\top(t) & g_e^\top(t) & u^\top(t)e_F(t) \end{bmatrix}^\top$.

If $\Omega_2 < 0$,we can have:

$$\dot{V}_e(t) < -\lambda_{min}(-\Omega_2)||\bar{e}(t)||^2 + \mu f_m^2 \bar{u}^2 \lambda_{max}[(P_3^{-1})^\top P_2^{-1} P_3^{-1}] \quad , \tag{2.27}$$

where $\lambda_{min}(-\Omega_2)$ denotes the minimum eigenvalue of $[-\Omega_2]$. Therefore, $\dot{V}_e(t) < 0$ for

$$\lambda_{min}(-\Omega_2)||\bar{e}(t)||^2 > \mu f_m^2 \bar{u}^2 \lambda_{max}[(P_3^{-1})^\top P_2^{-1} P_3^{-1}].$$

It means the estimation will always converge until $||\bar{e}(t)||^2$ arrives at

$$\mu f_m^2 \bar{u}^2 \lambda_{max}[(P_3^{-1})^\top P_2^{-1} P_3^{-1}]/\lambda_{min}(-\Omega_2),$$

which means the estimation errors of both the states and faults will be uniformly bounded. This is the end of the proof. ■

2.4 Adaptive Fault-Tolerant Control

In this section, a dynamic output feedback fault-tolerant shape control scheme for the nonlinear non-Gaussian stochastic distribution system is proposed. Let $\bar{x}(t) = [\xi^\top(t)\ x^\top(t)]^\top$, where $\xi(t)$ is defined in (2.8). We have the following augmented system Σ_3:

$$\Sigma_3 : \begin{cases} \dot{\bar{x}}(t) = \bar{A}\bar{x}(t) + \bar{G}g(x(t)) + \bar{B}F(t)u(t) + \bar{H}\omega_g(t) \\ \omega(t) = \bar{C}\bar{x} \end{cases}, \tag{2.28}$$

where $\bar{A} \in \mathbb{R}^{(m+n)\times(m+n)}, \bar{G} \in \mathbb{R}^{(m+n)\times m}, \bar{B} \in \mathbb{R}^{(m+n)\times p}, \bar{H} \in \mathbb{R}^{(m+n)\times n}, \bar{C} \in \mathbb{R}^{n\times(m+n)}$. These matrices can be described as follows,

$$\bar{A} = \begin{bmatrix} 0 & C \\ 0 & A \end{bmatrix}, \bar{G} = \begin{bmatrix} 0 \\ G \end{bmatrix}, \bar{B} = \begin{bmatrix} 0 \\ B \end{bmatrix}, \bar{H} = \begin{bmatrix} -I \\ 0 \end{bmatrix}, \bar{C} = \begin{bmatrix} 0 & C \end{bmatrix}. \tag{2.29}$$

It is not difficult to prove that the controllability of the augmented system is guaranteed when (A,B) is stabilizable and the matrix of

$$\begin{bmatrix} C & 0 \\ A & B \end{bmatrix}$$

has full row rank.

As the states are not available, an observer-based tracking controller is designed for fault-free condition. Let

$$\hat{\xi}(t) = \int_0^t (\hat{\omega}(\tau) - \omega_g(\tau))d\tau, \tag{2.30}$$

$$\hat{\bar{x}}(t) = [\hat{\xi}^\top(t) \;\; \hat{x}^\top(t)]^\top, \tag{2.31}$$

$$e_{\bar{x}} = \hat{\bar{x}} - \bar{x}. \tag{2.32}$$

Here $\hat{x}(t)$ and $\hat{\omega}(t)$ are obtained from the adaptive observer in (2.9). The fault-free controller is

$$u_N(t) = K\hat{\bar{x}}(t), \tag{2.33}$$

where $K \in \mathbb{R}^{p\times(m+n)}$ is the controller gain to be determined.

For the fault condition of loss of actuator effectiveness, the controller is given by

$$u_F(t) = \hat{E}(t)u_N(t) = \hat{E}(t)K\hat{\bar{x}}(t), \tag{2.34}$$

where $\hat{E}\hat{F} = \hat{F}\hat{E} = I$. Here $\hat{E}$ is easy to obtain as $\hat{F}$ is diagonal and each element $\hat{f}_i \geq \underline{f}_i > 0$. Then, substituting (2.34) into (2.28), the closed-loop augmented model of is given by

$$\begin{aligned}
\dot{\bar{x}}(t) =& \bar{A}\bar{x}(t) + \bar{B}F(t)u_F(t) + \bar{G}g(x(t)) + \bar{H}\omega_g(t) \\
=& \bar{A}\bar{x}(t) + \bar{B}\hat{F}(t)\hat{E}(t)u_N(t) - \bar{B}\hat{F}(t)\hat{E}(t)u_N(t) + \bar{B}F(t)u_F(t) + \bar{G}g(x(t)) + \bar{H}\omega_g(t) \\
=& \bar{A}\bar{x}(t) + \bar{B}K\hat{\bar{x}}(t) - \bar{B}e_F(t)u_F(t) + \bar{G}g(x(t)) + \bar{H}\omega_g(t) \\
=& \bar{A}\bar{x}(t) + \bar{B}K\bar{x}(t) + \bar{B}Ke_{\bar{x}} - \bar{B}e_F(t)u_F(t) + \bar{G}g(x(t)) + \bar{H}\omega_g(t) \\
=& (\bar{A} + \bar{B}K)\bar{x}(t) + \bar{B}Ke_{\bar{x}} - \bar{B}e_F(t)u_F(t) + \bar{G}g(x(t)) + \bar{H}\omega_g(t).
\end{aligned} \tag{2.35}$$

A stability condition with the guaranteed cost performance (2.8) of the closed-loop fault system (2.35) is presented as follows.

Theorem 2.4.1 *Given a constant $\gamma > 0$, the matrices $\bar{Z} = diag\{Z_1,\ Z_2\} > 0$ and $Z_3 > 0$, if there exist a constant $\kappa_1 > 0$, a symmetric positive definite matrices $P_5 \in \mathbb{R}^{(m+n)\times(m+n)}$, such that the following inequality holds*

$$\Omega_3 = \begin{bmatrix} \Delta_2 & P_5\bar{H} \\ * & -\gamma I \end{bmatrix} < 0, \tag{2.36}$$

where $\Delta_2 = P_5(\bar{A}+\bar{B}K) + (\bar{A}+\bar{B}K)^\top P_5 + 2l_f P_5\tilde{G} + Z + K^\top Z_3 K + \kappa_1 I$, $\tilde{G} = [0 \quad \bar{G}]$ and $\tilde{G} \in \mathbb{R}^{(m+n)\times(m+n)}$, then the closed-loop system in (2.35) is stable, and output weight vector $\omega(t)$ converges to the desired weight $\omega_g(t)$. Furthermore, the performance index (2.8) has an upper bound:

$$\begin{aligned} J_t \leq & e_x^\top(0)P_1 e_x(0) + trace[e_F(0)P_3^{-1}e_F(0)] \\ & + \bar{x}^\top(0)P_5\bar{x}(0) + \gamma\int_0^\infty \omega_g^\top(t)\omega_g(t)dt. \end{aligned} \tag{2.37}$$

Proof. In the proof, firstly we show that the states of system (2.35) are bounded for all t; then we show that the system (2.35) is stable and $\omega(t)$ converges to the desired weight $\omega_g(t)$. At last we show that (2.37) is true.

Choose a Lyapunov function as

$$V(t) = V_{\bar{x}}(t) + \varepsilon V_e(t), \tag{2.38}$$

where $V_{\bar{x}}(t) = \bar{x}^\top(t)P_5\bar{x}(t)$, and $V_e(t)$ is defined in (2.16). ε is a positive scalar. By differentiating $V_x(t)$ along the trajectory of the system (2.35) it gives

$$\dot{V}_{\bar{x}}(t) = 2\bar{x}^\top(t)P_5[(\bar{A}+\bar{B}K)\bar{x}(t) + \bar{B}Ke_{\bar{x}} - \bar{B}e_F(t)u_F(t) + \bar{G}g(x(t)) + \bar{H}\omega_g(t)]. \tag{2.39}$$

Add $-\gamma\omega_g^\top(t)\omega_g(t)$ to (2.39), and according to *Assumption* 2.2.1,

$$\begin{aligned} & \dot{V}_{\bar{x}}(t) - \gamma\omega_g^\top(t)\omega_g(t) \\ =& 2\bar{x}^\top(t)P_5[(\bar{A}+\bar{B}K)\bar{x}(t) + \bar{G}g(x(t)) + \bar{H}\omega_g(t)] - \gamma\omega_g^\top(t)\omega_g(t) \\ & + 2\bar{x}^\top(t)P_5\bar{B}Ke_{\bar{x}}(t) - 2\bar{x}^\top(t)P_5\bar{B}e_F(t)u_F(t) \\ \leq & 2\bar{x}^\top(t)P_5(\bar{A}+\bar{B}K)\bar{x}(t) + 2l_f P_5\tilde{G} \parallel \bar{x}(t) \parallel^2 + 2\bar{x}^\top(t)P_5\bar{H}\omega_g(t) - \gamma\omega_g^\top(t)\omega_g(t) \\ & + 2\bar{x}^\top(t)P_5\bar{B}Ke_{\bar{x}}(t) - 2\bar{x}^\top(t)P_5\bar{B}e_F(t)u_F(t) \\ =& \vartheta^\top(t)\Omega_4\vartheta(t) + 2\bar{x}^\top(t)P_5\bar{B}Ke_{\bar{x}}(t) - 2\bar{x}^\top(t)P_5\bar{B}e_F(t)u_F(t), \end{aligned} \tag{2.40}$$

where $\vartheta(t) = [\bar{x}^\top(t) \;\; \omega_g^\top(t)]^\top$ and

$$\Omega_4 = \begin{bmatrix} \Delta_3 & P_5\bar{H} \\ * & -\gamma I \end{bmatrix},$$

where $\Delta_3 = P_5(\bar{A}+\bar{B}K) + (\bar{A}+\bar{B}K)^\top P_5 + 2l_f P_5\tilde{G}$. For any $\vartheta(t) \neq 0$. If (2.36) holds, we have

$$\vartheta^\top(t)\Omega_4\vartheta(t) + \bar{x}^\top(t)(Z + K^\top Z_3 K + \kappa_1 I)\bar{x}(t) = \vartheta^\top(t)\Omega_3\vartheta(t) < 0. \tag{2.41}$$

Therefore,

$$\begin{aligned} &\dot{V}_x(t) - \gamma\omega_g^\top(t)\omega_g(t) \\ <& -\bar{x}^\top Z\bar{x}(t) - \bar{x}^\top K^\top Z_3 K\bar{x}(t) - \kappa_1||\bar{x}(t)||^2 + 2\bar{x}^\top(t)P_5\bar{B}Ke_{\bar{x}}(t) \\ &- 2\bar{x}^\top(t)P_5\bar{B}e_F(t)u_F(t) \\ <& -\kappa_1||\bar{x}(t)||^2 + 2\bar{x}^\top(t)P_5\bar{B}Ke_{\bar{x}} - 2\bar{x}^\top(t)P_5\bar{B}e_F(t)u_F(t). \end{aligned} \tag{2.42}$$

Hence, according to (2.27) and (2.42), it can be obtained that

$$\begin{aligned} &\dot{V}(t) - \gamma\omega_g^\top(t)\omega_g(t) \\ =&\dot{V}_x(t) + \varepsilon\dot{V}_e(t) - \gamma\omega_g^\top(t)\omega_g(t) \\ <& -\kappa_1||\bar{x}(t)||^2 + 2\bar{x}\Delta_4\zeta(t) - \varepsilon[\lambda_{min}(-\Omega_2)||\bar{e}(t)||^2 \\ &- \mu f_m^2\bar{u}^2\lambda_{max}((P_3^{-1})^\top P_2^{-1}P_3^{-1})]. \end{aligned} \tag{2.43}$$

where

$$\Delta_4 = [P_5\bar{B}K \;\; -P_5\bar{B}],$$

and

$$\zeta(t) = [e_{\bar{x}}^\top(t) \;\; u_F^\top(t)e_F(t)]^\top.$$

For

$$\lambda_{min}(-\Omega_2)||\bar{e}(t)||^2 > \mu f_m^2\bar{u}^2\lambda_{max}((P_3^{-1})^\top P_2^{-1}P_3^{-1}), \tag{2.44}$$

there exists κ_2 so that

$$\lambda_{min}(-\Omega_2)||\bar{e}(t)||^2 - \mu f_m^2\bar{u}^2\lambda_{max}((P_3^{-1})^\top P_2^{-1}P_3^{-1}) = \kappa_2||\bar{e}(t)||^2, \tag{2.45}$$

and let $\bar{\kappa}_3 = \| \; [P_5\bar{B}K \;\; -P_5\bar{B}] \; \|$, then (2.43) becomes,

$$\dot{V}(t) - \gamma\omega_g^\top(t)\omega_g(t) < -\kappa_1||\bar{x}(t)||^2 - \varepsilon\kappa_2||\bar{e}(t)||^2 + 2\bar{\kappa}_3 \; \| \; \bar{x} \; \| \| \; \zeta(t) \; \| \; . \tag{2.46}$$

According to (2.26), $\bar{e}(t) = \left[\begin{array}{ccc} e_x^\top(t) & g_e^\top(t) & u_F^\top(t) e_F(t) \end{array} \right]^\top$, moreover, according to (2.30), (2.31) and (2.32), there exists κ so that,

$$\bar{\kappa}_3 \parallel \zeta(t) \parallel \leq \kappa_3 \parallel \bar{e}(t) \parallel, \tag{2.47}$$

then

$$\begin{aligned}
&\dot{V}(t) - \gamma \omega_g^\top(t) \omega_g(t) \\
<& -\kappa_1 ||\bar{x}(t)||^2 - \varepsilon \kappa_2 ||\bar{e}(t)||^2 + 2\kappa_3 \parallel \bar{x} \parallel \parallel \bar{e}(t) \parallel \\
=& -\varepsilon \kappa_2 [||\bar{e}(t)||^2 - \frac{2\kappa_3}{\varepsilon \kappa_2} \parallel \bar{x} \parallel \parallel \bar{e}(t) \parallel + \frac{\kappa_3^2}{\varepsilon^2 \kappa_2^2} ||\bar{x}(t)||^2] + \frac{\kappa_3^2}{\varepsilon \kappa_2} ||\bar{x}(t)||^2 - \kappa_1 ||\bar{x}(t)||^2 \\
<& -\frac{1}{\varepsilon \kappa_2} (\varepsilon \kappa_1 \kappa_2 - \kappa_3^2) ||\bar{x}(t)||^2.
\end{aligned} \tag{2.48}$$

It is easy to find a ε so that $\varepsilon \kappa_1 \kappa_2 > \kappa_3^2$. Then,

$$\dot{V}(t) - \gamma \omega_g^\top(t) \omega_g(t) < 0. \tag{2.49}$$

Let $\kappa = \frac{1}{\varepsilon \kappa_2} (\varepsilon \kappa_1 \kappa_2 - \kappa_3^2)$, and we have,

$$\dot{V}(t) < -\kappa ||\bar{x}(t)||^2 + \gamma ||\omega_g(t)||^2. \tag{2.50}$$

Thus, $\dot{V}(t) < 0$ if $||\bar{x}(t)|| > \sqrt{\frac{\gamma}{\kappa}} ||\omega_g(t)||$ holds, which means that for all t, the state vector $||\bar{x}(t)||$ will converge until it arrive at $\min\{||\bar{x}(0)||, \sqrt{\frac{\gamma}{\kappa}} ||\omega_g(t)||\}$. That means $\lim_{t\to\infty} \bar{x} = \bar{x}_e$ and $\lim_{t\to\infty} \xi = \xi_e$, where $\bar{x}_e$ and ξ_e are the equilibrium value of $\bar{x}$ and ξ, respectively. Hence, $\lim_{t\to\infty} \dot{\xi} = 0$. Consequently, $\lim_{t\to\infty} (\omega(t) - \omega_g(t)) = 0$ holds, which means $\omega(t)$ converge to the desired weight $\omega_g(t)$.

Finally, it is left to verify that the tracking performance should be guaranteed. According to (2.40), (2.41), (2.42), (2.43) and (2.45),

$$\begin{aligned}
&\dot{V}(t) + \bar{x}^\top(t) Z \bar{x}(t) + \bar{u}^\top(t) Z_3 \bar{u}(t) - \gamma \omega_g^\top(t) \omega_g(t) \\
=& \dot{V}_{\bar{x}}(t) + \varepsilon \dot{V}_e(t) - \gamma \omega_g^\top(t) \omega_g(t) + \bar{x}^\top(t) Z \bar{x}(t) + \bar{u}^\top(t) Z_3 \bar{u}(t) \\
=& \dot{V}_x(t) - \gamma \omega_g^\top(t) \omega_g(t) + \bar{x}^\top(t) (Z + K^\top Z_3 K + \kappa_1 I) \bar{x}(t) - \kappa_1 ||\bar{x}(t)||^2 - \varepsilon \kappa_2 ||\bar{e}(t)||^2 \\
\leq& \vartheta^\top(t) \Omega_3 \vartheta(t) - \kappa_1 ||\bar{x}(t)||^2 - \varepsilon \kappa_2 ||\bar{e}(t)||^2 + 2\kappa_3 \parallel \bar{x} \parallel \parallel \bar{e}(t) \parallel \\
<& \vartheta^\top(t) \Omega_3 \vartheta(t) - \kappa ||\bar{x}(t)||^2.
\end{aligned} \tag{2.51}$$

If (2.36) holds, we have (2.51) is less than 0.

Integrating left side of (2.51) from $t = 0$ to $t = \infty$, we obtain

$$\begin{aligned} J_t &= \int_0^\infty [\xi^\top(t) Z_1 \xi(t) + x^\top(t) Z_2 x(t) + \bar{u}^\top(t) Z_3 \bar{u}(t)] dt \\ &< -\int_0^\infty \dot{V}(t) dt + \gamma \int_0^\infty \omega_g^\top(t) \omega_g(t) dt \\ &< \varepsilon e_x^\top(0) P_1 e_x(0) + \varepsilon trace[e_F(0) P_3^{-1} e_F(0)] + \bar{x}^\top(0) P_5 \bar{x}(0) + \gamma \int_0^\infty \omega_g^\top(t) \omega_g(t) dt. \end{aligned} \tag{2.52}$$

This completes the proof. ■

Although *Theorem* 2.4.1 provides a sufficient condition for closed-loop stability and PDF weight tracking, it provides a sufficient condition for the desirable stability and the output distribution shape tracking performance, but this condition cannot be used directly for obtaining the controller gain K. In order to obtain a feasible LMI condition for the controller gain, an appropriate transformation is taken together with an optimization method to obtain an optimal tracking controller design as follows.

Theorem 2.4.2 *For the system (2.35) associated with the cost function (2.37), given a constant $\gamma > 0$, the matrices $Z = diag\{Z_1,\ Z_2\} > 0,\ Z_3 > 0$, if there exist solutions in the following optimization problem*

$$\min_{\kappa_1, Z, Z_3, Q_1, W_1} trace(T_1) \tag{2.53}$$

subject to the following LMIs

$$\Omega_5 = \begin{bmatrix} \Delta_4 & \bar{H} & Q_1 & W_1^\top & Q_1 \\ * & -\gamma I & 0 & 0 & 0 \\ * & * & -Z^{-1} & 0 & 0 \\ * & * & * & -Z_3^{-1} & 0 \\ * & * & * & * & -\kappa_1 I \end{bmatrix} < 0, \tag{2.54}$$

$$\Omega_6 = \begin{bmatrix} T_1 & I \\ I & Q_1 \end{bmatrix} > 0, \tag{2.55}$$

with the constant $\kappa_1 > 0$, the matrix $Q_1 > 0$ and any matrix W_1, then $K = W_1 Q_1^{-1}$ is an optimal fault-tolerant shape controller gain, which ensures the minimization of the guaranteed cost (2.37) for the system (2.35), where

$$\Delta_4 = \bar{A} Q_1 + Q_1 \bar{A}^\top + \bar{B} W_1 + W_1^\top \bar{B}^\top.$$

Proof. Suppose the inequality (2.36) holds and let

$$\Xi_1 = \begin{bmatrix} P_5^{-1} & 0 \\ 0 & I \end{bmatrix}. \tag{2.56}$$

Then, pre-multiplying (2.36) by $\Xi_1^\top$ and post-multiplying by Ξ_1, the following inequality holds

$$\begin{bmatrix} \Delta_5 & \bar{H} \\ * & -\gamma I \end{bmatrix} < 0, \tag{2.57}$$

where $\Delta_5 = \bar{A}Q_1 + Q_1\bar{A}^\top + \bar{B}W_1 + W_1^\top \bar{B}^\top + 2l_f\tilde{G}Q_1 + Q_1(Z + K^\top Z_3 K + \kappa I)Q_1$, and $Q_1 = P_5^{-1}$. Applying the Schur complement to (2.57), the inequality (2.54) holds and the performance index (2.37) can be rewritten as

$$\begin{aligned} J_t \leq & e_x^\top(0)P_1 e_x(0) + trace[e_F(0)P_3^{-1}e_F(0)] \\ & + \bar{x}^\top(0)Q_1^{-1}\bar{x}(0) + \gamma\int_0^\infty \omega_g^\top(t)\omega_g(t)dt. \end{aligned} \tag{2.58}$$

Moreover, the minimization of $Trace(T_1)$ implies the minimization of the guaranteed cost in (2.58). The stability of the closed-loop system by such K can be easily induced from *Theorem* 2.4.2 so the proof will not be repeated herein. This completes the proof. ■

2.5 Overall Adaptive Fault Estimation and Fault-Tolerant Control Scheme

In Fig. 2.1, the block diagram of the proposed fault-tolerant shape control scheme for stochastic distribution system against LOCE failures is given.

The detailed implementation of the scheme is sketched here:

1. According to the target PDF shape, Chose the appropriate n B-spline basis functions $\Gamma_i(i = 1, 2, \cdots, n)$;

2. Calculate the target pseudo weights vector ω_g according to Eq. (2.7);

3. Measure the system output PDF, calculate the pseudo weights vector $\omega(t)$ according to Eq. (2.2);

4. Adaptively estimate the states and LOCE faults according to Theorem 2.3.1;

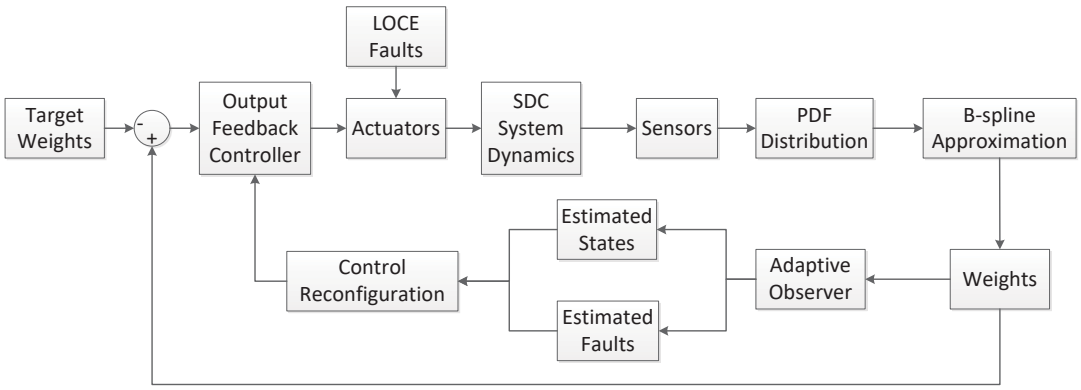

Figure 2.1: Overall adaptive fault estimation and fault-tolerant control scheme

5. Calculate the optimal fault-tolerant shape controller gain K according to Theorem 2.4.2;

6. Design the FTSC law according to Eq. (2.34) based on the estimated states, faults and the calculated K in step 4.

2.6 Simulation and Practical Application

2.6.1 A Numerical Example

To demonstrate and validate the proposed adaptive FTSC scheme, an example is given and simulation results are obtained. Consider a stochastic system whose desired output PDF is shown in Fig. 2.2.

It is formulated according to Eq. (2.2) with the B-spline functions $\Gamma_i(\eta),(i=1,2,3,4,5)$ as follows:

$$\begin{aligned}\Gamma_i(\eta) =& 0.5(\frac{\eta}{100}-i+1)^2 I_i + \Big[-(\frac{\eta}{100})^2+(2i+1)\frac{\eta}{100} \\ & -2\sum_{j=1}^{i} j+0.5\Big] I_{i+1} + 0.5(i+2-\frac{\eta}{100})^2 I_{i+2},\end{aligned}$$

where $I_i,\ (i=1,2,3,4,5)$ is the interval function defined as:

$$I_i = \begin{cases} 1,\ \eta \in [100(i-1),\ 100i) \\ 0,\ otherwise \end{cases}.$$

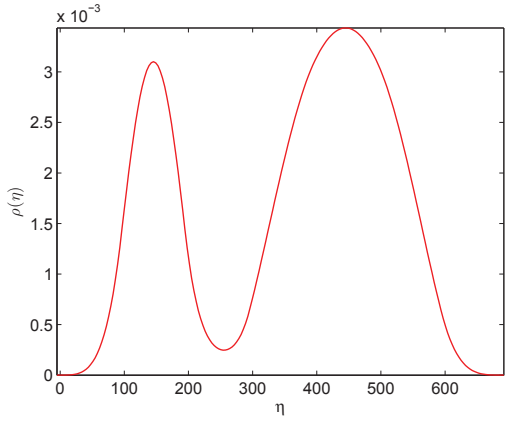

Figure 2.2: Target PDF distribution

The corresponding pseudo weights for the target PDF distribution $\rho_g(\eta)$ in Figure 2.2 is $\omega_g = [6,\ 0.1,\ 4,\ 5,\ 4]^\top$. The system coefficients matrices corresponding to Eq.(2.3) are assumed to be:

$$A = \begin{bmatrix} 0 & 5 & 0 & 0 & 0 \\ -2.5 & 0 & 19.5 & 0 & 12 \\ 0 & 0 & 0 & 1 & 0 \\ 48.6 & 0 & -48.6 & -1.25 & 5.5 \\ 0 & 0 & 0 & 0 & 1 \end{bmatrix}, B = \begin{bmatrix} 1.4 & 0 & 0 & 0 & 0 \\ 0 & 21.6 & 0 & 0 & 0 \\ 0 & 0 & 3.5 & 0 & 0 \\ 0 & 0 & 0 & 7.8 & 0 \\ 0 & 0 & 0 & 0 & 15.6 \end{bmatrix},$$

$C = I_{5\times5}$, $G = I_{5\times5}$ and $g(x) = \frac{1}{1+e^{-x}} - 0.5$. The initial condition in the dynamic weight system is given by (2.3) with the above matrices and $x(0) = [1,\ 1,\ 1,\ 1,\ 1]^\top$. The sampling time is $0.001s$. Different type of LOCE faults $F(t) = diag[0.2,\ 0.7+0.2cos(0.3t),\ 1,\ 0.4,\ 0.3]$ have been added to demonstrate the effectiveness of the proposed methods. According to the fault types, we can find that u_1, u_4, u_5 have constant control effectiveness losses of $0.2, 0.4$ and 0.3, respectively. u_3 is normal with no control effective loss and u_2 faces a oscillatory type of fault.

Fig. 2.3(a) and Fig. 2.3(b) illustrates the system states and faults estimation performances, respectively. Accurate estimations have been reached in both of them. Especially in Fig. 2.3(b), the no fault, constant faults and time-varying fault can be estimated simultaneously and the estimation results are accurate. Correspondingly, in Fig.2.4(a), the pseudo weights tracking is achieved at $\omega = [6.002,\ 0.098,\ 3.984,\ 4.998,\ 3.992]^\top$. In Fig. 2.4(b), the satisfactory tracking of target PDF distribution is obtained. Finally, in Fig.2.5, the PDF shape tracking evolution along the time is demonstrated in the 3-D plot.

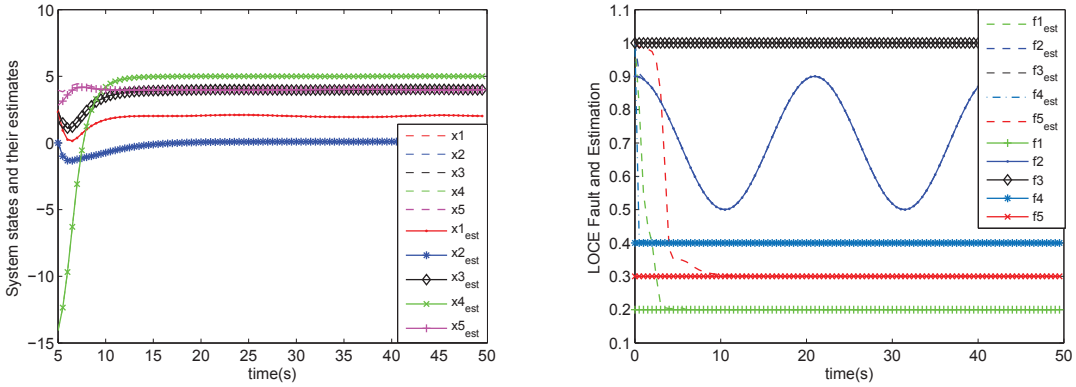

(a) State estimation (b) Fault estimation

Figure 2.3: Estimation of states and faults

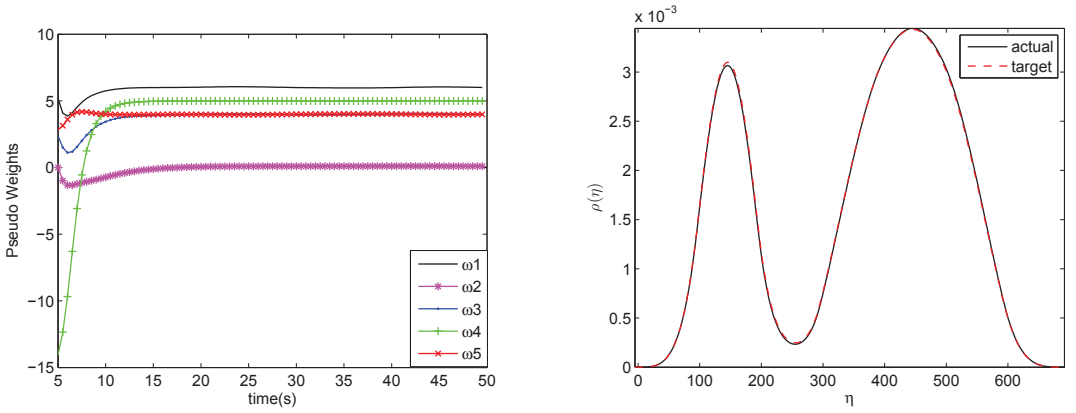

(a) Weights tracking (b) The PDF shape tracking

Figure 2.4: Tracking performance of the weights and the PDF distribution

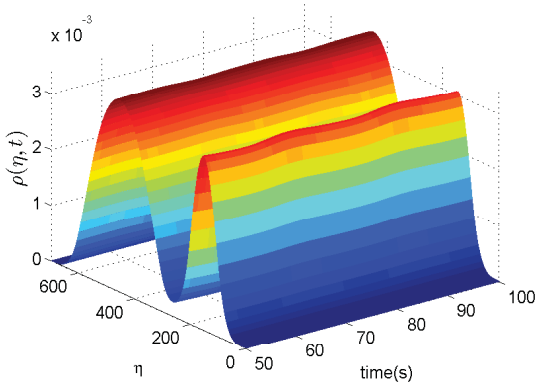

Figure 2.5: 3D dynamic PDF tracking

2.6.2 Application in Soil Particle Distribution Control

In many geotechnical projects, the soil structure and composition plays an extremely important role. They are the indicator of other engineering properties such as compressibility, shear strength, and hydraulic conductivity. The particle distribution of soils is the main fact that affects the permeability and stability of the structure. Foundation with bad soil gradation will lead to leakage loss or even failure of piping. Soil gradation is extremely important for a construction project such as highway, embankment or earthen dam. For this reason, it is vital to control the particle distribution of soils. For example, Fig. 2.6 shows several good gradation curves for crushable soils [99].

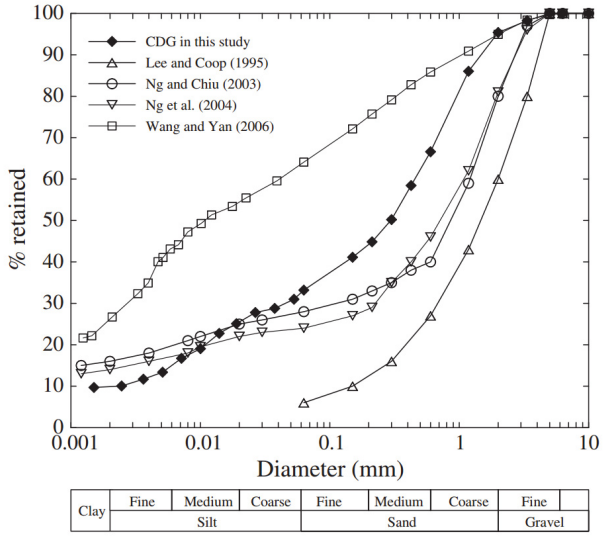

Figure 2.6: Gradation curves of the soil

The particle distribution curve according to the particle size can be obtained by taking the derivative of the gradation curve. By using one of the gradation curves in Fig. 2.6, we obtain the particle size distribution, shown in Fig. 2.7. Here in Fig. 2.7, coordinates on the horizontal axis are bin numbers, which divide the particle distribution into five groups corresponding to the decibel coordinates of Fig. 2.6.

With the development of robotics technology, robots (or robotic arms) have been applied in construction projects to select different soil particles and mix them. For example, excavators are commonly used to collect soils and sands of different size. After that, the collected soils and sands can be mixed to reach a good gradation. However, the measurable output for control is the particle size distribution. In this section, we will apply the techniques introduced in this chapter to the soil gradation control problem.

The detailed mechanical and dynamic models for an excavator are complex. For sim-

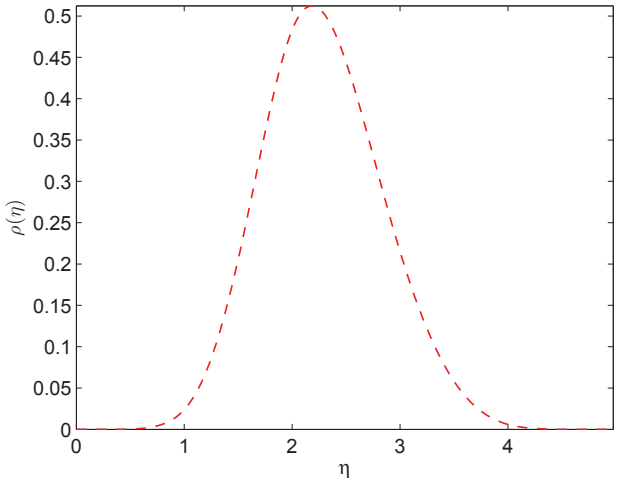

Figure 2.7: Particle distribution curve

plicity, we assume the excavator is controlled through a single link flexible joint system and the position and velocity of both the motor and the link joint are measurable. For the joint system, it can be described by a deterministic physical model. However, for the whole system from the input of motor control to the output of soil particle distribution, it is described by an unknown non-linear stochastic system. It is assumed here that the input affects the distribution of the system output directly. The unknown system relationship between the deterministic output of the excavator and the stochastic output of soil particle distribution is fitted by B-spline approximation. Assume $\eta(t)$ denote the soil size. $\rho(\eta)$ represents the soil size distribution of $\eta(t)$ under the control input $u(t)$.

The single link flexible joint system can be represented in the state space model, [100]:

$$\begin{cases} \dot{\theta}_l = \omega_l \\ \dot{\omega}_l = -\frac{k}{J_l}(\theta_l - \theta_m) - \frac{mgl}{J_l} sin(\theta_l) + \frac{K_D}{J_l} u_1 \\ \dot{\theta_m} = \omega_m \\ \dot{\omega_m} = \frac{k}{J_m}(\theta_l - \theta_m) - \frac{D}{J_m}\omega_m + \frac{K\tau}{J_m} u_2 \end{cases} \tag{2.59}$$

whereθ_l and ω_l represent the link angular position and the link angular velocity respectively, while θ_m and ω_m denote the motor angular position and motor angular velocity respectively. In this system, the control input u_1 is assumed to be directly applied to the link joint to regulate the link angular velocity (e.g. manual control) while the control input u_2 is the motor voltage signal.

For this system, the motor position and velocity can be measured. Moreover, the link angular position and the link angular velocity can also be measured. Parameters of this sin-

Table 2.1: Model Parameters

Parameters (Units)	Value
Motor inertia, $J_m(kg\ m^2)$	3.7×10^{-3}
Link inertia, $J_l(kg\ m^2)$	9.3×10^{-3}
Link mass, $m(kg)$	2.1×10^{-1}
Link length, $l(m)$	3.0×10^{-1}
Torsional spring constant, $k(Nm/rad)$	1.8×10^{-1}
Viscous friction coefficient, $D(Nm/V)$	4.6×10^{-2}
Amplifier gain, $K\tau(Nm/V)$	8×10^{-2}
Orthogonal amplifier gain, $K_D(Nm/V)$	1.3×10^{-2}

gle link model are provided in Table 2.1. Using the state vector as $x = [x_1\ x_2\ x_3\ x_4]^T$, where x_1, x_2, x_3 and x_4 represent $\theta_l, \omega_l, \theta_m$ and ω_m respectively, the deterministic joint model can be presented by Eq. (2.3), while the measured output soil size distribution function of the considered stochastic system can be expressed as a linear combination of all the pre-specified B-spline basis functions. Here it is assumed that, with the proper basis B-spline functions, the dynamics between the weights and the control input are known, which is actually obtainable through a series of experiments. The dynamics can be expressed as (2.7). It is assumed that the target distribution function $T(\eta)$ belongs to the following functional space:

$$T(\eta) \in \Omega_0 = \{\rho | \rho = \frac{\Gamma(\eta)\omega(t)}{\sqrt{\omega^\top(t)\Gamma_f\omega(t)}}, \omega \in R^{n\times 1}, \omega \geq 0\} \tag{2.60}$$

where $\omega(t)$ denotes the weight vector .

On-line measurement of the distribution of soil particles is essential and can be achieved by using proper instrumentation. For example, the more traditional sieving method is generally used while more advanced laser diffraction and light scattering-based methods are applied to grain size analysis. In addition, the soil size distribution function $\rho(\eta, t)$ at each sampling time t can be obtained by one of the standard density estimation methods introduced in [101].

Appropriate B-spline base functions corresponding to Fig. 2.7 are chosen to be:

$$\Gamma_1(\eta) = \begin{cases} \frac{1}{6}\eta^3, & 0 \le \eta < 1 \\ \frac{1}{6}(-3\eta^3 + 12\eta^2 - 12\eta + 4) & 1 \le \eta < 2 \\ \frac{1}{6}(3\eta^3 - 24\eta^2 + 60\eta - 44) & 2 \le \eta < 3 \\ \frac{1}{6}(4-\eta)^3 & 3 \le \eta < 4 \end{cases}, \tag{2.61}$$

$$\Gamma_2(\eta) = \begin{cases} \frac{1}{6}(\eta-1)^3, & 1 \le \eta < 2 \\ \frac{1}{6}(-3\eta^3 + 21\eta^2 - 45\eta + 31) & 2 \le \eta < 3 \\ \frac{1}{6}(3\eta^3 - 33\eta^2 + 117\eta - 131) & 3 \le \eta < 4 \\ \frac{1}{6}(5-\eta)^3 & 4 \le \eta < 5 \end{cases}. \tag{2.62}$$

The system coefficients matrices corresponding to Eq.(2.7) are obtained:

$$A = \begin{bmatrix} 0 & 1 & 0 & 0 \\ -19.5 & 0 & 19.5 & 0 \\ 0 & 0 & 0 & 1 \\ 48.6 & 0 & -48.6 & -1.25 \end{bmatrix}, B = \begin{bmatrix} 0 & 0 \\ 1.4 & 0 \\ 0 & 0 \\ 0 & 21.6 \end{bmatrix},$$

$$G = I, \;\; g(x(t)) = \begin{bmatrix} 0 \\ -3.33 sin(x_1) \\ 0 \\ 0 \end{bmatrix}, C = \begin{bmatrix} 0 & 0 & 1 & 0 \\ 0 & 0 & 0 & 1 \end{bmatrix}.$$

An upper bound on $||\frac{dg(x)}{dx}||$ is found as 3.33, therefore Assumption 2.2.1 can be satisfied and $l_f = 3.33$. The desired distribution is supposed to be described by (2.7) with $\omega_g = [4, \;\; 2]^\top$. The sampling time $T_s = 0.0005s$. Time-varying LOCE fault $F(t)$ has been added to demonstrate the effectiveness of the proposed methods. Here, the oscillatory type of fault signals are used as

$$F(t) = \begin{bmatrix} 0.5 + 0.1cos(0.2t) & 0 \\ 0 & 0.5 + 0.3cos(0.3t) \end{bmatrix}.$$

The LOCE faults and their estimates are shown in Fig.2.8(a). From the simulation results, it can be seen that both the states and the faults can be accurately estimated.

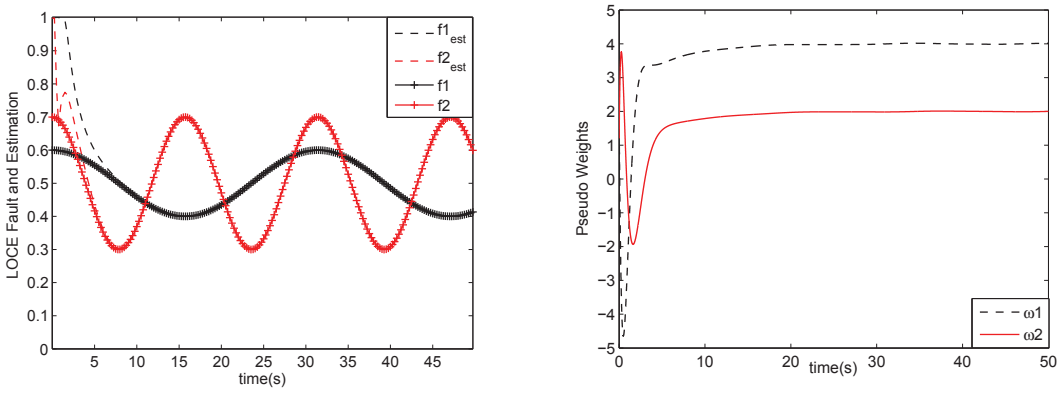

(a) LOCE faults and their estimates

(b) Tracking of weights

Figure 2.8: Fault estimation and weights tracking

Fig.2.8(b) shows the tracking performance of the pseudo weights. From the figure, we can clearly see that ω converge to $\omega_g = [4,\ 2]^\top$ rapidly in only a few iterations. Fig.2.9(a) demonstrates the final soil size distribution shape tracking result with excellent performance. By comparing to the desirable distribution curve of the soil gradation. It can be concluded that the proposed fault-tolerant shape control can accomplish satisfactory performance in this soil particle distribution control application. Finally, in Fig.2.9(b), the 3-D plot of the dynamic distribution tracking is presented, which illustrates the shape tracking evolution along the time.

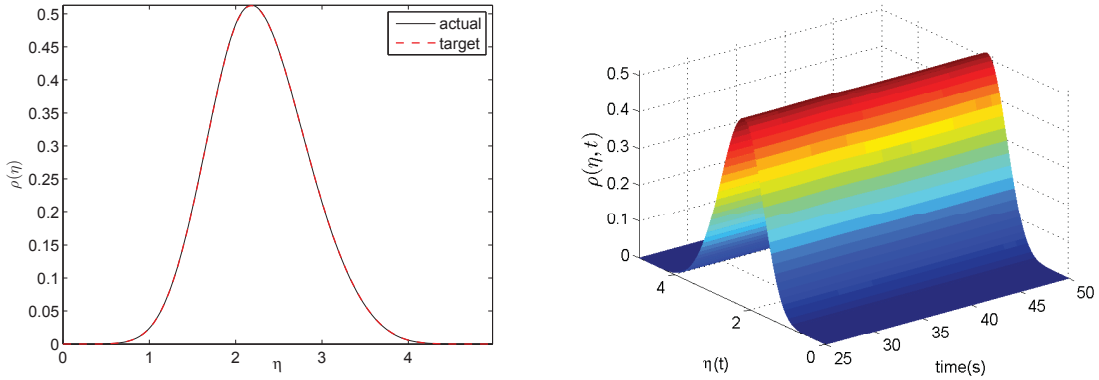

(a) The distribution shape tracking

(b) 3D dynamic distribution response

Figure 2.9: Tracking performance

If no FTSC scheme is applied, the pseudo weights tracking result is shown in Fig.2.10(a), and the corresponding distribution shape tracking result is illustrated in Fig. 2.10(b). From

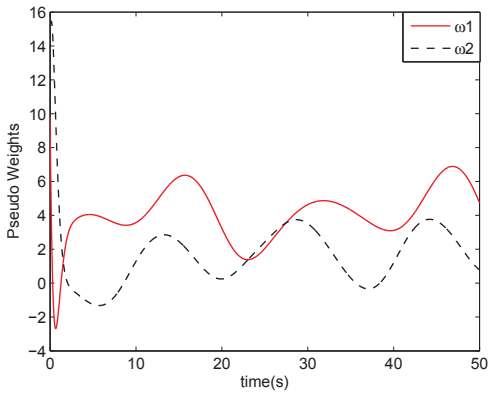

(a) Tracking of weights without FTSC

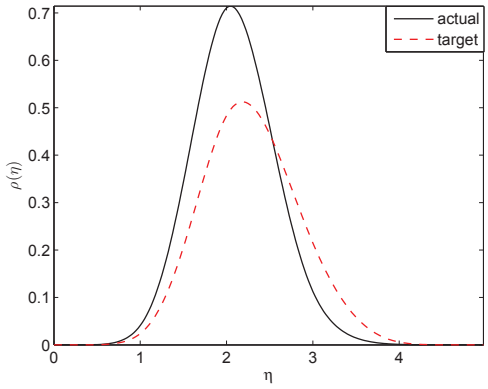

(b) PDF tracking without FTSC

Figure 2.10: Tracking performance without FTSC

both of the figures, we can see that, without the FTSC method, the tracking performance is seriously deteriorated when LOCE faults exist.

2.7 Conclusions

In this chapter, the FTSC problem for nonlinear and non-Gaussian stochastic distribution system is studied. Firstly, an innovative adaptive observer-based fault estimation technique is proposed for time-varying LOCE faults. Both the fault-free and LOCE fault condition can be estimated in the unified framework, simultaneously. Then, an observer-based fault-tolerant stochastic shape controller is developed. In addition, the optimized control performance can be achieved. Simulation results show that the proposed scheme can achieve accurate estimation for time-varying LOCE faults. Furthermore, the stochastic shape tracking performance is highly enhanced through the FTSC technique developed in this work. A successful application example in soil particle distribution control demonstrates the feasibility and effectiveness of the proposed adaptive fault estimation and FTSC method for particle size distribution control.

Chapter 3

Fault-Tolerant Shape Control Under Simultaneous Actuator and Sensor Faults

3.1 Introduction

Particulate processes where the product takes the form of particles, are ubiquitous in agricultural, chemical, mineral and pharmaceutical industries [102]. Examples include the crystallizers for pharmaceutical products [66], the emulsion polymerization reactors for the manufacture of coatings, pigments, latex paints [67], and the biochemical reactors for metabolite production [68]. In these particulate processes, control of particle size distribution (PSD) is the key to achieve the desired physiological and physiochemical properties.

The lumped statistical values, such as moments, are insufficient to characterize the properties of particulate systems. The dynamics of these complex systems can be captured with the full PSD. In the existing research, to obtain a model based PSD controller, mathematical models are designed based on the population balance equation (PBE), coupled with material and energy balance equations, which are nonlinear partial integro-differential equations [102][103]. Analytical solution of the PBE model can only be obtained under very strict assumptions. Therefore, most solution methods are based on numerical analysis. However, the order of the system will be high because of the discretization of spatial variables, resulting in high computation burden. Moreover, the controllability and observability become more difficult to satisfy [104]. The high-order factor may also render the

corresponding linear control problems unsolvable [105].

The presence of faults, if not taken into account in the controller design, may lead to severe deterioration of the closed-loop system performance. The existing research mainly deals with actuator and sensor faults separately and in different formulations, while in many practical applications, actuator and sensor faults can occur in the same system, and even in same time. Misinterpretation of the two different kinds of faults may cause missing-detection, increased maintenance cost, and even system damage. Therefore it is preferable to consider estimation of actuator and sensor faults under a rigorously formulated and unified framework. Sliding mode observers (SMOs) were designed to estimate the actuator and sensor faults simultaneously in [106][107]. However, SMOs need strong assumptions for the ranks of system matrices, which may be difficult to satisfy in some particulate systems.

In this chapter, a shape control scheme is proposed as an alternative to the conventional PSD control. The shape control method can be applied in the particulate process system because the objective of PSD control is to achieve a target particle size distribution shape, which aligns with the original goal of shape control in tracking a desirable PDF shape.

To improve the existing results, in [58] and Chapter 2 of this thesis, for fault-tolerant stochastic shape control, and further apply it in particulate processes, this Chapter aims to provide a fault-tolerant shape control scheme based on adaptive fault estimation for more general fault scenarios. The main contributions of this Chapter are summarized as follows: (i) The shape control strategy is introduced for the application of PSD distribution control for the first time. (ii) An innovative adaptive observer-based fault estimation scheme is proposed to simultaneously estimate the actuator and sensor faults for a nonlinear particulate process. (iii) The proposed fault estimator is designed and operated for fault-free, constant fault and time-varying fault conditions in a unified framework. (iv) Shape control reconfiguration is realized through a virtual actuator and a virtual sensor, which can compensate for both the actuator and sensor faults based on fault estimation.

The remainder of the chapter is organized as follows: Section 3.2 provides preliminary results and problem formulation. The fault estimation and the fault-tolerant shape control design are presented in Section 3.3 as the main results. Finally, in section 3.4, an application simulation example of emulsion polymerization is provided to demonstrate the feasibility of the proposed approach. The conclusion is drawn in Section 3.5.

3.2 Preliminaries and Problem Formulation

3.2.1 Distribution Approximation With B-spline Functions

For a particulate process, the PSD function of particles defines quantitatively how the sizes of the particles are distributed among the particles in the entire population. The PSD function is assumed to be measurable, continuous and bounded. Denote $u(t)$ as the control input and $\rho(\eta,t)$ as the PSD function, where $\eta \in [\alpha,\ \beta]$. It should be noted that in this case, the PSD shape of the output is controllable by the input. In many particulate processes, online measurement of the PSD function is essential and can be achieved by using proper instrumentation [108].

The commonly adopted square-root rational B-spline model is proposed here to approximate PSD function $\rho(\eta,t)$, [64].

$$\sqrt{\rho(\eta,t)} = \frac{\sum_{i=1}^{n} \omega_i(t)\Gamma_i(\eta)}{\sqrt{\sum_{i=1,j=1}^{n} \omega_i(t)\omega_j(t)\int_{\alpha}^{\beta}\Gamma_i(\eta)\Gamma_j(\eta)d\eta}} = \frac{\Gamma(\eta)\omega(t)}{\sqrt{\omega^{\top}(t)\Gamma_f\omega(t)}}, \quad \forall\eta \in [\alpha,\ \beta] \tag{3.1}$$

where $\Gamma(\eta) = [\Gamma_1(\eta),\cdots,\Gamma_n(\eta)]$ and $\Gamma_f = \int_{\alpha}^{\beta}\Gamma^{\top}(\eta)\Gamma(\eta)d\eta$. $\Gamma_i(\eta) \geq 0$, is the prespecified basis function. $\omega(t) = [\omega_1(t),\cdots,\omega_n(t)]^{\top}$, $\omega(t) \neq 0$, represents the corresponding weight coefficients. Here $\omega_i(t)$, $(i = 1,...,n)$ are independently determined and decoupled from each other. They are called pseudo weights as they have no physical meanings and are only used to form the desirable PSDs.

3.2.2 System Model With Simultaneous Time-varying Actuator and Sensor Faults

In this chapter, using the square-root B-spline approximation model for the output PSD, the whole dynamic system can be characterized. The dynamic plant model is given in Eq.(3.2a). The relationship between the pseudo weights and the states without sensor faults is established in Eq.(3.2b). It is worth pointing out that the output matrix C is identified and may have no physical meaning.

$$\dot{x}(t) = Ax(t) + g(x(t)) + Bu(t) + Ff_a(t), \tag{3.2a}$$

$$\omega(t) = Cx(t), \tag{3.2b}$$

where $x(t) \in \mathbb{R}^m$ is the measurable state vector; $\omega(t) \in \mathbb{R}^n$ is the calculated weight vector from the measurable PSD function through Eq. (3.1); $f_a(t) \in \mathbb{R}^p, (n > p)$ is the time-varying actuator fault vector; $u(t) \in \mathbb{R}^l, (l \geq p)$ is the control input; $A \in \mathbb{R}^{m\times m}$, $B \in \mathbb{R}^{m\times l}$,

$F \in \mathbb{R}^{m\times p}$ and $C \in \mathbb{R}^{n\times m}$ are the known matrices. The nonlinear function $g(x(t)) \in \mathbb{R}^m$ is Lipschitz about x uniformly, i.e.: $||g(x(t_1)) - g(x(t_2))||_2 \leq l_f||(x(t_1) - x(t_2))||_2$, $l_f > 0$ and $g(0) = 0$ for any $x(t_1), x(t_2) \in \mathbb{R}^m$ as in [58], where l_f is a Lipschitz constant.

When sensor faults are present, the measured PSD function is given in Eq. (3.3a). The corresponding faulty weights and fault-free weights are calculated through Eq. (3.1). Assume that the relationship between the faulty weights and the fault-free weights can be built as Eq. (3.3b),

$$\rho_f(\eta,t) = \rho(\eta,t) + D_0 f_s(t), \tag{3.3a}$$

$$\omega_f(t) = \omega(t) + D f_s(t), \tag{3.3b}$$

where $\rho_f(\eta,t)$ and $\rho(\eta,t)$ are the measured PSD with and without sensor faults, respectively. $f_s(t) \in \mathbb{R}^q (q \leq n)$ is the sensor fault vector. $D_0 \in \mathbb{R}^{1\times q}$ is the corresponding coefficient matrix. $\omega_f(t) \in \mathbb{R}^n$ and $\omega(t) \in \mathbb{R}^n$ are the corresponding weights calculated from $\rho_f(\eta,t)$ and $\rho(\eta,t)$, respectively. $D \in \mathbb{R}^{n\times q}$ is the coefficient matrix to map the sensor faults into weights formulation.

Remark 3.2.1 *The relationship between $\omega_f(t)$ and $\omega(t)$ in (3.3b) is obtained by linear approximation of the Taylor expansion of Eq. (3.3b) based on the B-spline approximation in Eq. (3.1).*

Combining Eq. (3.2a) and (3.3b), the dynamic system with both actuator and sensor faults can be represented in Σ_1 as:

$$\Sigma_1 : \begin{cases} \dot{x}(t) = Ax(t) + g(x(t)) + Bu(t) + F f_a(t) \\ \omega_f(t) = Cx(t) + D f_s(t) \end{cases} . \tag{3.4}$$

Assumption 3.2.1 $rank(CF) = rank(F) = p$

Assumption 3.2.2 *For every complex number s with nonnegative real part*

$$rank \begin{bmatrix} sI_m - A & F \\ C & 0 \end{bmatrix} = m + p. \tag{3.5}$$

Assumption 3.2.3 *The actuator fault f_a and sensor fault f_s are norm bounded. Also, f_a and f_s are differentiable after their occurrence.*

Remark 3.2.2 *Assumption 1 indicates that the number of independent measurements cannot be smaller than that of independent actuator faults. Assumption 3.2.2 is given as the minimum phase condition [106].*

3.2.3 Control Objectives

With the presence of simultaneous actuator and sensor faults, a fault-tolerant controller composed of a normal controller and a virtual actuator compensator, together with an virtual sensor compensator $v_s(t)$ will be designed to realize the fault-tolerant shape control (FTSC). Adding the sensor compensator, Σ_1 becomes:

$$\Sigma_2 : \begin{cases} \dot{x}(t) = Ax(t) + g(x(t)) + Bu(t) + Ff_a(t) \\ \omega_c(t) = Cx(t) + Df_s(t) + Dv_s(t) \end{cases}, \tag{3.6}$$

where the vector $\omega_c(t) \in \mathbb{R}^n$ is the compensated weights. $v_s(t) \in \mathbb{R}^q$ denotes the virtual sensor compensator and D is the corresponding coefficient matrix which is assumed to be identical to the sensor fault coefficient matrix.

To investigate the fault-tolerant shape controller for Σ_2, the target particle distribution can be approximated as follows:

$$\sqrt{\rho^*(\eta,t)} = \frac{\Gamma(\eta)\omega_g(t)}{\sqrt{\omega_g^\top(t)\Gamma_f\omega_g(t)}},\ \forall \eta \in [\alpha,\ \beta] \tag{3.7}$$

where $\rho^*(\eta,t)$ is the target PSD function and $\omega_g(t)$ is the corresponding target weights based on the given B-spline basis function $\Gamma(\eta)$. Therefore, the shape control objective is simplified to finding the control input $u(t)$ and the sensor compensator $v_s(t)$ such that $\rho(\eta,\ t)$ follows $\rho^*(\eta,t)$. It is known that if $e_\omega(t) = \omega(t) - \omega_g(t) \to 0$, then $\sqrt{\rho(\eta,\ t)} - \sqrt{\rho^*(\eta,t)} \to 0$. The considered fault-tolerant shape controller can be formulated as the tracking of $\omega_g(t)$ even when actuator and sensor faults occur, simultaneously.

The dynamic system Σ_2 is reformulated so that the fault-tolerant controller and the sensor fault compensator can be combined to form an augmented control signal $\bar{u}(t) = [v_s^\top(t)\ \ u^\top(t)]^\top$. Denote $\xi(t) = \int_0^t(\omega_c(\tau) - \omega_g(\tau))d\tau$ and $\bar{x}(t) = [\xi^\top(t)\ \ x^\top(t)]^\top$, $\bar{f}(t) = [f_s^\top(t)\ \ f_a^\top(t)]^\top$. We obtain the following augmented system model Σ_3:

$$\Sigma_3 : \begin{cases} \dot{\bar{x}}(t) = \bar{A}\bar{x}(t) + \bar{g}(x(t)) + \bar{B}\bar{u}(t) + \bar{H}\omega_g(t) + \bar{F}\bar{f}(t) \\ \omega_c(t) = \bar{C}\bar{x}(t) + \bar{D}\bar{f}(t) + Dv_s(t) \end{cases}, \tag{3.8}$$

where $\bar{A} \in \mathbb{R}^{(m+n)\times(m+n)}, \bar{B} \in \mathbb{R}^{(m+n)\times(q+l)}, \bar{H} \in \mathbb{R}^{(m+n)\times n}, \bar{F} \in \mathbb{R}^{(m+n)\times(p+q)}, \bar{C} \in \mathbb{R}^{n\times(m+n)}$, $\bar{D} \in \mathbb{R}^{n\times(p+q)}$. Here $\bar{g}(x(t)) = [0\ \ g^\top(x(t))]^\top$ and $\bar{g}(x(t)) \in \mathbb{R}^{m+n}$. According to the Lipschitz assumption, $\| \bar{g}(x(t)) \| = \| g(x(t)) \| \leq l_f \| x(t) \| \leq l_f \| \bar{x}(t) \|$. It is assumed that $(\bar{A}, \bar{B})$ is stabilizable. These matrices can be described as follows,

$$\bar{A} = \begin{bmatrix} 0 & C \\ 0 & A \end{bmatrix}, \bar{B} = \begin{bmatrix} D & 0 \\ 0 & B \end{bmatrix}, \bar{H} = \begin{bmatrix} -I \\ 0 \end{bmatrix},$$

$$\bar{F} = \begin{bmatrix} D & 0 \\ 0 & F \end{bmatrix}, \bar{C} = \begin{bmatrix} 0 & C \end{bmatrix}, \bar{D} = \begin{bmatrix} D & 0 \end{bmatrix}. \tag{3.9}$$

3.3 Adaptive Observer-Based Fault-Tolerant Shape Control

3.3.1 Optimal Shape Tracking of the Fault-Free System

In this part, a shape tracking controller with optimal control performance is designed for the fault-free model. The following state feedback tracking controller is designed:

$$u_N(t) = K_N \bar{x}(t), \tag{3.10}$$

where $K_N \in \mathbb{R}^{l\times(m+n)}$ is the normal controller gain to be determined and the virtual sensor $v_s(t) = 0$ for the fault-free model. Then, the closed-loop augmented normal model of system (3.8) is given by

$$\dot{\bar{x}}(t) = (\bar{A} + \bar{B}_2 K_N)\bar{x}(t) + \bar{g}(x(t)) + \bar{H}\omega_g(t), \tag{3.11}$$

where $\bar{B}_2$ is the second column block of $\bar{B}$.

Remark 3.3.1 *The augmented state vector $\bar{x}(t)$ is available because the states are assumed to be measurable and $\xi(t)$ can be calculated as $\xi(t) = \int_0^t (\omega_c(\tau) - \omega_g(\tau))d\tau$.*

The optimal controller is designed by minimizing the upper bound of the following cost function:

$$J_t = \int_0^\infty [\xi^\top(t) Z_1 \xi(t) + x^\top(t) Z_2 x(t) + u_N^\top(t) Z_3 u_N(t)]\, dt, \tag{3.12}$$

where $Z_1 > 0$, $Z_2 > 0$ and $Z_3 > 0$ ($Z_1 \in \mathbb{R}^{n\times n}, Z_2 \in \mathbb{R}^{m\times m}$ and $Z_3 \in \mathbb{R}^{l\times l}$).

A stability condition with the guaranteed cost performance (3.12) of the closed-loop fault-free system (3.11) is presented as follows.

Theorem 3.3.1 *Given a constant $\gamma > 0$, the matrices $\bar{Z} = diag\{Z_1,\ Z_2\} > 0$ and $Z_3 > 0$, if there exist a constant $\kappa > 0$, a matrix $P_1 > 0$, such that the following inequality holds*

$$\Omega_1 = \begin{bmatrix} \Delta_1 & P_1\bar{H} \\ * & -\gamma I \end{bmatrix} < 0, \tag{3.13}$$

where $\Delta_1 = P_1(\bar{A}+\bar{B}_2K_N)+(\bar{A}+\bar{B}_2K_N)^\top P_1+2l_fP_1+Z+K_N^\top Z_3K_N+\kappa I$*, then the closed-loop system in (3.11) is stable, and* $\omega(t)$ *converges to the desired weight* $\omega_g(t)$*. Furthermore, the performance index (3.12) has an upper bound:*

$$J_t \leq \bar{x}^\top(0)P_1\bar{x}(0)+\gamma\int_0^\infty \omega_g^\top(t)\omega_g(t)dt. \tag{3.14}$$

Proof. Choose a Lyapunov function as $V_1(t)=\bar{x}^\top(t)P_1\bar{x}(t)$. By differentiating $V_1(t)$ and subtract $\gamma\omega_g^\top(t)\omega_g(t)$ in both sides of the equation, it gives

$$\begin{aligned}
&\dot{V}_1(t)-\gamma\omega_g^\top(t)\omega_g(t)\\
=&2\bar{x}^\top(t)P_1[(\bar{A}+\bar{B}_2K_N)\bar{x}(t)+\bar{g}(x(t))+\bar{H}\omega_g(t)]-\gamma\omega_g^\top(t)\omega_g(t)\\
\leq&2\bar{x}^\top(t)P_1(\bar{A}+\bar{B}_2K_N)\bar{x}(t)+2l_f\bar{x}^\top P_1\bar{x}+2\bar{x}^\top(t)P_1\bar{H}\omega_g(t)-\gamma\omega_g^\top(t)\omega_g(t)\\
=&\vartheta^\top(t)\Omega_2\vartheta(t),
\end{aligned} \tag{3.15}$$

where $\vartheta(t)=[\bar{x}^\top(t)\ \ \omega_g^\top(t)]^\top$ and

$$\Omega_2=\begin{bmatrix}\Delta_2 & P_1\bar{H}\\ * & -\gamma I\end{bmatrix},$$

where $\Delta_2=P_1(\bar{A}+\bar{B}_2K_N)+(\bar{A}+\bar{B}_2K_N)^\top P_1+2l_fP_1$. For any $\vartheta(t)\neq 0$, if (3.13) holds, we have

$$\vartheta^\top(t)\Omega_2\vartheta(t)+\bar{x}^\top(t)(Z+K_N^\top Z_3K_N+\kappa I)\bar{x}(t)\leq\vartheta^\top(t)\Omega_1\vartheta(t)<0. \tag{3.16}$$

Therefore,

$$\dot{V}_1(t)-\gamma\omega_g^\top(t)\omega_g(t)<-\bar{x}^\top Z\bar{x}(t)-\bar{x}^\top K_N^\top Z_3K_N\bar{x}(t)-\kappa||\bar{x}(t)||^2. \tag{3.17}$$

As $Z>0$ and $Z_3>0$, we can have $\bar{x}^\top Z\bar{x}(t)>0$ and $\bar{x}^\top K_N^\top Z_3K_N\bar{x}(t)>0$. Therefore, (3.17) can be relaxed to be the following:

$$\dot{V}_1(t)-\gamma\omega_g^\top(t)\omega_g(t)<-\kappa||\bar{x}(t)||^2. \tag{3.18}$$

Then, it can be obtained that

$$\dot{V}_1(t)<-\kappa||\bar{x}(t)||^2+\gamma||\omega_g(t)||^2. \tag{3.19}$$

Thus, $\dot{V}_1<0$ if $||\bar{x}(t)||>\sqrt{\frac{\gamma}{\kappa}}||\omega_g(t)||$ holds, which means that for all t, the state vector $||\bar{x}(t)||$ satisfies $||\bar{x}(t)||\leq\max\{||\bar{x}(0)||,\ \sqrt{\frac{\gamma}{\kappa}}||\omega_g(t)||\}$.

Then, we show that there is a unique equilibrium point of (3.11) for the given $\omega_g(t)$. Corresponding to a fixed initial condition and the input $\omega_g(t)$, assume that $\bar{x}_1(t)$ and $\bar{x}_2(t)$ are two trajectories of the system (3.11). Then, the dynamics of $\varepsilon(t) = \bar{x}_1(t) - \bar{x}_2(t)$ can be described as

$$\begin{aligned} \dot{\varepsilon}(t) &= (\bar{A} + \bar{B}_2 K_N)\varepsilon(t) + [\bar{g}(x_1(t)) - \bar{g}(x_2(t))] \\ &\leq (\bar{A} + \bar{B}_2 K_N)\varepsilon(t) + l_f ||\varepsilon(t)|| \end{aligned} \tag{3.20}$$

with initial condition $\varepsilon(t) = 0$. By using the Lyapunov function $V_2(t) = \varepsilon^\top(t) P_1 \varepsilon(t)$, we have

$$\begin{aligned} \dot{V}_2(t) &\leq 2\varepsilon^\top(t) P_1 [(\bar{A} + \bar{B}_2 K_N)\varepsilon(t) + l_f ||\varepsilon(t)||] \\ &= \vartheta_1^\top(t) \Omega_2 \vartheta_1(t), \end{aligned} \tag{3.21}$$

where $\vartheta_1(t) = [\varepsilon^\top(t) \;\; 0]^\top$. Then it can be seen that $\dot{V}_2(t) < -\kappa ||\varepsilon(t)||^2$. Thus, it can be verified that $\varepsilon = 0$ is the unique asymptotically stable equilibrium point of the system (3.20). It means that the closed-loop system (3.11) also has a unique stable equilibrium trajectory. Hence, $\lim_{t\to\infty} \xi(t) = \xi_e$ and $\lim_{t\to\infty} \dot{\xi}(t) = 0$, where ξ_e is the equilibrium value of ξ. Consequently, $\lim_{t\to\infty}(\omega(\tau) - \omega_g(\tau)) = 0$ holds, which means $\omega(t)$ can converge to the desired weight $\omega_g(t)$.

Finally, it is left to show that the tracking performance is guaranteed. According to Eq. (3.15) and Eq. (3.16), the following Eq. (3.22) can be obtained:

$$\dot{V}_1(t) - \gamma \omega_g^\top(t)\omega_g(t) + \bar{x}^\top(t) Z \bar{x}(t) + u_N^\top(t) Z_3 u_N(t) + \kappa \bar{x}^\top(t)\bar{x}(t) \leq \vartheta^\top(t) \Omega_1 \vartheta(t). \tag{3.22}$$

If (3.13) holds, then the right-hand-side of Eq. (3.22) is less than 0. Furthermore, we have $\kappa \bar{x}^\top(t)\bar{x}(t) \geq 0$, as $\kappa > 0$. Therefore, the following Eq. (3.23) can be obtained by relaxing the condition of Eq. (3.22):

$$\dot{V}_1(t) - \gamma \omega_g^\top(t)\omega_g(t) + \bar{x}^\top(t) Z \bar{x}(t) + u_N^\top(t) Z_3 u_N(t) \leq 0. \tag{3.23}$$

Integrating both sides of (3.23) from $t = 0$ to $t = \infty$, we obtain

$$\begin{aligned} J_t &= \int_0^\infty [\xi^\top(t) Z_1 \xi(t) + x^\top(t) Z_2 x(t) + u_N^\top(t) Z_3 u_N(t)] dt \\ &\leq -\int_0^\infty \dot{V}_1(t) dt + \gamma \int_0^\infty \omega_g^\top(t)\omega_g(t) dt \\ &\leq \bar{x}^\top(0) P_1 \bar{x}(0) + \gamma \int_0^\infty \omega_g^\top(t)\omega_g(t) dt. \end{aligned} \tag{3.24}$$

This completes the proof. ■

Theorem 3.3.1 only provides a sufficient condition but cannot be used directly for obtaining the controller gain K_N. A feasible LMI realization is designed in Theorem 3.3.2 as follows.

Theorem 3.3.2 *For the system (3.11) associated with the cost function (3.14), given a constant $\gamma > 0$, the matrices $Z = diag\{Z_1,\ Z_2\} > 0,\ Z_3 > 0$, if there exist solutions in the following optimization problem*

$$\min_{\kappa, Z, Z_3, Q_1, W_1} trace(S) \tag{3.25}$$

subject to the following LMIs

$$\Omega_3 = \begin{bmatrix} \Delta_3 & \bar{H} & Q_1 & W_1^\top & Q_1 \\ * & -\gamma I & 0 & 0 & 0 \\ * & * & -Z^{-1} & 0 & 0 \\ * & * & * & -Z_3^{-1} & 0 \\ * & * & * & * & -\kappa I \end{bmatrix} < 0, \tag{3.26}$$

$$\Delta_3 = \bar{A}Q_1 + Q_1\bar{A}^\top + \bar{B}_2 W_1 + W_1^\top \bar{B}_2^\top + 2l_f Q_1,$$

$$\Omega_4 = \begin{bmatrix} S & I \\ I & Q_1 \end{bmatrix} > 0, \tag{3.27}$$

with the constant $\kappa > 0$, the matrix $Q_1 > 0$ ($Q_1 \in \mathbb{R}^{(m+n)\times(m+n)}$) and any matrix $W_1 \in \mathbb{R}^{l\times(m+n)}$. Then $K_N = W_1 Q_1^{-1}$ is an optimal stabilizing shape controller gain, which ensures the minimization of the guaranteed cost (3.14) for the system (3.11).

Proof. Suppose the inequality (3.13) holds and let

$$\Xi_1 = \begin{bmatrix} P_1^{-1} & 0 \\ 0 & I \end{bmatrix}. \tag{3.28}$$

Then, pre-multiplying (3.13) by $\Xi_1^\top$ and post-multiplying by Ξ_1, the following inequality holds

$$\begin{bmatrix} \Delta_3 & \bar{H} \\ * & -\gamma I \end{bmatrix} < 0, \tag{3.29}$$

where $\Delta_3 = \bar{A}Q_1 + Q_1\bar{A}^\top + \bar{B}_2W_1 + W_1^\top\bar{B}_2^\top + 2l_fQ_1 + Q_1(Z + K_N^\top Z_3K_N + \kappa I)Q_1$, and $Q_1 = P_1^{-1}$. Applying the Schur complement to (3.29), the inequality (3.26) holds and the performance index (3.14) can be rewritten as

$$J_t \leq \bar{x}^\top(0)Q_1^{-1}\bar{x}(0) + \gamma\int_0^\infty \omega_g^\top(t)\omega_g(t)dt. \tag{3.30}$$

Moreover, it is easy to show that $Q_1^{-1} < S$ in (3.27) . Thus, the minimization of $Trace(S)$ implies the minimization of the guaranteed cost in (3.30). This completes the proof. ■

3.3.2 Actuator and Sensor Fault Estimation

The results for fault estimation are presented in this section. A lemma is introduced first.

Lemma 3.3.1 *Based on Assumption 3.2.1, there exist T_1 and T_2, so that*

$$z = \begin{bmatrix} z_1 \\ z_2 \end{bmatrix} = T_1\begin{bmatrix} x_1 \\ x_2 \end{bmatrix}, \quad w = \begin{bmatrix} w_1 \\ w_2 \end{bmatrix} = T_2\begin{bmatrix} \omega_{1f} \\ \omega_{2f} \end{bmatrix}, \tag{3.31}$$

and the corresponding transformed system matrices for Σ_1 in (3.6) become:

$$T_1AT_1^{-1} = \begin{bmatrix} A_1 & A_2 \\ A_3 & A_4 \end{bmatrix},\ T_1 = \begin{bmatrix} G_1 \\ G_2 \end{bmatrix},\ T_1B = \begin{bmatrix} B_1 \\ B_2 \end{bmatrix},$$

$$T_1F = \begin{bmatrix} F_1 \\ 0 \end{bmatrix},\ T_2CT_1^{-1} = \begin{bmatrix} C_1 & 0 \\ 0 & C_4 \end{bmatrix},\ T_2D = \begin{bmatrix} 0 \\ D_2 \end{bmatrix},$$

where $T_1 \in \mathbb{R}^{m\times m}, T_2 \in \mathbb{R}^{n\times n}, z_1 \in \mathbb{R}^p, w_1 \in \mathbb{R}^p, A_1 \in \mathbb{R}^{p\times p}, A_4 \in \mathbb{R}^{(m-p)\times(m-p)}, G_1 \in \mathbb{R}^{p\times m}, B_1 \in \mathbb{R}^{p\times l}, F_1 \in \mathbb{R}^{p\times p}, C_1 \in \mathbb{R}^{p\times p}, C_4 \in \mathbb{R}^{(n-p)\times(m-p)}, D_2 \in \mathbb{R}^{(n-p)\times q}$. F_1 and C_1 are invertible.

Proof. See [109]. ■

Hence, Σ_1 can be transformed into two subsystems,

$$\Sigma_{11}: \begin{cases} \dot{z}_1(t) = A_1z_1(t) + A_2z_2(t) + G_1g(T_1^{-1}z(t)) + B_1u(t) + F_1f_a(t) \\ w_1(t) = C_1z_1(t) \end{cases}, \tag{3.32}$$

$$\Sigma_{12}: \begin{cases} \dot{z}_2(t) = A_4z_2(t) + A_3z_1(t) + G_2g(T_1^{-1}z(t)) + B_2u(t) \\ w_2(t) = C_4z_2(t) + D_2f_s(t) \end{cases}. \tag{3.33}$$

Remark 3.3.2 *The pair (A_4, C_4) is detectable when Assumption 3.2.2 holds [109].*

A new state $z_3(t) \in \mathbb{R}^{n-p}$ is introduced as a filtered version of $w_2(t)$,

$$\dot{z}_3(t) = -A_f z_3(t) + A_f C_4 z_2(t) + A_f D_2 f_s(t), \tag{3.34}$$

where $A_f \in \mathbb{R}^{(n-p)\times(n-p)}$ is a stable matrix. Define $\tilde{z}_2 = [z_2^\top \ z_3^\top]^\top \in \mathbb{R}^{m+n-2p}$. Then Σ_{11} becomes:

$$\Sigma_{13}: \begin{cases} \dot{z}_1(t) = A_1 z_1(t) + \tilde{A}_2 \tilde{z}_2(t) + G_1 g(T_1^{-1} z(t)) + B_1 u(t) + F_1 f_a(t) \\ w_1(t) = C_1 z_1(t) \end{cases}, \tag{3.35}$$

where $\tilde{A}_2 = \begin{bmatrix} A_2 & 0 \end{bmatrix} \in \mathbb{R}^{p\times(m+n-2p)}$. Via augmentation, Σ_{12} then becomes:

$$\Sigma_{14}: \begin{cases} \dot{\tilde{z}}_2(t) = \tilde{A}_4 \tilde{z}_2(t) + \tilde{A}_3 z_1(t) + \tilde{G}_2 g(T_1^{-1} z(t)) + \tilde{B}_2 u(t) + \tilde{D}_2 f_s(t) \\ w_3(t) = \tilde{C}_3 \tilde{z}_2(t) \end{cases}, \tag{3.36}$$

where $\tilde{A}_4 \in \mathbb{R}^{(m+n-2p)\times(m+n-2p)}$, $\tilde{A}_3 \in \mathbb{R}^{(m+n-2p)\times p}$, $\tilde{B}_2 \in \mathbb{R}^{(m+n-2p)\times l}$, $\tilde{G}_2 \in \mathbb{R}^{(m+n-2p)\times m}$, $\tilde{D}_2 \in \mathbb{R}^{(m+n-2p)\times q}$ and $\tilde{C}_3 \in \mathbb{R}^{(n-p)\times(m+n-2p)}$. The matrices can be obtained as:

$$\tilde{A}_4 = \begin{bmatrix} A_4 & 0 \\ A_f C_4 & -A_f \end{bmatrix}, \tilde{A}_3 = \begin{bmatrix} A_3 \\ 0 \end{bmatrix}, \tilde{G}_2 = \begin{bmatrix} G_2 \\ 0 \end{bmatrix},$$

$$\tilde{B}_2 = \begin{bmatrix} B_2 \\ 0 \end{bmatrix}, \tilde{D}_2 = \begin{bmatrix} 0 \\ A_f D_2 \end{bmatrix}, \tilde{C}_3 = \begin{bmatrix} 0 & I_{n-p} \end{bmatrix}.$$

From the above augmented system Σ_{14}, the sensor faults are transformed into a new form similar to actuator faults. It is easy to prove that $(\tilde{A}_4, \tilde{C}_3)$ is observable if (A_4, C_4) is detectable [110].

For systems (3.35) and (3.36), the following two adaptive observers are built:

$$\Sigma_{41}: \begin{cases} \dot{\hat{z}}_1(t) = A_1 \hat{z}_1(t) + \tilde{A}_2 \hat{\tilde{z}}_2(t) + G_1 g(T_1^{-1} \hat{z}(t)) + B_1 u(t) + F_1 \hat{f}_a(t) + L_1(\hat{w}_1 - w_1) \\ \hat{w}_1(t) = C_1 \hat{z}_1(t) \end{cases}, \tag{3.37}$$

$$\Sigma_{42}: \begin{cases} \dot{\hat{\tilde{z}}}_2(t) = \tilde{A}_4 \hat{\tilde{z}}_2(t) + \tilde{A}_3 C_1^{-1} w_1(t) + \tilde{G}_2 g(T_1^{-1} \hat{z}(t)) + \tilde{B}_2 u(t) + \tilde{D}_2 \hat{f}_s(t) + L_2(\hat{w}_3 - w_3) \\ \hat{w}_3(t) = \tilde{C}_3 \hat{\tilde{z}}_2(t) \end{cases}, \tag{3.38}$$

where $\hat{z}_1$, $\hat{\tilde{z}}_2$, $\hat{z}$, $\hat{f}_a$, $\hat{w}_1$, $\hat{\tilde{z}}_2$, $\hat{f}_s$, and $\hat{w}_3$ are the estimates of z_1, $\tilde{z}_2$, z, f_a, w_1, $\tilde{z}_2$, f_s, and w_3, respectively. $L_1 \in \mathbb{R}^{p\times p}$ and $L_2 \in \mathbb{R}^{(m+n-2p)\times(n-p)}$ are the two observer gains to be designed.

Let $e_1(t) = \hat{z}_1 - z_1$, $e_2(t) = \hat{\tilde{z}}_2 - \tilde{z}_2$, $e_{fa}(t) = \hat{f}_a(t) - f_a(t)$, $\dot{e}_{fa}(t) = \dot{\hat{f}}_a(t) - \dot{f}_a(t)$, $e_{fs}(t) = \hat{f}_s(t) - f_s(t)$, $\dot{e}_{fs}(t) = \dot{\hat{f}}_s(t) - \dot{f}_s(t)$, $e_{w1} = \hat{w}_1 - w_1 = C_1 e_1$, $e_{w3} = \hat{w}_3 - w_3 = \tilde{C}_3 e_2$ and $g_e(t) = g(T_1^{-1}\hat{z}(t)) - g(T_1^{-1}z(t))$. Then, we have the error dynamics as:

$$\begin{cases} \dot{e}_1(t) = (A_1 + L_1 C_1)e_1(t) + \tilde{A}_2 e_2(t) + G_1 g_e(t) + F_1 e_{fa}(t) \\ \dot{e}_2(t) = (\tilde{A}_4 + L_2 \tilde{C}_3)e_2(t) + \tilde{G}_2 g_e(t) + \tilde{D}_2 e_{fs}(t) \end{cases}. \tag{3.39}$$

The following Lemma is needed for the subsequent results.

Lemma 3.3.2 *For a given positive scalar μ_0 and a symmetric positive definite matrix $R_0 \in \mathbb{R}^{r_0 \times r_0}$, the following conditions holds[31]:*

$$2a^\top b \leq \frac{1}{\mu_0} a^\top R_0 a + \mu_0 b^\top R_0^{-1} b, \tag{3.40}$$

where $a, b \in \mathbb{R}^{r_0}$ and r_0 is a random real integer.

Based on the above lemma, the following adaptive estimation algorithm is obtained.

Theorem 3.3.3 *For the error dynamics system (3.39), given small positive scalars $\mu_1 > 0$ and $\mu_2 > 0$, if there exist symmetric positive definite matrices $P_2 \in \mathbb{R}^{p\times p}$, $P_4 \in \mathbb{R}^{p\times p}$, $P_3 \in \mathbb{R}^{(m+n-2p)\times(m+n-2p)}$, $P_5 \in \mathbb{R}^{q\times q}$, $R_1 \in \mathbb{R}^{p\times p}$, $R_2 \in \mathbb{R}^{q\times q}$ and any matrix $E_1 \in \mathbb{R}^{p\times p}$, $E_2 \in \mathbb{R}^{(n-p)\times q}$, $M_1 \in \mathbb{R}^{p\times p}$, $M_2 \in \mathbb{R}^{(m+n-2p)\times(n-q)}$ such that a solution $\sigma > 0$ exists for the following optimization problem:*

$$\min_{E_1,E_2,P_2,P_3,P_4,P_5,R_1,R_2,M_1,M_2} \quad \sigma \tag{3.41}$$

subject to the following matrix inequalities

$$\Omega_5 = \begin{bmatrix} \sigma I & P_2F_1 - C_1^\top E_1 \\ P_2F_1 - C_1^\top E_1 & \sigma I \end{bmatrix} > 0, \tag{3.42}$$

$$\Omega_6 = \begin{bmatrix} \sigma I & P_3\tilde{D}_2 - \tilde{C}_3^\top E_2 \\ P_3\tilde{D}_2 - \tilde{C}_3^\top E_2 & \sigma I \end{bmatrix} > 0, \tag{3.43}$$

and

$$\Omega_7 = \begin{bmatrix} \Delta_7^{11} & P_2\tilde{A}_2 & P_2G_1 & \Delta_7^{14} & 0 \\ * & \Delta_7^{22} & P_3\tilde{G}_2 & -\frac{1}{\nu_1}\tilde{A}_2^\top P_2F_1 & \Delta_7^{25} \\ * & * & -I & -\frac{1}{\nu_1}G_1^\top P_2F_1 & -\frac{1}{\nu_2}\tilde{G}_2^\top P_3\tilde{D}_2 \\ * & * & * & \Delta_7^{44} & 0 \\ * & * & * & 0 & \Delta_7^{55} \end{bmatrix} < 0, \tag{3.44}$$

where $\Delta_7^{11} = P_2A_1 + A_1^\top P_2 + M_1C_1 + C_1^\top M_1^\top + \alpha_1 l_f^2 \parallel T_1^{-1} \parallel^2 I$, $\Delta_7^{22} = P_3\tilde{A}_4 + \tilde{A}_4^\top P_3 + M_2\tilde{C}_3 + \tilde{C}_3^\top M_2^\top + \alpha_2 l_f^2 \parallel T_1^{-1} \parallel^2 I$, $\Delta_7^{14} = -\frac{1}{v_1}A_1^\top P_2F_1 - \frac{1}{v_1}C_1^\top M_1^\top F_1$, $\Delta_7^{25} = -\frac{1}{v_2}\tilde{A}_4^\top P_3\tilde{D}_2 - \frac{1}{v_2}\tilde{C}_3^\top M_2^\top \tilde{D}_2$, $\Delta_7^{44} = -2\frac{1}{v_1}F_1^\top P_2F_1 + \frac{1}{\mu_1 v_1}R_1$, $\Delta_7^{55} = -2\frac{1}{v_2}\tilde{D}_2^\top P_3\tilde{D}_2 + \frac{1}{\mu_2 v_2}R_2$, *and* $M_1 = P_2L_1, M_2 = P_3L_2$.

Then the following adaptive estimation algorithm:

$$\begin{cases} \dot{\hat{f}}_a(t) = -P_4^{-1}E_1^\top[\dot{e}_{w1}(t) + v_1e_{w1}(t)] \\ \dot{\hat{f}}_s(t) = -P_5^{-1}E_2^\top[\dot{e}_{w3}(t) + v_2e_{w3}(t)] \end{cases} \tag{3.45}$$

can render $e_1(t)$, $e_2(t)$, $e_{fa}(t)$ *and* $e_{fs}(t)$ *uniformly ultimately bounded so that the error system is stabilized.* L_1 *and* L_2 *can be obtained from* $L_1 = P_2^{-1}M_1$ *and* $L_2 = P_3^{-1}M_2$, *respectively.*

Proof. The following Lyapunov candidate is chosen here:

$$V_3(t) = e_1^\top(t)P_2e_1(t) + e_2^\top(t)P_3e_2(t) + \frac{1}{v_1}e_{fa}^\top(t)P_4e_{fa}(t) + \frac{1}{v_2}e_{fs}^\top(t)P_5e_{fs}(t). \tag{3.46}$$

According to the Lipschitz assumption, $\parallel g(x_1(t)) - g(x_2(t)) \parallel \leq l_f \parallel (x_1(t) - x_2(t)) \parallel$. Therefore,

$$\parallel l_f e_x(t) \parallel^2 - \parallel g_e(t) \parallel^2 \geq 0, \tag{3.47}$$

where $e_x(t) = \hat{x} - x = T_1^{-1}(\hat{z} - z)$. There exist $\alpha_1 > 0$ and $\alpha_2 > 0$, so that

$$\alpha_1 l_f^2 \parallel T_1^{-1} \parallel^2 \parallel e_1 \parallel^2 + \alpha_2 l_f^2 \parallel T_1^{-1} \parallel^2 \parallel e_2 \parallel^2 - \parallel g_e(t) \parallel^2 \geq 0. \tag{3.48}$$

The time derivative of (3.46) can be written as

$$\begin{aligned} \dot{V}_3(t) \leq\ & 2e_1^\top(t)P_2[(A_1 + L_1C_1)e_1(t) + \tilde{A}_2e_2(t) + G_1g_e(t) + F_1e_{fa}(t)] \\ & + 2e_2^\top P_3[(\tilde{A}_4 + L_2\tilde{C}_3)e_2(t) + \tilde{G}_2g_e(t) + \tilde{D}_2e_{fs}(t)] \\ & + \frac{2}{v_1}e_{fa}^\top(t)P_4[\dot{\hat{f}}_a(t) - \dot{f}_a(t)] + \frac{2}{v_2}e_{fs}^\top(t)P_5[\dot{\hat{f}}_s(t) - \dot{f}_s(t)] \\ & + \alpha_1 l_f^2 \parallel T_1^{-1} \parallel^2 \parallel e_1 \parallel^2 + \alpha_2 l_f^2 \parallel T_1^{-1} \parallel^2 \parallel e_2 \parallel^2 - \parallel g_e(t) \parallel^2 . \end{aligned} \tag{3.49}$$

Let

$$\begin{aligned} \dot{\hat{f}}_a(t) &= -P_4^{-1}E_1^\top[\dot{e}_{w1}(t) + v_1e_{w1}(t)] \\ &= -P_4^{-1}E_1^\top C_1\left[(A_1 + L_1C_1)e_1(t) + \tilde{A}_2e_2(t) + G_1g_e(t) + F_1e_{fa}(t)\right] - v_1P_4^{-1}E_1^\top C_1e_1(t), \\ \dot{\hat{f}}_s(t) &= -P_5^{-1}E_2^\top[\dot{e}_{w3}(t) + v_2e_{w3}(t)] \\ &= -P_5^{-1}E_2^\top\tilde{C}_3\left[(\tilde{A}_4 + L_2\tilde{C}_3)e_2(t) + \tilde{G}_2g_e(t) + \tilde{D}_2e_{fs}(t)\right] - v_2P_5^{-1}E_2^\top\tilde{C}_3e_2(t), \end{aligned}$$

and

$$P_2F_1 = C_1^\top E_1, \tag{3.50}$$

$$P_3\tilde{D}_2 = \tilde{C}_3^\top E_2. \tag{3.51}$$

Eq. (3.50) and Eq. (3.51) represent equality constraints that are difficulty to satisfy together with the condition (3.44). Alternatively, they can be approximated in the LMI form of minimizing σ subject to the following inequalities[31]:

$$\begin{bmatrix} \sigma I & P_2F_1 - C_1^\top E_1 \\ P_2F_1 - C_1^\top E_1 & \sigma I \end{bmatrix} > 0, \tag{3.52}$$

$$\begin{bmatrix} \sigma I & P_3\tilde{D}_2 - \tilde{C}_3^\top E_2 \\ P_3\tilde{D}_2 - \tilde{C}_3^\top E_2 & \sigma I \end{bmatrix} > 0. \tag{3.53}$$

Then Eq. (3.49) becomes:

$$\begin{aligned} \dot{V}_3(t) =& 2e_1^\top(t)P_2[(A_1 + L_1C_1)e_1(t) + \tilde{A}_2e_2(t) + G_1g_e(t)] + 2e_2^\top P_3[(\tilde{A}_4 + L_2\tilde{C}_3)e_2(t) + \tilde{G}_2g_e(t)] \\ & - 2\frac{1}{v_1}e_{fa}^\top(t)E_1^\top C_1\left[(A_1 + L_1C_1)e_1(t) + \tilde{A}_2e_2(t) + G_1g_e(t) + F_1e_{fa}(t)\right] \\ & - 2\frac{1}{v_1}e_{fa}^\top(t)P_4\dot{f}_a(t) - 2\frac{1}{v_2}e_{fs}^\top(t)E_2^\top\tilde{C}_3\left[(\tilde{A}_4 + L_2\tilde{C}_3)e_2(t) + \tilde{G}_2g_e(t) + \tilde{D}_2e_{fs}(t)\right] \\ & - 2\frac{1}{v_2}e_{fs}^\top(t)P_5\dot{f}_s(t) - \parallel g_e(t) \parallel^2 + \alpha_1 l_f^2 \parallel T^{-1} \parallel^2 \parallel e_1 \parallel^2 + \alpha_2 l_f^2 \parallel T^{-1} \parallel^2 \parallel e_2 \parallel^2 . \end{aligned} \tag{3.54}$$

From *Lemma* 3.3.2, the following can be derived:

$$\begin{aligned} -2e_{fa}^\top(t)P_4\dot{f}_a(t) &\leq \frac{1}{\mu_1}[-e_{fa}(t)]^\top R_1[-e_{fa}(t)] + \mu_1[P_4\dot{f}_a(t)]^\top R_1^{-1}[P_4\dot{f}_a(t)] \\ &\leq \frac{1}{\mu_1}e_{fa}^\top(t)R_1e_{fa}(t) + \mu_1 f_{m1}^2\lambda_{max}(P_4^\top R_1^{-1}P_4), \end{aligned} \tag{3.55}$$

and

$$\begin{aligned} -2e_{fs}^\top(t)P_5\dot{f}_s(t) &\leq \frac{1}{\mu_2}[-e_{fs}(t)]^\top R_2[-e_{fs}(t)] + \mu_2[P_5\dot{f}_s(t)]^\top R_2^{-1}[P_5\dot{f}_s(t)] \\ &\leq \frac{1}{\mu_2}e_{fs}^\top(t)R_2e_{fs}(t) + \mu_2 f_{m2}^2\lambda_{max}(P_5^\top R_2^{-1}P_5), \end{aligned} \tag{3.56}$$

where f_{m1} and f_{m2} are the maximum values of $\dot{f}_a(t)$ and $\dot{f}_s(t)$, respectively. $\lambda_{max}(P_4^\top R_1^{-1}P_4)$ and $\lambda_{max}(P_5^\top R_2^{-1}P_5)$ are the maximum eigenvalues of $[(P_4^\top R_1^{-1}P_4)]$ and $[(P_5^\top R_2^{-1}P_5)]$, re-

spectively. Then, Eq. (3.54) becomes:

$$\begin{aligned}\dot{V}_3(t) \leq & 2e_1^\top(t)P_2[(A_1+L_1C_1)e_1(t)+\tilde{A}_2e_2(t)+G_1g_e(t)]+2e_2^\top P_3[(\tilde{A}_4+L_2\tilde{C}_3)e_2(t)+\tilde{G}_2g_e(t)] \\ & -2\frac{1}{v_1}e_{fa}^\top(t)E_1^\top C_1\left[(A_1+L_1C_1)e_1(t)+\tilde{A}_2e_2(t)+G_1g_e(t)+F_1e_{fa}(t)\right] \\ & +\frac{1}{\mu_1 v_1}e_{fa}^\top(t)R_1e_{fa}(t)-2\frac{1}{v_2}e_{fs}^\top(t)E_2^\top\tilde{C}_3\left[(\tilde{A}_4+L_2\tilde{C}_3)e_2(t)+\tilde{G}_2g_e(t)+\tilde{D}_2e_{fs}(t)\right] \\ & +\frac{1}{\mu_2 v_2}e_{fs}^\top(t)R_2e_{fs}(t)-\parallel g_e(t)\parallel^2+\alpha_1 l_f^2\parallel T^{-1}\parallel^2\parallel e_1\parallel^2+\alpha_2 l_f^2\parallel T^{-1}\parallel^2\parallel e_2\parallel^2 \\ & +\frac{\mu_1}{v_1}f_{m1}^2\lambda_{max}(P_4^\top R_1^{-1}P_4)+\frac{\mu_2}{v_2}f_{m2}^2\lambda_{max}(P_5^\top R_2^{-1}P_5) \\ = & \tilde{e}^\top(t)\Omega_7\tilde{e}(t)+\frac{\mu_1}{v_1}f_{m1}^2\lambda_{max}(P_4^\top R_1^{-1}P_4)+\frac{\mu_2}{v_2}f_{m2}^2\lambda_{max}(P_5^\top R_2^{-1}P_5),\end{aligned} \tag{3.57}$$

where $\tilde{e}(t)=\begin{bmatrix} e_1^\top(t) & e_2^\top(t) & g_e^\top(t) & e_{fa}^\top(t) & e_{fs}^\top(t)\end{bmatrix}^\top$.

When (3.44) is satisfied,we can have:

$$\dot{V}_3(t) < -\lambda_{min}(-\Omega_7)||\tilde{e}(t)||^2+\frac{\mu_1}{v_1}f_{m1}^2\lambda_{max}(P_4^\top R_1^{-1}P_4)+\frac{\mu_2}{v_2}f_{m2}^2\lambda_{max}(P_5^\top R_2^{-1}P_5), \tag{3.58}$$

where $\lambda_{min}(-\Omega_7)$ denotes the minimum eigenvalue of $[-\Omega_7]$. Therefore, for

$$\lambda_{min}(-\Omega_7)||\tilde{e}(t)||^2 > \frac{\mu_1}{v_1}f_{m1}^2\lambda_{max}(P_4^\top R_1^{-1}P_4)+\frac{\mu_2}{v_2}f_{m2}^2\lambda_{max}(P_5^\top R_2^{-1}P_5),$$

$\dot{V}_3(t) < 0$. It means the estimation will always converge until $||\tilde{e}(t)||^2$ arrives at

$$[\frac{\mu_1}{v_1}f_{m1}^2\lambda_{max}(P_4^\top R_1^{-1}P_4)+\frac{\mu_2}{v_2}f_{m2}^2\lambda_{max}(P_5^\top R_2^{-1}P_5)]/\lambda_{min}(-\Omega_7),$$

which means the estimation errors of both the actuator faults and sensor faults will be uniformly bounded. This is the end of the proof. ■

3.3.3 Fault-Tolerant Shape Control

In this part, considering the simultaneous occurrences of time-varying actuator and sensor faults, a novel yet straightforward shape control compensation algorithm based on virtual actuator and virtual sensor is designed, which is to be added to the normal control law in order to reduce/eliminate the impact of the faults on the system,

$$\bar{u}(t)=\bar{u}_N(t)+\bar{v}(t) \tag{3.59}$$

where $\bar{u}_N(t)=[0,\ u_N^\top(t)]^\top\in\mathbb{R}^{(l+q)\times 1}$ is the augmented normal controller.

$\bar{v}(t)=[v_s^\top(t),\ v_a^\top(t)]^\top\in\mathbb{R}^{(l+q)\times 1}$ is the augmented virtual actuator and virtual sensor, where $v_a(t)\in\mathbb{R}^{l\times 1}$ is the virtual actuator and $v_s(t)\in\mathbb{R}^{q\times 1}$ is the virtual sensor. The signal

$\bar{u}(t)$ in Eq. (3.8) is then determined and computed according to Eq. (3.59) while the virtual actuator and the virtual sensor can be obtained as:

$$\begin{cases} v_a(t) = -S_f \hat{f}_a(t) \\ v_s(t) = -\hat{f}_s(t) \end{cases} \tag{3.60}$$

where S_f satisfies $BS_f = F$, such that the additional term in Eq. (3.60) can compensate for the fault effects.

Substitute Eq. (3.60) into Eq. (3.6) and the dynamic system with actuator and sensor compensation can be expressed as follows:

$$\begin{cases} \dot{x}(t) = Ax(t) + g(x(t)) + Bu_N(t) + F[f_a(t) - \hat{f}_a(t)] \\ \omega_c(t) = Cx(t) + D[f_s(t) - \hat{f}_s(t)] \end{cases} \tag{3.61}$$

Based on Eq.(3.45), the fast convergence of the fault estimation can be reached while the system stability can be guaranteed by $u_N(t)$ in Eq.(3.10).

Remark 3.3.3 *The main objective of this chapter is to achieve fault-tolerant shape control so that the PSD function of a particulate process can track a given target shape in the presence of simultaneous actuator and sensor faults. The augment adaptive control law may reduce (or even eliminate) the impact of faults. It is worth pointing out that this adaptive control law can also achieve tracking in the fault-free situation. In that case,* $\hat{f}_a(t) = 0$, $\hat{f}_s(t) = 0$ *and* $\bar{u}(t) = \bar{u}_N(t)$.

3.4 Overall Adaptive Fault-Tolerant Control Scheme

In Fig. 3.1, the block diagram of the proposed fault-tolerant shape control scheme for PSD system under simultaneous actuator and sensor faults is given.

The detailed implementation of the scheme is sketched here:

1. According to the target PSD shape, Chose the appropriate n B-spline basis functions $\Gamma_i (i = 1, 2, \cdots, n)$;

2. Calculate the target pseudo weights vector ω_g according to Eq. (3.7);

3. Measure the system output PDF, calculate the pseudo weights vector $\omega(t)$ according to Eq. (3.1);

4. Design an optimal shape controller for the fault-free system based on Theorem 3.3.2;

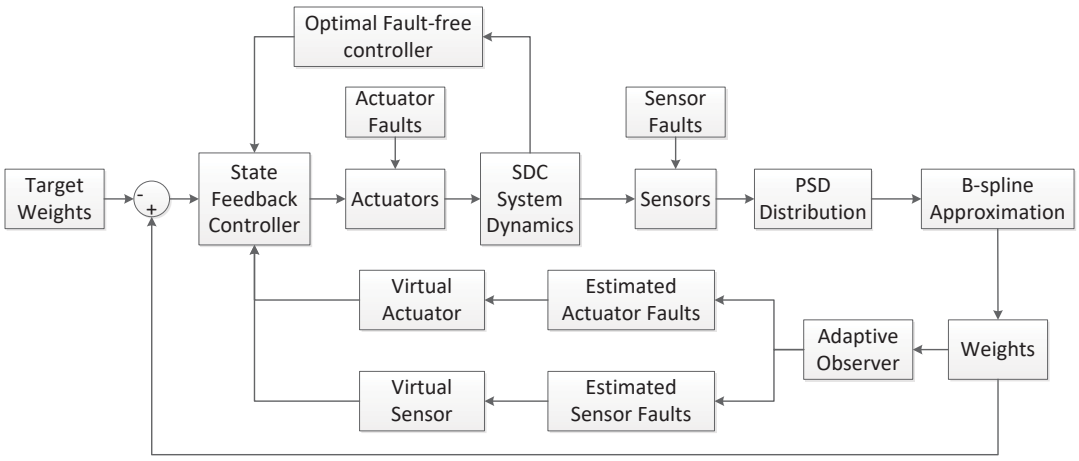

Figure 3.1: Overall adaptive fault-tolerant control scheme

5. Simultaneously estimate the actuator and sensor faults according to Theorem 3.3.3;

6. Design the FTSC law based on the optimal fault-free controller by adding a virtual actuator and a virtual sensor according to Eq. (3.61).

3.5 Simulation of PSD Shape Control in Emulsion Polymerization

The process of emulsion polymerization in polymer industry is used as a simulation example in this work. The main target is to regulate the full PSD shape, which is an important process as many properties of the polymer product are decided by the full PSD [111]. The control of emulsion polymerization systems is a well-studied topic. However, the existing results are mainly based on the high order discretized PBE equation. In [111], based on the discretized population balance model of the semibatch VAc/BuA emulsion copolymerization system, a model order reduction technique using principal component analysis (PCA) was proposed for model predictive control (MPC). Satisfactory control performance was achieved. However, to derive the controllable model for MPC, a numerical discretization process, and a model reduction step should be applied, which cause complexities in computation. In this work, an alternative method is proposed to use the distribution shape control scheme.

A semibatch VAc/BuA emulsion copolymerization system proposed in [111] is adopted in Figure 3.2 for illustration. The target particle size distribution is shown in Fig. 3.3.

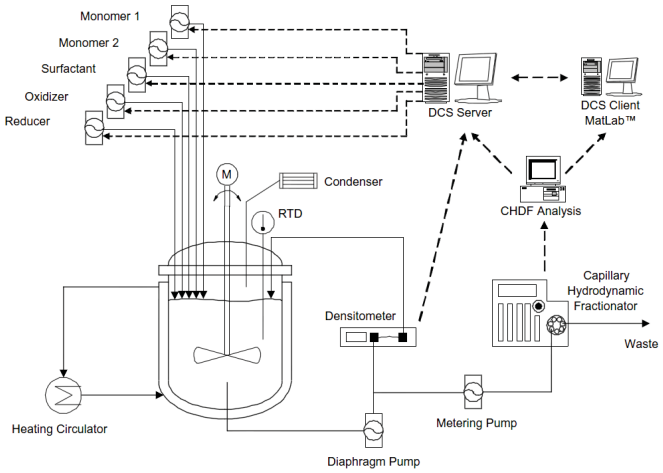

Figure 3.2: Schematic diagram of the experimental system

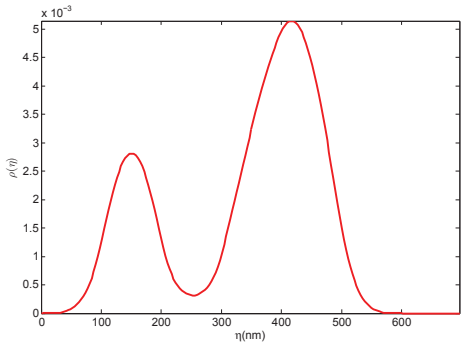

Figure 3.3: Particle distribution curve

The inputs of the emulsion polymerization system are the feed rates of vinyl acetate (VAc), butyl acrylate (BuA), tert-butyl hydroperoxide (tBHP) and surfactant, respectively. For simple demonstration, actuation saturation is not considered in this chapter. A state vector of four elements is selected to construct the state space model, which represents the values of the particle distribution at four discretization point. Then, the emulsion polymerization system can be represented according to Eq. (3.6), where the measured output PSD shape function of the considered stochastic system can be expressed as a function of all the pre-specified B-spline basis functions. Unlike the system model established in [111], which is derived based on the reduced order PBE equation, the system equation of Eq. (3.6) in this work is assumed to be identified using the process data. The dynamics between the weights and the control input can be well represented by choosing the proper

basis B-spline functions. The dynamics can be expressed as Eq.(3.7). It is assumed that the target distribution function $\rho_g(\eta)$ belongs to the following functional space:

$$\rho_g(\eta) \in \Omega_0 = \{\rho | \sqrt{\rho_u(\eta,\, t)} = \frac{\Gamma(\eta)\omega(t)}{\sqrt{\omega^\top(t)\Gamma_f\omega(t)}}\}, \tag{3.62}$$

where $\omega(t)$ denotes the weight vector and $\omega \in \mathbb{R}^{4\times 1}, \omega \geq 0$.

Remark 3.5.1 *The system matrices can be identified based on the input and the output pseudo weights corresponding to the selected B-spline functions. It is reasonable as there is abundant process data to identify the system matrices.*

On-line measurement of the distribution of particle size, in this case, is essential and can be achieved by using proper instrumentation. For example, the PSD measurements can be obtained by a capillary hydrodynamic fractionator. In addition, the combination of near-infrared spectroscopy (NIRS) method and fiber optic technology are widely adopted for reduction of time delays normally involved with sample preparation [65].

The PSD is formulated as in Eq. (3.1) with the B-spline functions $\Gamma_i(\eta), (i = 1,2,3)$ corresponding to Fig. 3.3 chosen to be:

$$\Gamma_1(\eta) = \begin{cases} 0.5(\frac{\eta}{100})^2, & 0 \leq \eta < 100 \\ -(\frac{\eta}{100})^2 + 3\frac{\eta}{100} - 1.5, & 100 \leq \eta < 200 \\ 0.5(3 - \frac{\eta}{100})^2 & 200 \leq \eta < 300 \end{cases}$$

$$\Gamma_2(\eta) = \begin{cases} 0.5(\frac{\eta}{100} - 1)^2, & 100 \leq \eta < 200 \\ -(\frac{\eta}{100})^2 + 5\frac{\eta}{100} - 5.5, & 200 \leq \eta < 300 \\ 0.5(4 - \frac{\eta}{100})^2, & 300 \leq \eta < 400 \end{cases}$$

$$\Gamma_3(\eta) = \begin{cases} 0.5(\frac{\eta}{100} - 2)^2, & 200 \leq \eta < 300 \\ -(\frac{\eta}{100})^2 + 7\frac{\eta}{100} - 11.5, & 300 \leq t < 400 \\ 0.5(5 - \frac{\eta}{100})^2, & 400 \leq \eta < 500 \end{cases}$$

$$\Gamma_4(\eta) = \begin{cases} 0.5(\frac{\eta}{100} - 3)^2, & 300 \leq \eta < 400 \\ -(\frac{\eta}{100})^2 + 9\frac{\eta}{100} - 19.5), & 400 \leq \eta < 500 \\ 0.5(6 - \frac{\eta}{100})^2, & 500 \leq \eta < 600 \end{cases}$$

After a B-spline approximating procedure, the dynamical relations between ω and u are described by Eq. (3.6) with all the system matrices are identified and here directly given as:

$$A = \begin{bmatrix} -5.8 & -5 & -6 & -8.9 \\ -48.6 & -1.25 & 48.6 & -9.3 \\ -9.3 & -6.5 & -8 & 10 \\ 1.95 & -7 & -1.95 & -2 \end{bmatrix}, B = \begin{bmatrix} 0 & 14 & 0 & 0 \\ 21.6 & 0 & 0 & 0 \\ 0 & 0 & 0 & 12 \\ 0 & 0 & 23 & 0 \end{bmatrix},$$

$$C = \begin{bmatrix} 1 & 0 & 0 & 0 \\ 0 & 1 & 0 & 0 \\ 0 & 0 & 1 & 0 \\ 0 & 0 & 0 & 1 \end{bmatrix}, D = \begin{bmatrix} 0 & 0 \\ 0 & 0 \\ 1 & 0 \\ 0 & 1 \end{bmatrix}, F = \begin{bmatrix} 0 & 14 \\ 21.6 & 0 \\ 0 & 0 \\ 0 & 0 \end{bmatrix},$$

and $g(x) = \frac{1}{1+e^{-x}} - 0.5$ is used to represent the unmodeled dynamics. The desired PSD $\rho^*(y,t)$ is chosen based on Eq. (3.7), with $\omega_g = [4.5,\ 0.1,\ 4,\ 5]^\top$. In the simulation, sensor noise is added to Eq. (3.6). The noise is assumed to be zero mean i.i.d with standard deviation of 0.1. The initial condition in the dynamic weight system is given by Eq. (3.6) with the above matrices and $x(0) = [6,\ 4,\ 6,\ 2]^\top$. The sampling time is 0.1 min.

The simulation is performed for both fault-free and faulty cases to demonstrate the applicability of the proposed method for both conditions. For the first 500 minutes, there were no faults added to the system. Time-varying actuator faults f_a and sensor faults f_s was simultaneously added to the system at the time of 500 minutes. Here, the oscillatory type of fault signals is used.

$$f_a(t) = \begin{bmatrix} 1.5 + 0.1sin(0.0003t) \\ 0.8 + 0.1sin(0.0005t) \end{bmatrix}; f_s(t) = \begin{bmatrix} 0.2 + 0.1sin(0.0003t) \\ 1.5 + 0.1sin(0.0005t) \end{bmatrix}$$

Choosing $v_1 = v_2 = 1$, $\mu_1 = \mu_2 = 1$, according to Theorem 3.3.3, both the actuator faults and sensor faults can be estimated at the same time. The actuator faults and their estimates are shown in Fig.3.4(a), while the sensor faults and their estimates are illustrated in Fig.3.4(b). From the simulation results, it can be seen that the proposed algorithm can be applied in both fault-free and faulty conditions without fault detection module. Moreover, both the actuator and sensor faults can be accurately estimated.

Fig.3.5(a) shows the tracking performance of the pseudo weights. From the figure, we can clearly see that ω converge to $\omega_g = [4.5,\ 0.1,\ 4,\ 5]^\top$ rapidly in only a few iterations in the fault-free condition. After faults occur at the time of 500 minutes, there are noticeable

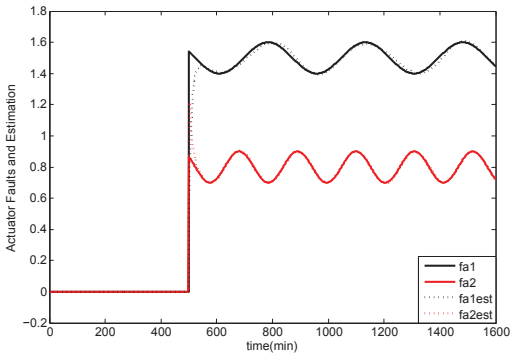

(a) Actuator faults and their estimates

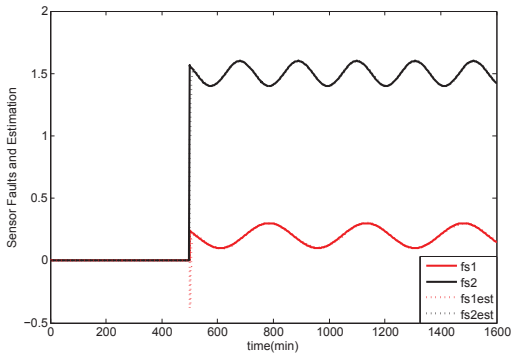

(b) Sensor faults and their estimates

Figure 3.4: Faults and their estimation

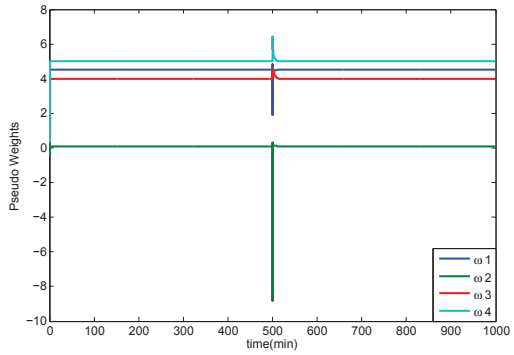

(a) Tracking of weights

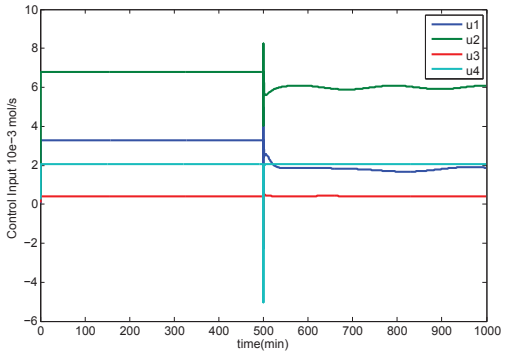

(b) Control inputs

Figure 3.5: Weights and control inputs

spikes caused by the faults for the tracking weights. However, all the weights converge to the target quickly. This can be further illustrated in Fig. 3.5(b), which shows responses of the control inputs. The actuator faults are quickly compensated by the inputs once the faults happened. Finally, Fig.3.6(a) demonstrates the final PSD shape tracking result with excellent performance. In Fig.3.6(b), the 3-D plot of the PSD distribution tracking is presented, which illustrates the shape tracking evolution along the time. In Fig. 3.5(a), 3.5(b) and 3.6(b), only the results of first 1000 minutes are shown.

3.6 Conclusions

In this chapter, the fault-tolerant shape control problem for PSD process under simultaneous actuator and sensor faults is investigated. Simultaneous time-varying actuator and

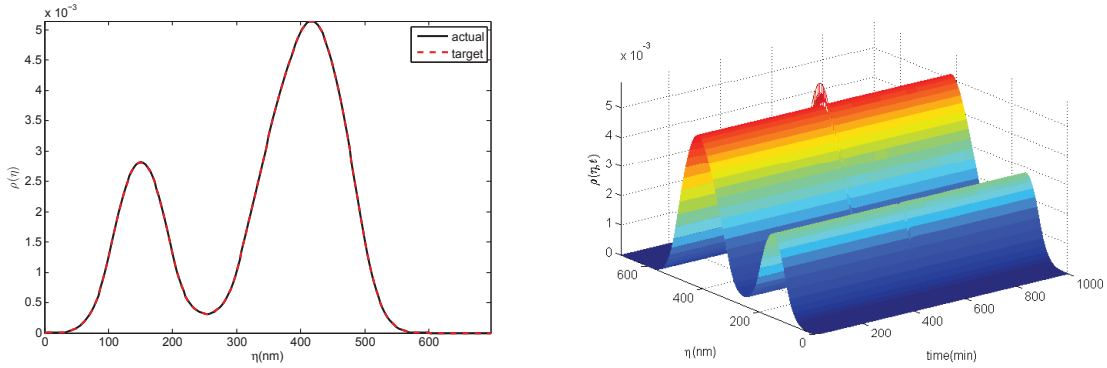

(a) The PSD shape tracking

(b) 3-D PSD distribution response

Figure 3.6: Shape tracking performance

sensor faults can be estimated based on an adaptive observer. A fault-tolerant shape control scheme is proposed using virtual actuator and virtual sensor techniques based on the estimated faults. An optimal performance can be reached in both fault-free and faulty conditions. The simulation results for an emulsion polymerization process example show the proposed method can be applied in both fault-free and faulty cases without a separate fault detection module. Moreover, it can estimate the time-varying actuator and sensor faults simultaneously and achieve a satisfactory tracking performance.

Part II

Adaptive FDD for Rotating Machinery

Fault detection and diagnosis is very crucial when it comes to rotating machines because component failures, especially those of rolling element bearings and gears, can lead to costly downtime or even catastrophic consequences. While analytical model-based FDD techniques significantly rely on accurate system description, the recent development of miniature sensors, wireless communication, and high-efficiency computing techniques has provided researchers with an alternative data-driven approach [84]. Using time-series vibration signal and incorporating certain physical features of the specific practical system can significantly improve FDD performance and decrease computation complexity.

In this part, two data-driven model-based FDD techniques are proposed based on sinusoidal synthesis (SS) model representation constructed by incorporating sinusoidal constraints.

In Chapter 4, an innovative sinusoidal synthesis based adaptive tracking (SSBAT) scheme is proposed for rotating machinery fault diagnosis based on vibration data. Adaptive parameter estimation technique is adopted for establishing the time-varying data-driven model.

In Chapter 5, a minimum entropy deconvolution based sinusoidal synthesis (MEDSS) FDD scheme is proposed, where the phase information of the rotating machinery is further used, following the minimum entropy deconvolution (MED) technique, to improve the SSBAT FDD performance in Chapter 4. A time-weighted-error Kalman filter is used to estimate the MEDSS model parameters adaptively.

Chapter 4

Adaptive Sinusoidal Synthesis Model for Rotating Machinery FDD*

4.1 Introduction

Frequency domain or spectral analysis of vibration signals is commonly used for rotating machinery fault detection. Cyclostationary analysis [112] can take advantage of the stochastic process nature of the vibration signal. Cepstrum analysis [113] is another common technique in this field. In this method, the cepstrum magnitude is used to detect the sidebands associated with time-varying components or to quantify harmonics. Spectral Kurtosis (SK) was proposed for fault detection based on rotating machine vibration data in [114]. SK is a method in which a bandpass filter is selected to maximize the Kurtosis of the resulting filtered signal. The SK method is shown to be effective in rotating machine monitoring and has been receiving wide research attention in the last few years.

In contrast to frequency analysis, time-domain analysis is fast and easy to implement. There have already been a great amount of schemes developed for time-domain analysis. Most methods are applied to the raw signals directly such as Root Mean Square (RMS), Crest Factor (CF), Energy Ration (ER), Kurtosis and Energy Operator (EO) [115]. Among the many commonly used time-domain methods, the Time Synchronous Average Signal (TSA) based method is deemed to be powerful. TSA can be used to remove any signal components that are not synchronous with the rotating bearings or gears. Therefore, random background noises and disturbances can be easily removed. To filter out asynchronous vi-

*Parts of the results in this chapter appeared in *Mechanical Systems and Signal Processing*, vol. 83, pp. 356-370, 2017.

bration and noise, speed or tachometer information is combined with angular re-sampling. TSA method has found successful applications in bearing and gear fault detection [78]. A major drawback of TSA is the significant loss of information contained in the distribution or autocorrelation function, which may contain important information related to possible faults [116].

Adaptive model-based OT methods were recently proposed based on a recursive least-squares [117] and adaptive VKF approach [118]. Online real-time process monitoring has been performed using the adaptive VKF OT techniques [119]. When applying order tracking to rotating machinery fault diagnosis, order amplitudes, as a function of harmonic order and shaft speed, are calculated and analyzed for fault diagnosis purpose. Therefore, this method can be referred to as order domain fault diagnosis. Human experience or intelligent expert system may be needed in OT based fault diagnosis[120][121].

It is known that the vibration feature of a rotating machine usually consists of three major components: a sinusoidal component, an impact caused broadband frequency component and random noise [122]. Therefore, detection of impact-faults such as rotor rubbing, rolling element bearing inner or outer race faults, and gear tooth faults can be improved through prediction based on a sinusoidal restriction [123]. These impact faults are among the most damaging machine faults and it is crucial to detect them before they cause more catastrophic failures. Impact faults are known to periodically excite the rotating machine dynamics with time-localized disturbances. Analysis based on sinusoidal synthesis is well established as a method for synthesizing accurate replicas of musical tones [124]. Sinusoidal expansion and parameter identification methods were also developed and applied to bearing and gear fault detection and prognosis [125]. Recently, adaptive filtering and estimation theory have been utilized for estimation of sinusoidal frequencies and amplitudes [126][127][128]. A discrete-time version of the frequency estimator model was given in [129] and it was adopted for gear crack fault detection.

As indicated in [115], for a vibration signal, its trend represented by the sinusoidal components is more obvious in frequency domain while the impulse feature of an impact fault is more prominent in the time domain. On the other hand, it is known that an impact fault has a broadband spectrum in the frequency domain, and can sometimes be treated and filtered out as noises. Hence, a time domain featured fault detection scheme that also carries sinusoidal properties of vibration signals is highly suitable since it can take use of both time-domain and frequency domain information. In this chapter, a sinusoidal synthesis based adaptive tracking (SSBAT) scheme is designed and further a fault detection scheme based on SSBAT is proposed. The SSBAT method is constructed based on the harmonic or semi-harmonic structure of the vibration signals, and it leads to a time domain

linear predictor (or filter) in which the sinusoidal properties are explicitly incorporated. Unlike AR based methods, the scheme considered in this work is based on a time-series model constructed by incorporating the sinusoidal constraints. It can predict future vibration samples based on a sum of sinusoidal components while the number of sinusoids and the rotating speed can be unknown. The advantage of low computation complexity and recursive form from linear predictors are retained in this method. The parameters of the predictor (filter) are updated continuously via adaptive estimation. This makes it possible to synthesize the vibration signal with a low order but time-varying SSBAT model. Moreover, no prior knowledge such as data-fitting under no-fault conditions is needed in this approach. Different from the frequency estimation (identification) problem, which in its own right an interesting research topic with many results produced recently [127][130], the SSBAT method proposed in this chapter is not focused on identifying amplitudes, frequencies, and phases of the sinusoidal components but rather focused on vibration trending and fault detection problems. Compared to the model based order tracking (OT) methods, the proposed scheme utilizes similar time-domain techniques based on state space modeling. However, the method in this work renders a synthesized time-domain signal, instead of extracting individual order components in OT methods, for impact fault detection. Moreover, the explicit knowledge of the rotating speed is not required for the proposed SSBAT method. Instead, the speed dependent model parameters are estimated during the process.

The remainder of this chapter is organized as follows: The SSBAT model is presented in Section 4.2, together with proofs of tracking stability and parameter convergence. In Section 4.3, the SSBAT model based fault detection approach is proposed. Simulation examples to illustrate tracking performance, parameter convergence, fault detection, and a practical application in turbine rubbing fault detection are given in Section 4.4 and 4.5, respectively. Meanwhile, to verify the effectiveness of the SSBAT method, all the simulation results are compared with the commonly adopted AR and ARMED analysis methods.

4.2 The Sinusoidal Synthesis Based Adaptive Tracking (SSBAT) Scheme and Its Application to Fault Diagnosis

The sinusoidal synthesis approach has been widely adopted in the sound production model [131] and can be applied in vibration signal synthesis [94]. The rotating machinery vibration signal consists of three significant components: 'a sinusoidal component due to time varying loading, a broadband impulsive component due to characteristic impulsive fault signatures, and random noise' [122]. Therefore, the measured vibration signal with

periodic characteristic impulsive fault signatures can be represented as follows:

$$y_m[k] = y_o[k] + d[k] + v[k], \tag{4.1}$$

where $y_m[k]$ is the measured discrete signal at time kT; $y_o[k]$ is the nominal fault-free vibration signal; $d[k]$ denotes the periodic impact fault signal, and $v[k]$ is a Gaussian white noise with mean 0 and variance σ^2. $y_o[k]$ can be represented as the combination of a finite number of harmonic components as follows:

$$y_o[k] = \sum_{i=1}^{m} A_i \cos(kT\omega_i + \phi_i), \tag{4.2}$$

where T is the sampling time; m is the number of sinusoidal components; $A_i \in \mathbb{R}_+$ is the amplitude of the ith component; ω_i is the corresponding frequency, and $\phi_i \in [-\pi, +\pi]$ denotes the initial phase. $d[k]$ can be expressed as a series of impulses convolved with a transmission path from the fault element to the vibration sensor [132]:

$$d[k] = h[k] * (\sum_{j=0}^{\infty} \delta[k - jT_d]), \tag{4.3}$$

where h refers to the vibration transmission path and T_d is the fault period.

4.2.1 Sinusoidal Synthesis Model

The sinusoidal synthesis (SS) model proposed in this section is used to synthesize the nominal signal, i.e. $d[k]$ is assumed to be zero during the derivation of SS filter. The SS module can be expressed in the state space form as Σ_f:

$$\Sigma_f : \begin{cases} x[k+1] = Ax[k] + By_m[k] \\ y[k] = Cx[k] \end{cases}, \tag{4.4}$$

where only $y_m[k]$ is the known (measured) vibration signal, which is represented in Eq. (4.1). $y[k]$ is the SS filtered vibration signal, which is used to synthesize the nominal signal $y_o[k]$.

The scheme consists of a sinusoidal synthesis tracking model and a parameter estimator, hence it is indeed an adaptive tracking model. For designing the model Σ_f, firstly, the system matrices of A, B and C are to be chosen according to the sinusoidal characteristics of the vibration signal. It is known that the z-transform of each sinusoidal component is:

$$y_i[k] = A_i \cos(kT\omega_i + \phi_i) \Rightarrow Y_i(z) = \frac{A_i[z^2 - z\cos(T\omega_i - \phi_i)]}{z^2 - 2z\cos(T\omega_i) + 1} := \frac{N_i(z)}{z^2 - 2zcos(T\omega_i) + 1}, \tag{4.5}$$

where $N_i(z)$ represents the numerator polynomial. Therefore, the nominal signal can be expressed in the z-domain as Eq. (4.6).

$$Y_o(z) = \sum_{i=1}^{m} Y_i(z) = \frac{N(z)}{D(z)}, \tag{4.6}$$

and further

$$Y_o(z)D(z) = N(z), \tag{4.7}$$

where $N(z)$ and $D(z)$ are the numerator and the denominator polynomial of the z-transform of the nominal vibration signal and $D(z)$ is :

$$\begin{aligned} D(z) &= \prod_{i=1}^{m}[z^2 - 2z\cos(T\omega_i) + 1] \\ &= z^{2m} + \beta_{m-1}z^{2m-1} + \beta_{m-2}z^{2m-2} + \cdots + \beta_0 z^m \\ &+ \beta_1 z^{m-1} + \cdots + \beta_{m-2}z^2 + \beta_{m-1}z + 1, \end{aligned} \tag{4.8}$$

where β_is refer to the polynomial coefficients for the denominator. In order to track a sinusoidal signal, the denominator $D(z)$ is of interest and contains the main frequency characteristics. This is similar to the idea of Internal Model Principle [133] in control systems, where the poles of the reference signal $y_m[k]$ should be incorporated in the model. In this case, $D(z)$ is also called a reference generating polynomial. Because the generating polynomial $D(z)$ contains all structural properties of the signal, and such properties are independent of the amplitude and the phase of the reference signal [126], for simplicity, we can assume the signal amplitude as zero in this modeling stage, thus $N(z) = 0$. Eq. (4.7) is then rewritten as follows,

$$\begin{aligned} z^{2m}Y(z) &= -(\beta_{m-1}z^{2m-1} + \beta_{m-2}z^{2m-2} + \cdots + \beta_0 z^m \\ &+ \beta_1 z^{m-1} + \cdots + \beta_{m-2}z^2 + \beta_{m-1}z + 1)Y_o(z), \end{aligned} \tag{4.9}$$

where $Y(z)$ is the filtered vibration signal, and $Y_o(z)$ is the nominal fault-free vibration signal. However the above expression is non-causal and $z^{2m}Y(z)$ cannot be obtained in real time. For causality, one can filter each side of Eq. (4.9) with a $2m$th order stable filter $\frac{1}{\Lambda}$, where Λ is chosen as an arbitrary $2m$th order stable polynomial [134] with all roots inside the unit circle:

$$\Lambda(z) = z^{2m} + \lambda_{2m-1}z^{2m-1} + \cdots + \lambda_1 z + \lambda_0. \tag{4.10}$$

Eq. (4.9) then becomes:

$$\begin{aligned} Y(z) &= [\frac{(\lambda_{2m-1} - \beta_{m-1})z^{2m-1} + (\lambda_{2m-2} - \beta_{m-2})z^{2m-2} + \cdots + (\lambda_m - \beta_0)z^m}{\Lambda(z)} \\ &+ \frac{(\lambda_{m-1} - \beta_1)z^{m-1} + \cdots + (\lambda_0 - 1)}{\Lambda(z)}]Y_o(z), \end{aligned} \tag{4.11}$$

where $\beta_i, i = 0, 1, \cdots, m-1$ are unknown parameters to be estimated. As the nominal vibration signal $y_o[k]$ is unknown, the measured signal $y_m[k]$ can be used to pass through the filter. According to the above $z-$transform, we can easily obtain the matrices of the state space tracking model Σ_f in Eq. (4.4) as:

$$A = \begin{bmatrix} -\lambda_{2m-1} & \cdots & -\lambda_1 & -\lambda_0 \\ 1 & \cdots & 0 & 0 \\ 0 & \cdots & 0 & 0 \\ \vdots & \ddots & \vdots & \vdots \\ 0 & \cdots & 1 & 0 \end{bmatrix}_{2m\times 2m}, B = \begin{bmatrix} 1 \\ 0 \\ \vdots \\ 0 \end{bmatrix}_{2m\times 1}, \lambda = \begin{bmatrix} \lambda_{2m-1} \\ \lambda_{2m-2} \\ \cdots \\ \lambda_1 \\ \lambda_0 - 1 \end{bmatrix}_{2m\times 1},$$

$$C = [\lambda_{2m-1} - \beta_{m-1}, \lambda_{2m-2} - \beta_{m-2}, \cdots, \lambda_m - \beta_0, \cdots, \lambda_1 - \beta_{m-1}, \lambda_0 - 1]_{1\times 2m} = \lambda^T - \beta^T V \tag{4.12}$$

$$\beta = \begin{bmatrix} \beta_{m-1} \\ \beta_{m-2} \\ \cdots \\ \beta_0 \end{bmatrix}_{m\times 1}, V = \begin{bmatrix} 1 & 0 & \cdots & 0 & \cdots & 0 & 1 & 0 \\ 0 & 1 & \cdots & 0 & \cdots & 1 & 0 & 0 \\ \vdots & \vdots & \ddots & \vdots & \iddots & \vdots & \vdots & \vdots \\ 0 & \cdots & 0 & 1 & 0 & \cdots & 0 & 0 \end{bmatrix}_{m\times 2m},$$

where the structures and coefficients of A and B are all known if m, the number of sinusoidal components in the signal, is known. However, in many cases, m is unknown. In this case, a model order of $2n$ is chosen to synthesize the vibration signal. The output matrix of C is dependent on β, which are unknown. The signal tracking problem is then transformed to the parameter estimation problem for C which is determined by β.

4.2.2 Adaptive Parameter Estimation With Recursive Least-Squares (LS) Algorithm

In the proposed SSBAT model, the order $2n$ is not necessarily equal to $2m$ where m is the actual number of sinusoidal components. Usually, $n \neq m$, which means that the proposed SSBAT model is used to synthesize the nominal signal with different number of sinusoidal components. To realize this, the amplitudes, frequencies and phases of sinusoidal components in the synthesis model will be adjusted to fit the original signal adaptively. For the SSBAT model Σ_f defined in Eq. (4.4) and (4.12), an adaptive parameter estimation method

with modified recursive Least-Square (LS) algorithm is adopted to estimate the $\beta[k]$.

$$\begin{aligned}\hat{\beta}[k]^{LS} &:= \arg\min_{\beta,n}\{\frac{1}{k}\sum_{l=1}^{k}(y[l]-C[l]x[l])^T(y[l]-C[l]x[l])+\kappa n\} \\ &= \arg\min_{\beta,n}\{\frac{1}{k}\sum_{l=1}^{k}(y[l]-(\lambda^T-\beta^T[l]V)x[l])^T(y[l]-(\lambda^T-\beta^T[l]V)x[l])+\kappa n\}.\end{aligned} \tag{4.13}$$

Here, the LS algorithm is modified from [135]. $\kappa > 0$ is an given parameter and the term κn is used to penalize and reject the unnecessarily high order models. let $x'[k] := VE(x[k])$. The best model order is selected after comparing Eq. (4.13) with different n. For a given n, a normalized recursive LS algorithm is applied,

$$\begin{cases} \hat{\beta}[k] = \hat{\beta}[k-1] - \gamma\dfrac{P_{k-1}x'[k]\tilde{y}^T[k]}{1+\zeta(x'[k])^T P_{k-1}x'[k]} \\ P_k = P_{k-1} - \gamma\dfrac{P_{k-1}x'[k](x'[k])^T P_{k-1}}{1+\zeta(x'[k])^T P_{k-1}x'[k]} \end{cases}, \tag{4.14}$$

where $\tilde{y}[k] = y_m[k] - \hat{y}[k]$, and

$$y_m[k] = (\lambda^T - \beta^T V)x[k] + v(k),\ \ \hat{y}[k] = (\lambda^T - \hat{\beta}^T[k-1]V)x[k].$$

Here $\gamma > 0$ and $\zeta > 0$ are fixed design parameters of the algorithm. $P > 0$ is the covariance matrix. $y_m[k]$ and $\hat{y}[k]$ are the measured signal and the computed SSBAT model output based on the estimated β, respectively.

4.2.3 Tracking Performance and Parameter Convergence

For the proposed SSBAT model, it is clear that the model in Eq. (4.4) is stable. In this subsection, the tracking and parameter convergence are proved. In the following Lemma 4.2.1, an optimal condition is provided for the selection of the SSBAT model order.

Lemma 4.2.1 *Assume a fault-free vibration signal is comprised of m sinusoidal elements as*

$$y_m[k] = \sum_{i=1}^{m} A_i\cos(kT\omega_i + \phi_i) + v[k]. \tag{4.15}$$

For the SSBAT model to be optimal in the sense that the minimization problem defined in Eq. (4.13) is achieved, it is necessary that $n \leq m$.

Proof: To show this, we can assume the opposite and then show the contradiction. Assume that for the optimal SSBAT, we have $n \geq m$ (but $n < 2m$). The denominator of the z-transform of Eq. (4.15) is given in Eq. (4.8). The optimal SSBAT model of Eq. (4.13) can be expressed as:

$$\hat{y}[k] = \sum_{i=1}^{m} \hat{A}_i \cos(kT\hat{\omega}_i + \hat{\phi}_i) + \sum_{i=m+1}^{n} A_i \cos(kT\hat{\omega}_i + \hat{\phi}_i). \tag{4.16}$$

There exists $\hat{\beta} = [\hat{\beta}_0,\ \hat{\beta}_1,\ \cdots,\ \hat{\beta}_{m-1}]^T$, so that when the optimal estimation is reached,

$$E[\sum_{i=1}^{m} \hat{A}_i \cos(kT\hat{\omega}_i + \hat{\phi}_i)] = E(y_m[k]),$$

and

$$\sum_{i=m+1}^{n} \hat{A}_i \cos(kT\hat{\omega}_i + \hat{\phi}_i) = 0.$$

For this condition, the optimal solution for Eq. (4.13) is,

$$\frac{1}{k}\sum_{l=1}^{k} (y[l] - \hat{C}x[l])^T (y[l] - \hat{C}x[l]) + \kappa n = \sigma^2 + \kappa m,$$

where σ^2 is the variance of the noise. This optimal result is reached when $n = m$. For any $n > m$,

$$\frac{1}{k}\sum_{l=1}^{k} (y[l] - \hat{C}x[l])^T (y[l] - \hat{C}x[l]) + \kappa n > \sigma^2 + \kappa m,$$

which contradicts with the minimization principle of the optimal SSBAT. Hence, to satisfy the optimization condition of Eq. (4.13). It is necessary that $n \leq m$. The proof is then completed. ∎

The Lemma 4.2.1 provides a condition for realizing the proposed SSBAT. In Theorem 4.2.1, the tracking performance and the parameter convergence of the proposed adaptive tracking model is shown for the case when $n = m$.

Theorem 4.2.1 *For a vibration signal composed of finite m sinusoids as Eq. (4.15), and the 2nth order SSBAT model in Eq. (4.4), when $n = m$, the estimated parameter $\hat{\beta}$ converges to the nominal β, i.e. $\lim_{k\to+\infty} E(\hat{\beta}[k]) = \beta$ and the tracking error satisfies that $\lim_{k\to+\infty} E(\hat{y}[k] - y_m[k]) = 0$.*

Proof. For the ith sinusoidal component in Eq. (4.15), there are two points in the spectrum at $-\omega_i$ and $+\omega_i$, where ω_i is the corresponding angular frequency. Therefore, the vibration

signal composed of m sinusoidal signals is able to contribute $2m$ points to the spectrum. Hence, according to [136] (Theorem 2.7.2), the signal is persistently exciting of order 2m.

Here, the convergence proof for the condition of $n = m$ is given. According to the definition of Persistent Excitation, there exist a constant $\alpha > 0$, such that,

$$P \geq \alpha I, \tag{4.17}$$

where I is an identity matrix. According to Eq. (4.14) and let $\tilde{\beta}[k] = E(\hat{\beta}[k] - \beta)$, then,

$$\tilde{\beta}[k] = \tilde{\beta}[k-1] - \gamma \frac{P_{k-1}x'[k]x'[k]^T\tilde{\beta}[k-1]}{1+\zeta x'[k]^T P_{k-1}x'[k]} = (I - \gamma \frac{P_{k-1}x'[k]x'[k]^T}{1+\zeta x'[k]^T P_{k-1}x'[k]})\tilde{\beta}[k-1], \tag{4.18}$$

$$P_k P_{k-1}^{-1} = (I - \gamma \frac{P_{k-1}x'[k]x'[k]^T}{1+\zeta x'[k]^T P_{k-1}x'[k]}). \tag{4.19}$$

Therefore,

$$P_k^{-1} E(\tilde{\beta}[k]) = P_{k-1}^{-1} E(\tilde{\beta}[k-1]), \tag{4.20}$$

as

$$P_k - P_{k-1} = -\gamma \frac{P_{k-1}x'[k]x'[k]^T P_{k-1}}{1+\zeta x'[k]^T P_{k-1}x'[k]} \leq 0, \tag{4.21}$$

$$P_k \geq \alpha I. \tag{4.22}$$

Since we focus on tracking the trend of the vibration signal, $x'[k]$ varies with time in general, and in most cases, $x'[k] \neq 0$. From the above, it is readily obtained that

$$\lim_{k \to +\infty} P_k = \bar{P}.$$

where $\bar{P} \geq \alpha I$ is a constant matrix. Therefore,

$$\lim_{k \to +\infty} P_k = \lim_{k \to +\infty} P_{k-1},$$

and based on Eq. (4.20), it is obtained that

$$\lim_{k \to +\infty} E(\hat{\beta}[k]) = \lim_{k \to +\infty} E(\hat{\beta}[k-1]).$$

To further prove the convergence, define $V_k = \tilde{\beta}[k]^T P_k^{-1} \tilde{\beta}[k]$. Then from Eq. (4.20), we have

$$\begin{aligned} V_k - V_{k-1} &= \tilde{\beta}[k]^T P_k^{-1}\tilde{\beta}[k] - \tilde{\beta}[k-1]^T P_{k-1}^{-1}\tilde{\beta}[k-1] = (\tilde{\beta}[k] - \tilde{\beta}[k-1])^T P_{k-1}^{-1}\tilde{\beta}[k-1] \\ &= -(\gamma \frac{P_{k-1}x'[k]x'[k]^T\tilde{\beta}[k-1]}{1+\zeta x'[k]^T P_{k-1}x'[k]})^T P_{k-1}^{-1}\tilde{\beta}[k-1] = -\gamma \frac{(\tilde{\beta}^T[k-1]x'[k])^2}{1+\zeta x'[k]^T P_{k-1}x'[k]}. \end{aligned} \tag{4.23}$$

Refer to Eq. (4.17) and the Persistent Excitation condition, we can derive

$$V_k - V_{k-1} < 0.$$

Hence,

$$\lim_{k\to+\infty} V_k = 0,$$

which means $\lim_{k\to+\infty} \tilde{\beta}[k] = 0$, i.e.

$$\lim_{k\to+\infty} E(\hat{\beta}[k]) = \beta.$$

As $E(\tilde{y}[k]) = \tilde{\beta}x'[k]$ and $x'[k]$ is bounded, it is readily obtained that

$$\lim_{k\to+\infty} E(\hat{y}[k] - y_m[k]) = 0.$$

Therefore, the tracking of the SSBAT is converge and the proof is complete. ■

Remark 4.2.1 *When $n < m$, it means that the proposed SSBAT model is used to synthesize the nominal signal with fewer number of sinusoidal components. To realize this, the amplitudes, frequencies and phases of sinusoidal components in the synthesis model will be adjusted to fit the original signal adaptively. The synthesized signal is time-variant in nature. The tracking error is bounded due to the fact that the SSBAT is stable (see Eg. (2) and the matrix A in Eq. (4.12)).*

4.2.4 SSBAT Based Fault Detection Approach

An SSBAT model based fault detection approach is proposed in this work for rotating machines. First of all, the established SSBAT algorithm is used as a linear predictor to obtain the one-step ahead signal. An on-line SSBAT residual can be calculated by subtracting the predicted signal from the measured data. Random prediction error may occur if the rotating machinery remains in a healthy condition. However, when a localized fault, e.g., a shaft crack or a rotor rubbing develops, we can express $y_m[k]$ as

$$y_m[k] = \begin{cases} (\lambda^T - C^T V)x[k] + v[k], & k < k_f \\ (\lambda^T - C^T V)x[k] + v[k] + d[k] & k \geq k_f \end{cases}.$$

In this case, a periodical significant deviation is expected from the model. This is because the SSBAT model can track the vibration signal trend with sinusoidal properties but will

not predict/track the abrupt impulse like fault (which has a very wide spectrum):

$$E(\tilde{y}[k]) = E(y_m[k] - \hat{y}[k]) = \begin{cases} \bar{\varepsilon} & k < k_f \\ \bar{\varepsilon} + d[k] & k \geq k_f \end{cases}.$$

where $\bar{\varepsilon}$ is the mean of the random noise.

Clearly, the frequency-time domain feature extraction capability of SSBAT is well-suited to the nature of vibration signals and poses important applications in the fields of rotating machinery fault detection. In practice, when processing data of a long time period, the Kurtosis of the SSBAT residual can be calculated as an indicator to further confirm whether the abnormal fault has occurred. The implementation of the algorithm is sketched here.

1. Estimate the SSBAT model parameters $\hat{\beta}$ according to Eq. (4.14);
2. Compute the estimated output $\hat{y}[k]$ based on Eq. (4.4) and Eq. (4.12) but using the estimated parameters $\hat{\beta}$;
3. Calculate the on-line SSBAT residual $\tilde{y}[k]$;
4. Calculate the Kurtosis of the SSBAT residual for fault detection.

4.3 Simulation Examples

4.3.1 Example 1: Signal Tracking

For validation, a simulated vibration signal is generated. The vibration signal is formed as 10 harmonic components at 60 Hz, 120 Hz, 180 Hz, 240 Hz, 300 Hz, 360 Hz, 420 Hz, 480 Hz, 540 Hz, 600 Hz, which have random amplitudes of 2.7, 2.0, 0.1, 0.2, 0.1, 0.07, 0.2, 0.3, 0.1 and 0.05 respectively and initial phases of 0.33π, 0.58π, 2.1π, 0.9π, 1.3π, 0.2π, 0.5π, 1.3π, 0.2π and 1.9π rad respectively. Additive white Gaussian noise with zero mean and standard deviation of 0.01 is included. During the simulation, 5000 samples have been generated with a sample time period of 1 second. The first 1000 simulated data samples are plotted in Fig. 4.1(a) and its corresponding spectrum calculating through Fast Fourier Transform (FFT) is shown in Fig. 4.1(b). The simulated vibration dataset was divided into two parts with evaluation set of 3000 samples and validation set of the rest 2000 samples. The tracking test has been carried out for one-component SSBAT, two-component SSBAT, three-component SSBAT and AR with minimum Akaike Information

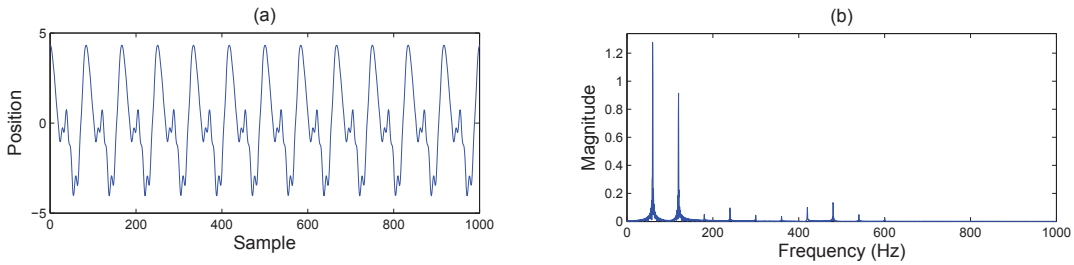

Figure 4.1: Simulated signal: (a) simulated vibration signal; (b) spectrum of the simulated signal.

Criterion (AIC) [137], denoted as SSBAT1, SSBAT2, SSBAT3 and AR AIC, respectively. By one-component, two-component, or in general n-component SSBAT model, we mean that the model in Eq. (10) corresponds to the sum of n sinusoids as given in Eq. (1) ($n = 1,\ 2,\ 3, ..$).

The AIC order of autoregressive method is computed from 1 to 150 with step 5. In this example, it is calculated to be 146. Tracking results for the validation set are compared in Fig. 4.2. Only first 200 samples out of the 2000 data are plotted to illustrate the convergence speed of different algorithms. However, the fit value is calculated based on the all 2000 validation data. The fit value is defined in % as the normalized root mean square (NRMSE) measure of the goodness of fit, which is calculated as:

$$FIT = 100\frac{1 - ||y - \hat{y}||_2}{||y - \bar{y}||_2},$$

where y is the validation data, $\bar{y}$ is the mean of the validation data and $\hat{y}$ is the estimated output. $||y||_2$ means the Euclidean Norm of y. Fig. 4.2(a), 4.2(b) and 4.2(c) shows the identification results of one-component, two-component and three-component SSBAT algorithm. Very fast convergence (within 50 iterations) and satisfactory fitting results (89.73%, 90.57% and 92.09% respectively) are demonstrated. Also, it shows that no significant improvement is made by increasing the sinusoidal component numbers, which indicates the capability of the SSBAT using a low order adaptive model to synthesize a high order sinusoidal comprised signal. Fig. 4.2(d) shows the performance of AR algorithm with the order of 146. It has also reached the fitting value of 85.84%. However, it needs at least 150 iterations to converge. Hence, the proposed SSBAT method has demonstrated fast and superior tracking performance compared with the AR method. Particularly, the SSBAT algorithm is qualified to apply in adaptive sinusoidal synthesis.

The computation time for signal tracking simulation in Fig. 4.2 of the SSBAT method is compared with that of the AR method. It is obtained based on using MATLAB on a local

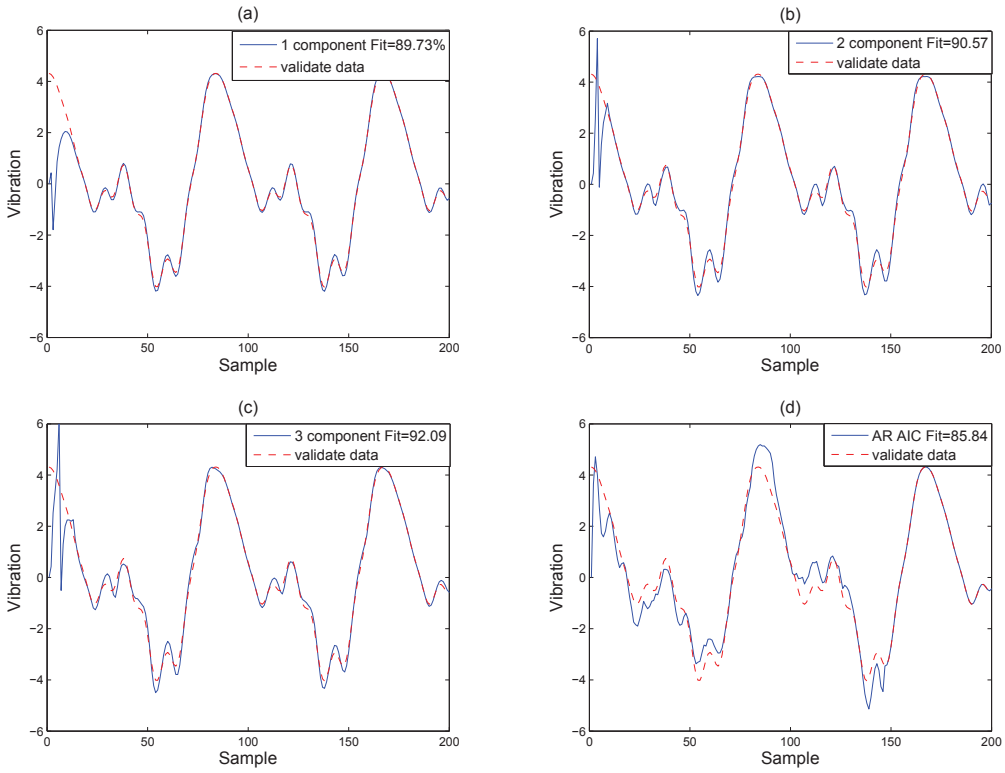

Figure 4.2: Signal tracking performance: (a) one-component SSBAT; (b) two-component SSBAT; (c)three-component SSBAT; (d) AR AIC.

workstation with Xeon(R) CPU at 2.4 GHz. As we can see, the computation of SSBAT is much more time efficient than the 146 order AR AIC method. The result is shown in Table 4.1.

The adaptive evolution of the estimated parameters for One-component SSBAT is demonstrated in Figure 4.3. It is clearly shown that the parameters evolve periodically to adapt the vibration signal when the order of the synthesis model is much lower than the actual number of sinusoidal components.

Table 4.1: Computation Time

Algorithm	SSBAT1	SSBAT2	SSBAT3	AR AIC
Time (Seconds)	0.216892	0.143940	0.150662	7.383978
Fit (%)	89.73	90.57	92.09	85.84

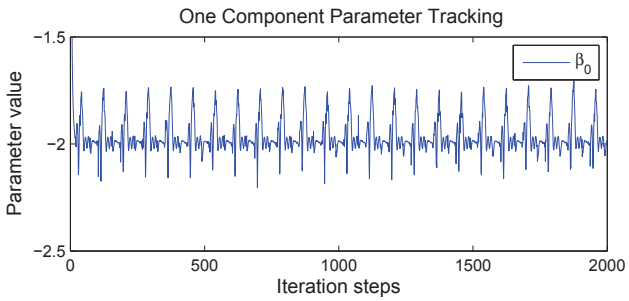

Figure 4.3: Adaptive parameter tracking

4.3.2 Example 2: Parameters Convergence

To demonstrate the convergence, we assume, $m = n$, and the vibration signal is exactly composed of three sinusoidal components with angular velocity

$$T\omega_1 = 0.8, T\omega_2 = 2.9, T\omega_3 = 1.5$$

Amplitudes and phases of the three components are randomly chosen which have no influence for parameter tracking. The nominal β can be calculated from Eq. (4.8):

$$D(z) = \prod_{i=1}^{3}(z^2 - 2z\cos(T\omega_i) + 1) = z^6 + 0.4070z^5 + 0.2165z^4 + 1.1969z^3 + 0.2165z^2 + 0.4070z + 1,$$

where $\beta = [\beta_0, \beta_1, \beta_2]^\top = [1.1969, 0.2165, 0.4070]^\top$.

If we use a SSBAT signal with three sinusoidal components to synthesize the nominal signal, then the values of $\hat{\beta}_i, (i = 0, 1, 2)$ are converged to the true values β_i as shown in Fig. 4.4. According to Eq. (4.8), β_i are directly corresponding to ω_i. Therefore, the frequencies of the SSBAT model $\hat{\omega}_i$ can track that of the nominal sinusoidal components ω_i when the number of sinusoidal components of the synthesis model is equal to the actual number of nominal sinusoidal components, i.e. $n = m$.

4.3.3 Example 3: Fault Detection

To demonstrate the application of the proposed SSBAT algorithm in fault detection, a decaying exponential enveloped sinusoidal impact is periodically added to the simulated signal in *Example 1* . The maximum amplitude of the impact is 2 and the time constant of the exponential envelop is 0.002. The modeled impact fault is added to the signal at a period of 83 milliseconds, which means the impact impulse occurs 12 times every second. This is commonly seen in gear tooth defect such as a tooth root crack or spall [85]. The

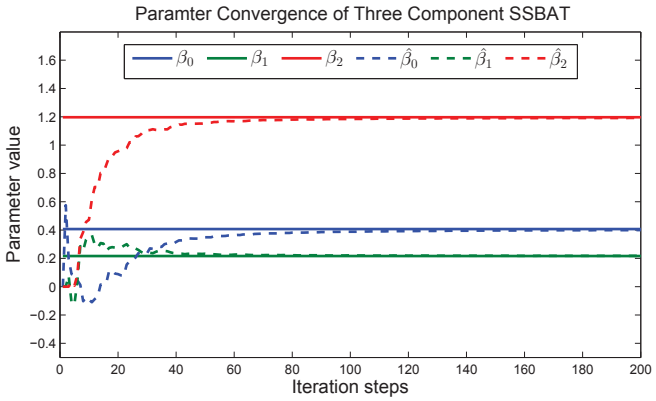

Figure 4.4: Parameter convergence

fault impact is shown in the top of Fig. 4.5(a). The vibration signal after adding exponential envelope impacts is shown in the bottom of Fig. 4.5(a) and its corresponding spectrum is illustrated in Fig. 4.5(b).

After constructing the fault signal, several methods including the one-component, two-component, three-component SSBAT based together with the AR AIC and ARMED methods are adopted to detect the fault. The prediction residual of the five methods are presented in Fig. 4.6. The time duration of the 2000 samples correspond to 0.4 seconds, which means that it has gone through 4.8 periods of the fault impacts.

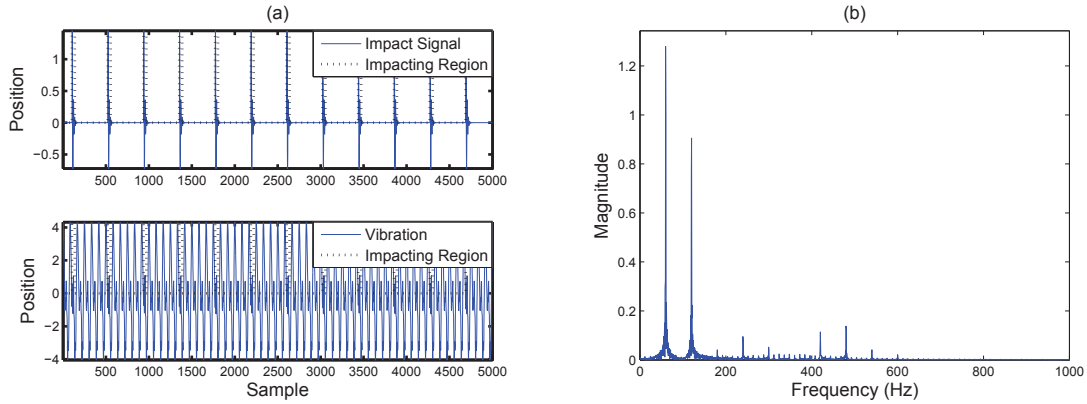

Figure 4.5: Signal with faults: (a) vibration signal with added exponential envelope impacts; (b) spectrum of the simulated signal with fault.

In Fig. 4.6, all four methods have detected four obvious faults. By comparing the results, all the three SSBAT algorithms can detect the faults and have achieved comparable performance as the ARMED method. However, it is clearly seen that the ARMED has filtered out much more signal information in the residual. Moreover, the SSBAT and ARMED

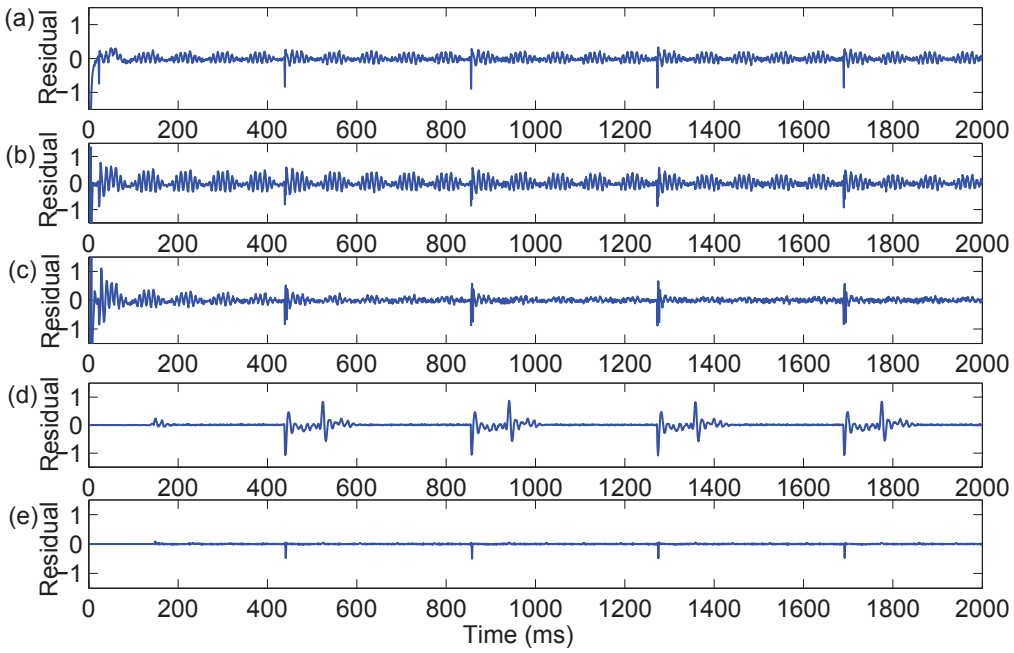

Figure 4.6: Fault detection results: (a) one-component SSBAT residual; (b) two-component SSBAT residual; (c) three-component SSBAT residual; (d) AR AIC residual; (e) ARMED residual.

give better results than that using the AR AIC method. This is because the AR AIC method has over fitted the fault information while the SSBAT does not. The SSBAT method retains the sinusoidal characteristics of the vibration signal during the adaptive tracking (or trending) but it will not adapt to the abrupt impulse like faults.

The Kurtosis values are analyzed to evaluate the SSBAT, AR AIC and ARMED methods' capability in detecting impact faults. Faults of various levels have been added to the simulated vibration signal. By comparing the fault peak disturbance versus the kurtosis in Fig. 4.7, it is noticed that the AR AIC and ARMED method have the same Kurtosis values. It can be seen that the SSBAT schemes tend to demonstrate better performance than AR methods with faults of higher amplitudes while both AR models perform better for faults with smaller amplitudes. It means that the SSBAT methods are not as sensitive as the two AR methods. However, proper tuning of the SSBAT model order can help improve this aspect. For example, among the SSBAT methods, the three-component SSBAT method has the best fault detection performance. Note that, when calculating the Kurtosis, the first

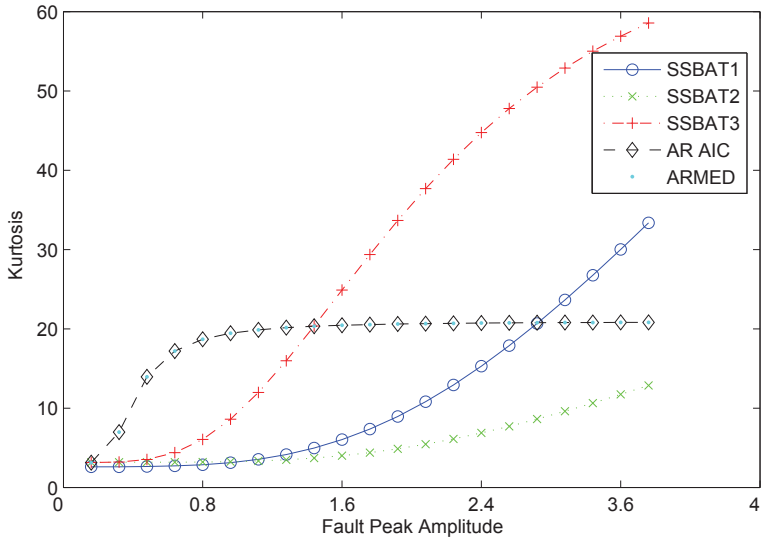

Figure 4.7: Kurtosis of different fault peak disturbance

200 samples of the residual signal are ignored to allow for the SSBAT and AR models to converge.

4.4 Application to Steam Turbine Fault Diagnosis

Vibration data acquired from a turbine generator is investigated in this section. The 50MW back pressure steam turbine generator consists of a steam turbine and a generator [138], Fig. 4.8.

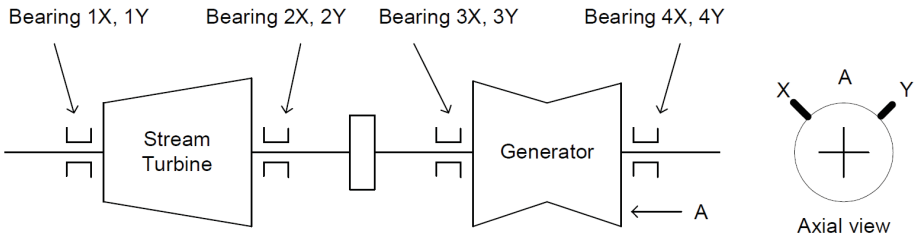

Figure 4.8: Layout of the back pressure steam turbine generator

Data is collected by two vibration sensors on bearing 4 installed along x and y axes. A data measurement set of 1226 samples is collected every two hours at a sampling rate of 9.7 kSamples/second. Under normal operation, the turbine is rotating at approximately 60Hz,

resulting in approximately 161 samples per revolution and nearly 8 rotor revolutions per dataset. The vibration sensors on each axis detect the decomposed vibration signal. Hence, the fault detection can be carried out in each direction and here we only analyze the $x-axis$ vibration signal. The datasets used in this case study were collected from August 10th, 2005 to January 15th, 2006, in which two machine downtimes were observed and recorded. A rotor-stator rubbing event caused by the shaft bending was verified by inspection and fixed during the second downtime. Therefore, we are expecting a repeating fault once per shaft revolution, which is consistent with a rotor-to-stator rubbing fault. Since there are nearly 8 revolutions in each data set recorded in this application, 7 or 8 impulsive fault signatures are expected. In the following analysis, it is assumed the fault is not known beforehand and completed fault detection procedure is conducted.

The condition of the turbine is analyzed with one component SSBAT, two component SSBAT, and three component SSBAT methods. Moreover, AR method with optimal order calculated with AIC and ARMED method are also adopted to compare with the SSBAT methods.

Firstly, the Root Mean Square (RMS) of the vibration signal is calculated for the turbine. It has been shown that the energy and root mean square of vibration signal will change when a bearing fault occurs [139]. The RMS of the vibration is calculated for the whole vibration data to give a general impression of the defects in the time domain, Fig. 4.9 (a).

It is suspected that there is a fault between the two machine downtimes, which is a month-long downtime after August 10th, 2005 and another short downtime on January 15th, 2006. There are two possibilities according to the RMS results. A maintenance may have been carried out during the first downtime and the physical model may deviate. Therefore, a small calibration may have been conducted during the second downtime on January 15th, 2006. The second possibility is that abnormal behavior was observed before August 10th, 2005 and a maintenance was carried out. However the problem was not corrected and the fault lasted for the following 4 months until the second maintenance was conducted on January 15th, 2006. The SSBAT method and the AR methods are adopted to the whole data sets and the corresponding Kurtosis of the residual is plotted in Fig. 4.9 (b-e). All the methods indicate high fault level during the time interval between the two downtimes. Therefore, we can confirm that there exists certain fault(s) during this period.

The suspected fault is identified during the specific time interval from September 22, 2005, to January 15th, 2006. We randomly select one data set during this time period to conduct a more detailed analysis. Fig. 4.10(a) shows the vibration of the data set at that time. Fig. 4.10 (b-f) shows the residual of the three SSBAT methods and the AR methods. All the methods generate residuals from which 7 repeating faults indicating the

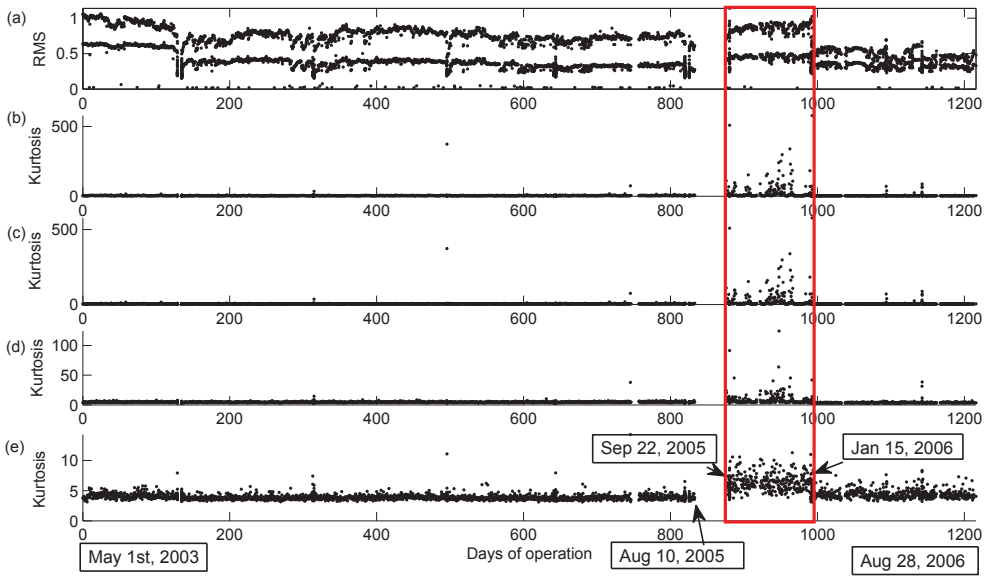

Figure 4.9: Kurtosis comparison for four methods: (a) RMS of the vibration; (b) Kurtosis of one-component SSBAT residual; (c) Kurtosis of two-component SSBAT residual; (d) Kurtosis of three-component SSBAT residual; (e) Kurtosis of AR AIC residual.

fault occurrence once per shaft revolution can be observed. From the figures, it can be seen that all the SSBAT methods perform satisfactorily detecting the fault while the two-component SSBAT has the best performance. The AR AIC method is also able to give some indication to the fault although there exist certain ambiguities. It is noticed that in this application, the ARMED method has shown better performance over other methods. The SSBAT methods have shown comparable performance as the ARMED method. It should be noted that the SSBAT method only utilizes the online data set to detect the fault while both the AR models need to use the history no-fault data sets to fit model.

Fig. 4.11 shows the location of the faults with respect to the rotor orbit. In Fig. 4.11(a) the X-axis vibration is plotted together with two-component SSBAT residual signal. Although there is no sign of fault on the Y-axis vibration according to the two-component SSBAT result (Fig. 4.11(b)), it is still able to identify the exact location on the rotor orbit. In Fig. 4.11(c) the vibration orbit is shown and the location of suspected fault can be identified. From the orbit, we can see some sign of abnormal vibration in the x direction at the fault location.

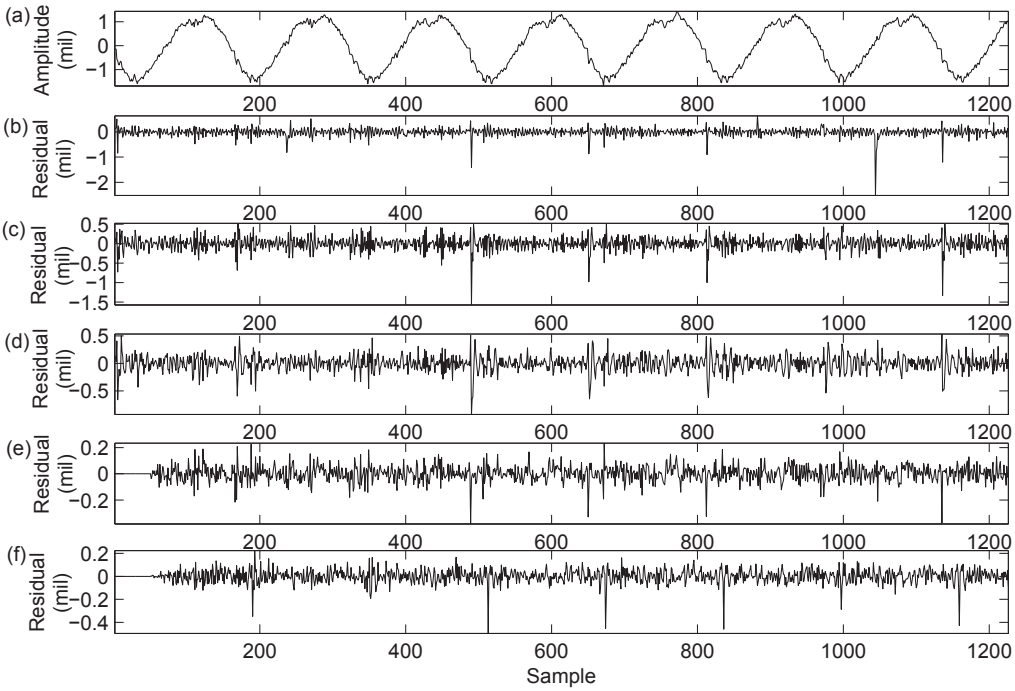

Figure 4.10: Fault detection results for turbine: (a) vibration signal; (b) one-component SSBAT residual; (c) two-component SSBAT residual; (d) three-component SSBAT residual; (e) AR AIC residual; (f) ARMED residual.

4.5 Conclusion

In this chapter, an SSBAT fault diagnosis method is proposed. The data-driven algorithm is based on the specific features of the vibration data from rotating machinery. This adaptive model is constructed based on the sinusoidal structure of the vibration signals. It is well suited to the nonlinear nature of the sinusoidal model analysis. Moreover, it transforms the problem into a linear adaptive problem based on the time-frequency characteristics of sinusoids. Three simulation examples were performed to illustrate the SSBAT tracking, parameter convergence, and fault detection performance, respectively. In addition, a practical application to a steam turbine fault detection is also presented. For performance evaluation, the standard AR AIC predictive model and ARMED algorithm are compared with the SSBAT models in both simulation examples and the application example. The experimental data indicated that the SSBAT method is better than the AR algorithm and has achieved comparable performance as the ARMED method.

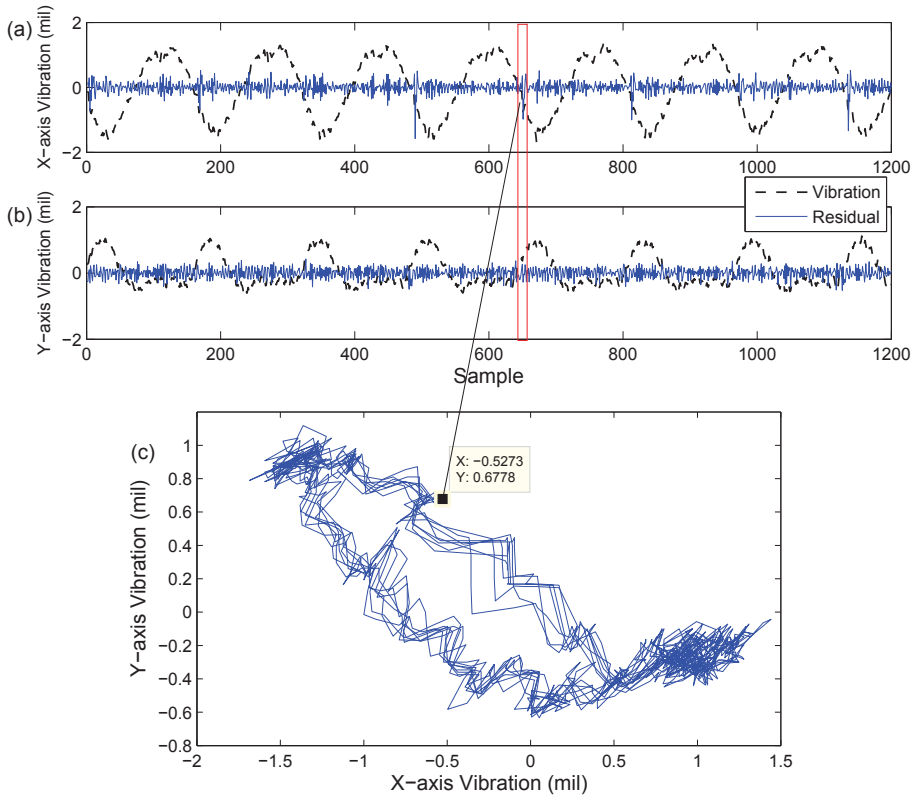

Figure 4.11: The position of faults in orbit map: (a) X-axis vibration overlayed with two-component SSBAT residual; (b) Y-axis vibration overlayed with two-component SSBAT residual; (c) fault on orbit.

Chapter 5

Minimum Entropy Deconvolution Optimized Sinusoidal Synthesis and Its Application to Vibration Based Fault Detection *

5.1 Introduction

A sinusoidal synthesis based fault detection method was proposed in Chapter 4 and it was successfully adopted for steam turbine fault detection [94]. The frequency information of the vibration signal can be fully used in developing the sinusoidal synthesis data-driven model. However, it is insensitive to phase properties, which can differentiate noise from characteristic impulsive fault signatures.

Kalman filtering is an effective means of estimating the time-varying coefficients and is widely applied in speech parameter estimation problems [140, 141]. Recently, the theory of adaptive filtering and estimation has also been applied to estimate frequencies and amplitudes of sinusoidal signals [126, 127, 128, 142]. Minimum Entropy Deconvolution (MED), originally proposed by Wiggins for applications on seismic recordings [143], was adopted for gear fault detection together with the AR method by H. Endo et. al. [85]. It was shown that the ARMED resulted in improved performance over the traditional AR

*Parts of the results in this chapter appeared in *Journal of Sound and Vibration*, vol. 390, pp. 218-231, 2017.

method. The MED algorithm can make use of higher-order statistical characteristics, in particular, the kurtosis, of the signal. Kurtosis is defined as the fourth moment of the distribution and measures the relative peakedness or flatness of a distribution as compared to a normal distribution. Kurtosis provides a measure of the size of the tails of a distribution and is used as an indicator of major peaks in a set of data. Kurtosis has been used for diagnosing bearing, and gearbox faults [144]. Recently, a new Maximum Correlated Kurtosis Deconvolution method was proposed and shown to be effective in detecting periodic fault signatures [132]. However, it requires a priori knowledge of the fault period, and for non-integer fault periods, it requires an additional resampling preprocessing stage [145].

Based on the existing work [85, 94, 132], this chapter outlines a MED based sinusoidal synthesis (MEDSS) data-driven model designed for fault diagnosis in rotating machinery [95]. First, the sinusoidal synthesis model proposed in Chapter 4 is adopted. In the process of building the SS model, the MED technique is applied to optimize the model parameters. The MED algorithm is more sensitive to the phase relationship (which differentiates white noises from impulses) by using higher-order statistical properties compared to the autocorrelation measurements like AR [85]. Thus it is effective in deconvolving the impulsive sources from a mixture of signals. Therefore, the MEDSS model is insensitive to the strong background noises encompassing other vibration sources and is more sensitive to characteristic fault with impulsive signatures. Finally, a time-weighted-error Kalman filter is designed for estimating the parameters of the MEDSS model adaptively. This makes it possible to synthesize the vibration signal with a low order but time-varying MEDSS model. The advantages of low computation complexity and adaptive form from linear predictors are retained in this method. The scheme proposed in this chapter is mainly used for detection of defects in rotating elements that have sharp leading and trailing defect edges, which typically generate strong impulsive signatures.

The remainder of this chapter is organized as follows: The MEDSS model is designed and its application in fault diagnosis is proposed in Section 5.2 as the main results. In Section 5.3, three simulation examples are provided to illustrate the fault detection performance for fault-free, high signal-to-noise ratio (SNR) faulty and low SNR faulty conditions. A practical application example for rubbing fault detection in an industrial steam turbine is given in Section 5.4, followed by a conclusion in Section 5.5.

5.2 The MEDSS Model and Its Application to Fault Detection

The measured vibration signal with periodic characteristic impulsive fault signatures can be represented as Eq. (5.1).

$$y_m[k] = y_o[k] + d[k] + v[k], \tag{5.1}$$

where the meaning of the symbols are the same to Chapter 4, Eq. (4.1).

5.2.1 Regular Sinusoidal Synthesis (SS) Model

The regular SS model proposed in Chapter 4, Eq. (4.4) is used to predict the deterministic pattern of the fault free vibration signal, $y_o[k]$. Chapter 4, Eq. (4.6) then can be represented in the filter form as follows [94]:

$$\begin{aligned} Y(z) &= \frac{(\lambda_{2m-1}-\beta_{m-1})z^{2m-1}+\cdots+(\lambda_m-\beta_0)z^m+(\lambda_{m-1}-\beta_1)z^{m-1}+\cdots+(\lambda_0-1)}{\Lambda(z)}Y_o(z) \\ &= G(z)Y_o(z), \end{aligned} \tag{5.2}$$

where $Y(z)$ is the filtered vibration signal, $Y_o(z)$ is the nominal fault-free vibration signal, and $G(z)$ denotes the SS filter.

From Eq.(5.2), the transfer function $G(z)$ is stable, and can be treated as an SS filter. Therefore, Eq.(5.2) denotes the process of data prediction, which can be presented in the time domain as follows:

$$y[k] = g[k] * y_o[k] = \sum_{i=0}^{m} g[i]y_o[k-i], \tag{5.3}$$

where g represents the characteristic response of the filter $G(z)$ and it is assumed that $g[0] = 0$ for a one-step ahead predictor. As the nominal vibration signal $y_o[k]$ is unknown, the measured signal $y_m[k]$ can be used to pass through the SS filter.

5.2.2 MED Optimization

In section 5.2.1, the sinusoidal synthesis filter is reviewed, which incorporates specifically the frequency characteristics of the sinusoidal signal. In this section, the MED technique is applied to extract the phase information and further optimize the SS filter g. According to Chapter 4, Eq.(4.10), the filter g is arbitrarily selected as long as Λ is a stable

polynomial [134]. The nominal vibration signal $y_o[k]$ is not available, but instead, the measured signal $y_m[k]$ is available, which contains noises and impact fault signals as shown in Eq.(5.1). When the faults are in their early stages, the characteristic impulsive fault signature $d[k]$ is relatively small compared to the noise $v[k]$ and its presence can be masked by the noise. Moreover, both the noise and the fault signature $d[k]$ are in nature broadband excitation signals, and their magnitude spectra are not easily differentiable. The most significant difference is contained in the phase information of the signal. Hence, in this section, the MED approach is designed to further highlight the distinctive characteristics of the impulse-like fault signatures so that they can be detected from the noisy measurement signals. Meanwhile, such a filter can minimize or even eliminate noises encompassing other vibration sources for the machine under inspection. The enhanced MEDSS filter can be denoted as follows:

$$g_e = g * f, \tag{5.4}$$

where f is the corresponding MED filter whose coefficient vector $\mathbf{F} = [f_0, f_1, \cdots, f_L]^T$ and L is the order of the filter. The MED filter is used to optimize the original SS filter g. In the MEDSS filter, the entropy of the measured signal $y_m[k]$ is minimized, which means the effect of random noises is minimized and the structured information of the impulsive fault signatures is enhanced. A comparison of noises with the impulsive fault signatures shows their magnitude response is similar (as broadband excitations), but impulses have much more distinctive phase responses than random noises. Such structured information will be highlighted by minimum entropy deconvolution algorithms. On the other hand, the high entropy noises will be removed [85].

Next we will present a state space representation for the MEDSS by combining both the sinusoidal synthesis model and the MED filter. The sinusoidal synthesis model of Eq.(5.3) becomes the following:

$$y = g_e * y_o \approx g_e * y_m = g * f * y_m. \tag{5.5}$$

Here, $y_m[k]$ can be used instead of $y_o[k]$ because the noise effect is to be minimized by the MED filter.

The MED filter f is iteratively calculated based on the measured vibration signal. Assume $s = f * y_m$, where $\mathbf{S} = [s[1], s[2], \cdots, s[N]]^T$ and N is the total number of samples. The MED filter f can be designed by maximizing the kurtosis of the measured vibration signal. Kurtosis is defined as the fourth moment of the distribution and is used to measure how outlier-prone a signal is. Due to the impulse-like rotating fault manifestation, kurtosis is suitable to be a fault indicator in rotating machinery. The MED filter f is designed by

maximizing the kurtosis of the filtered signal through Eq. (5.6) [144]:

$$\max_f \text{Kurtosis} = \max_f K(f) = \max_f \frac{\sum_{j=1}^{N}(s[j]-\mu_s)^4}{\left(\sum_{j=1}^{N}(s[j]-\mu_s)^2\right)^2}. \tag{5.6}$$

Assuming $s[n]$ is zero-mean, i.e. $\mu_s = 0$, then Eq. (5.6) becomes as follows:

$$\max_f K(f) = \max_f \frac{\sum_{j=1}^{N} s^4[j]}{\left(\sum_{j=1}^{N} s^2[j]\right)^2}. \tag{5.7}$$

The filter coefficients $f_l, (l = 0,1,\ldots,L)$ corresponding to the maximum Kurtosis can be calculated by setting the derivatives of $K(f)$ in Eq.(5.7) with respect to f_l to be zero. We then have the following:

$$\frac{d}{df_l}K(f) = 0, \qquad l = 0,1,\ldots,L. \tag{5.8}$$

As we have

$$\frac{\partial s[j]}{\partial f_l} = \frac{\partial(\sum_{p=0}^{L} f_p y_m[j-p])}{\partial f_l} = y_m[j-l] \tag{5.9}$$

and

$$\frac{\partial K(f)}{\partial s[j]} = \frac{4s^3[j]\sum_{j=1}^{N} s^2[j] - 4s[j]\sum_{j=1}^{N} s^4[j]}{(\sum_{j=1}^{N} s^2[j])^3}. \tag{5.10}$$

Substituting Eq. (5.7), Eq. (5.9) and Eq. (5.10) into Eq. (5.8), we have Eq.(5.11) as follows:

$$\sum_{j=1}^{N}\frac{\partial K(f)}{\partial s[j]}\frac{\partial s[j]}{\partial f_l} = \sum_{j=1}^{N}\left\{\frac{4s^3[j]\sum_{j=1}^{N} s^2[j] - 4s[j]\sum_{j=1}^{N} s^4[j]}{(\sum_{j=1}^{N} s^2[j])^3} y_m[j-l]\right\} = 0, \qquad l = 0,1,\ldots,L. \tag{5.11}$$

Rearrange Eq.(5.11) and we can obtain the following Eq. (5.12):

$$\frac{\sum_{j=1}^{N} s^2[j]}{\sum_{j=1}^{N} s^4[j]}\sum_{j=1}^{N} s^3[j]y_m[j-l] = \sum_{j=1}^{N}(s[j]y_m[j-l]), \qquad l = 0,1,\ldots,L. \tag{5.12}$$

As

$$s[j] = \sum_{p=0}^{L} f_p y_m[j-p], \tag{5.13}$$

Eq.(5.12) becomes the following:

$$\frac{\sum_{j=1}^{N} s^2[j]}{\sum_{j=1}^{N} s^4[j]}\sum_{j=1}^{N} s^3[j]y_m[j-l] = \sum_{j=1}^{N}(\sum_{p=0}^{L} f_p y_m[j-p]y_m[j-l]), \qquad l = 0,1,\ldots,L. \tag{5.14}$$

Then the MED filter coefficients can be calculated in the matrix form as follows:

$$\mathbf{F} = \frac{\sum_{j=1}^{N} s^2[j]}{\sum_{j=1}^{N} s^4[j]} \left(\mathbf{\Gamma}\mathbf{\Gamma}^T\right)^{-1} \mathbf{\Gamma} \left[s^3[1]\ s^3[2]\ \ldots\ s^3[N]\right]^T \tag{5.15}$$

$$\mathbf{\Gamma} = \begin{bmatrix} y_m[1] & y_m[2] & y_m[3] & \ldots & y_m[N] \\ 0 & y_m[1] & y_m[2] & \ldots & y_m[N-1] \\ 0 & 0 & y_m[1] & \ldots & y_m[N-2] \\ \vdots & \vdots & \vdots & \ddots & \vdots \\ 0 & 0 & 0 & \ldots & y_m[N-L] \end{bmatrix}_{(L+1)\times N}$$

where $\mathbf{F}$ is iteratively calculated.

The MED filter can be denoted in the transfer function form as the following:

$$F(z) = \sum_{l=0}^{L} f_l z^{-l} = \frac{f_0 z^L + f_1 z^{L-1} + \cdots + f_L}{z^L}. \tag{5.16}$$

The MEDSS filtered signal then becomes:

$$Y(z) = G(z)F(z)Y_m(z), \tag{5.17}$$

where $Y_m(z)$ is the z-transform of $y_m[k]$.

According to Eq.(5.17), the MEDSS model is established as a $(2m+L)$th order state space model Σ_1:

$$\Sigma_1 : \begin{cases} \mathbf{x}[k+1] = \mathbf{A}\mathbf{x}[k] + \mathbf{B}y_m[k] \\ y[k] = \mathbf{C}\mathbf{x}[k] \end{cases}, \tag{5.18}$$

where

$$\mathbf{A} = \begin{bmatrix} -\lambda_{2m-1} & -\lambda_{2m-2} & \cdots & -\lambda_0 & 0 & \ldots & 0 & 0 \\ 1 & 0 & \cdots & 0 & 0 & \ldots & 0 & 0 \\ 0 & 1 & \cdots & 0 & 0 & \ldots & 0 & 0 \\ \vdots & \vdots & \ddots & \vdots & \vdots & \ddots & \vdots & \vdots \\ 0 & 0 & \cdots & 0 & 0 & \ldots & 1 & 0 \end{bmatrix}_{(2m+L)\times(2m+L)}, \quad \mathbf{B} = \begin{bmatrix} 1 \\ 0 \\ \vdots \\ 0 \end{bmatrix}_{(2m+L)\times 1},$$

$$\mathbf{\Lambda} = \begin{bmatrix} \lambda_{2m-1} \\ \lambda_{2m-2} \\ \cdots \\ \lambda_1 \\ \lambda_0 - 1 \end{bmatrix}_{2m\times 1}, \boldsymbol{\beta} = \begin{bmatrix} \beta_{m-1} \\ \beta_{m-2} \\ \cdots \\ \beta_0 \end{bmatrix}_{m\times 1}, \mathbf{V} = \begin{bmatrix} 1 & 0 & \cdots & 0 & \cdots & 0 & 1 & 0 \\ 0 & 1 & \cdots & 0 & \cdots & 1 & 0 & 0 \\ \vdots & \vdots & \ddots & \vdots & \iddots & \vdots & \vdots & \vdots \\ 0 & \cdots & 0 & 1 & 0 & \cdots & 0 & 0 \end{bmatrix}_{m\times 2m},$$

$$\boldsymbol{\Psi} = \begin{bmatrix} f_0 & f_1 & \cdots & f_{2m-1} & f_{2m} & \cdots & f_L & 0 & \cdots & 0 \\ 0 & f_0 & \cdots & f_{2m-2} & f_{2m-1} & \cdots & f_{L-1} & f_L & \cdots & 0 \\ \vdots & \vdots & \ddots & \vdots & \vdots & \ddots & \vdots & \vdots & \ddots & \vdots \\ 0 & 0 & \cdots & f_0 & f_1 & \cdots & f_{L-2m+1} & f_{L-2m+2} & \cdots & f_L \end{bmatrix}_{2m\times(2m+L)},$$

$$\mathbf{C} = \boldsymbol{\Lambda}^\top \boldsymbol{\Psi} - \boldsymbol{\beta}^\top \mathbf{V}\boldsymbol{\Psi}. \tag{5.19}$$

The structures and coefficients of $\mathbf{A}$, $\mathbf{B}$, and $\boldsymbol{\Lambda}$ are all known if m, the number of sinusoidal components in the signal, is known. $\boldsymbol{\Psi}$ can be obtained based on the measured vibration signal. $\boldsymbol{\beta}$ is the unknown parameter vector. However, m, the number of harmonic components, is usually unknown in practice. In this case, a model order of $2n+L(n \leq m)$ is used to synthesize the vibration signal. The reason is that, in the SS filter, a lower order model can be used to synthesize a finite number of harmonic components of the vibration signal when the number of components is unknown [94].

Although the actual order of the MEDSS model is $2n+L$, the number of unknown parameters in $\boldsymbol{\beta}$ is still n, which is the same as in the regular SS model. Therefore, in the simulation study, for comparison with the regular SS, the $(2n+L)$th order MEDSS filter model is still named the $2n$th order MEDSS filter.

5.2.3 Adaptive Parameter Estimation Using Kalman Filter

The output matrix $\mathbf{C}$ in (5.18) is unknown and depends on $\boldsymbol{\beta}$, which is determined by the spectral distribution of the vibration signal. The MEDSS model in Σ_1 then can be transformed to Σ_2 based on $\boldsymbol{\beta}$:

$$\Sigma_2 : \begin{cases} \mathbf{x}[k+1] = \mathbf{A}\mathbf{x}[k] + \mathbf{B}y_m[k] \\ y'[k] = \boldsymbol{\beta}^\top[k]\mathbf{x}'[k] + v[k] \end{cases}, \tag{5.20}$$

where $y'[k] = \boldsymbol{\Lambda}^\top\boldsymbol{\Psi}\mathbf{x}[k] - y_m[k]$ and $\mathbf{x}'[k] = \mathbf{V}\boldsymbol{\Psi}\mathbf{x}[k]$. Here, the noise $v[k]$ is added because the measured vibration signal $y_m[k]$ is used in $y'[k]$ instead of $y[k]$.

In the MEDSS model, the unknown parameter vector $\boldsymbol{\beta}$ can be estimated based on the measured vibration signal. The parameter estimation is constructed in a Kalman filter framework, as given in Σ_3:

$$\Sigma_3 : \begin{cases} \boldsymbol{\beta}[k+1] = \boldsymbol{\Phi}[k,k-1]\boldsymbol{\beta}[k] \\ y'[k] = \mathbf{x}'[k]^T\boldsymbol{\beta}[k] + v[k] \end{cases}, \tag{5.21}$$

where $\mathbf{\Phi}[k,k-1]$ is the unknown time varying parameter transition matrix. The parameters of $\boldsymbol{\beta}[k]$ in Σ_3 are obtained in the following Eq. (5.22) [146]:

$$\begin{cases} \hat{\boldsymbol{\beta}}[k|k-1] = \mathbf{\Phi}[k|k-1]\hat{\boldsymbol{\beta}}[k-1|k-1] \\ \mathbf{V}_\beta[k|k-1] = \mathbf{\Phi}[k|k-1]\mathbf{V}_\beta[k-1|k-1]\mathbf{\Phi}^T[k|k-1] \\ \mathbf{K}_\beta[k] = \mathbf{V}_\beta[k|k-1]x'[k-1](x'^T[k-1]\mathbf{V}_\beta[k|k-1]x'[k-1]+\mathbf{R})^{-1} \\ \hat{\boldsymbol{\beta}}[k|k] = \hat{\boldsymbol{\beta}}[k|k-1]+\mathbf{K}_\beta[k](y'[k]-x'^\top[k-1]\hat{\boldsymbol{\beta}}[k|k-1]) \\ \mathbf{V}_\beta[k|k] = \mathbf{V}_\beta[k|k-1]-\mathbf{K}_\beta[k]x'^\top[k-1]\mathbf{V}_\beta[k|k-1] \end{cases}, \tag{5.22}$$

where $\mathbf{R}$ is the covariance of the measurement noise. $\mathbf{V}_\beta$ is the error covariance and $\mathbf{K}_\beta[k]$ is the Kalman gain. $\mathbf{\Phi}[k|k-1]$ is assumed to be the identity matrix during the iteration.

As mentioned above, when the exact number of sinusoidal components m is unknown, a lower model order n is usually chosen (i.e. $n \leq m$). The synthesized signal, in this case, has non-stationary frequency characteristics, which means the parameter vector $\boldsymbol{\beta}[k]$ is time varying. The classic Kalman filter algorithm in Eq.(5.22) may not be suitable for this parameter estimation problem (where the parameters are periodically time-varying), since it has an 'infinite memory' [140], meaning that the current estimated parameter is affected by the entire history of the signal. In this chapter, the time-weighted-error Kalman filtering technique is adopted. This method was proposed in [147] and was adopted for parameter estimation in many applications, e.g. the speech parameter estimation problem, [140]. The cost function of the time-weighted-error Kalman filter is given as follows[140]:

$$J_k = \sum_{j=1}^{k} \rho^{k-j}(y'[j]-\mathbf{x}'[j]^T\boldsymbol{\beta}[j])^2, \tag{5.23}$$

where ρ is the forgetting factor and $0 < \rho \leq 1$. In (5.23), the recent data has heavier weight than the previous data. Hence, the tracking of time-varying parameters can be realized. The smaller ρ is, the smaller windows of data will affect the estimation of parameters. The iteration of error covariance $\mathbf{V}_\beta[k]$ in Eq. (5.22) then becomes as follows:

$$\begin{cases} \mathbf{V}_\beta[k|k-1] = \rho^{-1}\mathbf{\Phi}[k|k-1]\mathbf{V}_\beta[k-1|k-1]\mathbf{\Phi}^T[k|k-1] \\ \mathbf{V}_\beta[k|k] = \mathbf{V}_\beta[k|k-1]-\mathbf{K}_\beta[k]x'^\top[k-1]\mathbf{V}_\beta[k|k-1] \end{cases}. \tag{5.24}$$

Once we have obtained the estimated parameter $\hat{\boldsymbol{\beta}}$, we can calculate the system matrix $\hat{\mathbf{C}}$ and further predict the one-step ahead signal. The estimated system matrix $\hat{\mathbf{C}}$ is calculated according to Eq.(5.19):

$$\hat{\mathbf{C}} = \mathbf{\Lambda}^\top\mathbf{\Psi} - \hat{\boldsymbol{\beta}}^\top\mathbf{V}\mathbf{\Psi}. \tag{5.25}$$

The linear predictor filter is then established as:

$$\Sigma_4 : \begin{cases} \mathbf{x}[k+1] = \mathbf{A}\mathbf{x}[k] + \mathbf{B}y_m[k] \\ \hat{y}[k] = \hat{\mathbf{C}}\mathbf{x}[k] \end{cases}, \tag{5.26}$$

where $\mathbf{x}[k] \in \mathbb{R}^{2n+L}$, $\mathbf{A} \in \mathbb{R}^{(2n+L)\times(2n+L)}$, $\mathbf{B} \in \mathbb{R}^{(2n+L)\times 1}$, $\hat{\mathbf{C}} \in \mathbb{R}^{(2n+L)\times 1}$, and they are in the same form as in Eq. (5.19).

5.2.4 Fault Detection Based on MEDSS filter

The MEDSS filter based fault detection for characteristic impulsive fault signatures of rotating machinery is proposed in this section. The established SS filter is used as a linear predictor to obtain the one-step ahead nominal signal. An on-line residual can be calculated by subtracting the predicted signal from the measured data. This residual (or unpredictable part of the signal) contains noises and impulse, which has a white spectrum and is called 'pre-whitened' [148]. To minimize the effect of the colored noise and enhance the fault information in the residual signal, corresponding to the MED process in the predictor, the measured signal $y_m[k]$ is replaced with the MED filtered signal $s[k]$. Random prediction error may occur if the rotating machinery remains in a healthy condition. However, when a localized fault, e.g., a shaft crack or a rotor rubbing develops, a periodical significant deviation is expected from the model. This is because the linear predictor model can track the vibration signal trend with sinusoidal properties, but will not predict/track the abrupt impulse like fault (which has a very wide spectrum):

$$\tilde{y}[k] = s[k] - \hat{y}[k] = \begin{cases} v_f[k] & k < k_f \\ v_f[k] + d[k] & k \geq k_f \end{cases}, \tag{5.27}$$

where k_f denotes the time when the fault happen. $v_f[k]$ is the MED-filtered noise, which is approximately a small noise with zero means and much smaller variance than the original noise $v[k]$ and $d(k)$ represents the periodic impulsive fault signature. The implementation of the algorithm is sketched here.

1. Construct the MEDSS model Σ_1, where the model order is assumed to be $2n$;
2. Estimate the sinusoidal frequency parameter vector $\hat{\boldsymbol{\beta}}$ using the time-weighted-error Kalman filter based on (5.22) and (5.24);
3. Calculate the system matrix $\hat{\mathbf{C}}$ according to (5.25);

4. Predict the one-step ahead signal based on the MEDSS predictor model Σ_4;

5. Calculate the residual according to (5.27) and conduct fault detection by residual evaluation.

5.3 Simulation

For validation, a simulated vibration signal is generated based on Eq. (5.28).

$$y_m[k] = \sum_{i=1}^{m} A_i \cos(kT\omega_i + \phi_i) + v[k], \tag{5.28}$$

where $m = 10$, meaning 10 harmonic components. The amplitudes of A_i are randomly picked as 0.5 mil, 0.1 mil, 0.1 mil, 0.2 mil, 0.1 mil, 0.07 mil, 0.2 mil, 0.3 mil, 0.1 mil and 0.05 mil. $\omega_i, (i = 1, 2, .., 10)$ are 60 Hz, 120 Hz, ..., 600 Hz, respectively. The initial phases of ϕ_i are randomly selected as 0.33π, 0.58π, 2.1π, 0.9π, 1.3π, 0.2π, 0.5π, 1.3π, 0.2π and 1.9π rad, respectively. v is a white noise, $v \sim \mathcal{N}(0, 4 \times 10^{-4})$. The sampling time T is 0.0002 s, which means that 5000 samples have been generated in one second.

5.3.1 Example 1: Analysis of the fault-free signal

The MED technique has a feature of enhancing the impulsive fault signatures. Therefore, it is meaningful to check if the MEDSS filter will lead to increased false alarms. In this example, a fault-free signal is analyzed. The simulated signal is plotted in Figure 5.1 (a) while the residual signals from three different methods are shown in Figure 5.1 (b-d). The three methods are the proposed MEDSS filter, the regular SS filter, and the ARMED method proposed in [85]. For both of the MEDSS and the regular SS models, the order $2n = 4$ is chosen. From Figure 5.1, we can see that all three methods perform well with no false alarms under the fault-free condition. As we can see from Figure 5.1 (b) and Figure 5.1 (d), there is a peak at around sample number 240. It should be noted that the peak does not indicate the presence of a fault and is an artefact of the MED technique. The definition of MED assumes zero data $x_n = 0$, for $n < 1$. This assumption creates a discontinuity between all the zero samples and the actual first sample x_1. This discontinuity causes a spurious impulse to be convolved at the beginning of the prediction [145]. However, the false alarm disappears after the algorithms converge and has no significant effect on detection of the periodic impulsive fault signatures proposed in this work.

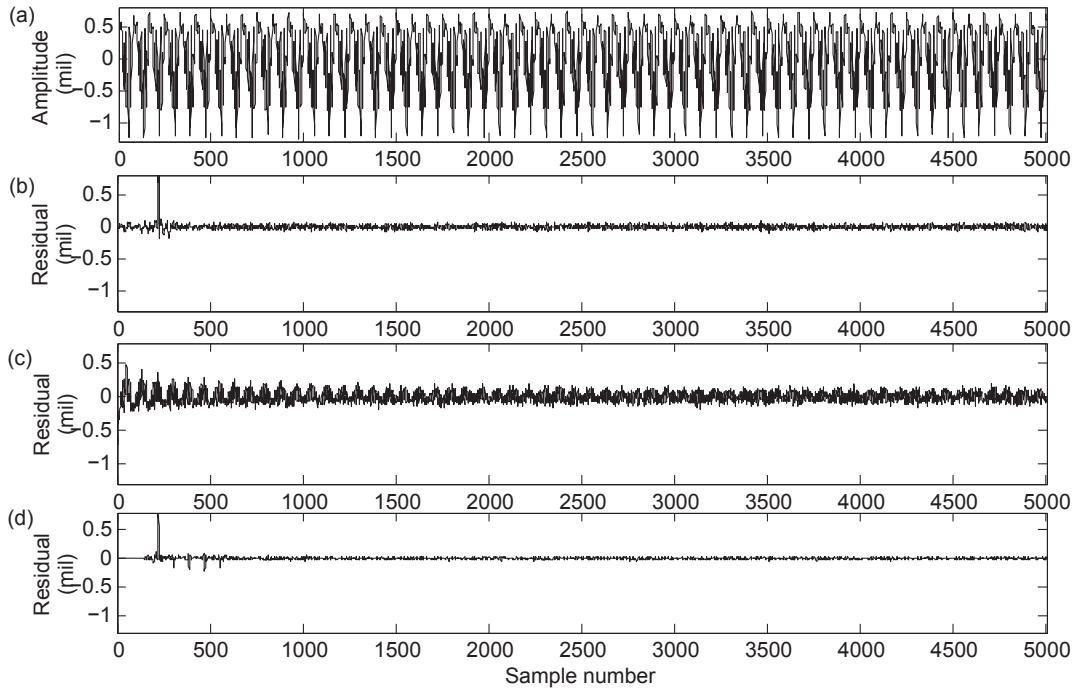

Figure 5.1: Comparison of fault detection performance with fault-free signal: (a) simulated signal with no fault, (b) residual of the $4th$ order MEDSS predictor, (c) residual of the $4th$ order regular SS predictor, (d) residual of the ARMED predictor.

The computation time of the three methods in Figure 5.1 is provided and shown in Table 5.1 for comparison purposes. It is obtained by using MATLAB on a local workstation with Xeon(R) CPU at 2.4GHz. As we can see, the regular SS method is the most time efficient. The computation time of MEDSS is about 10 times that of the regular SS and $1/10$ that of the ARMED. In addition, the corresponding kurtosis values of the residuals are shown in Table 5.1, from which we can see that only the ARMED residual has a relatively higher kurtosis value, while the other two methods render low kurtosis values close to that of the raw (fault-free) signal. As kurtosis is an indicator that reflects the "peakness" property of a signal, the relative high ARMED kurtosis value shows a potential possibility of false indication of the fault in the fault-free signal.

Table 5.1: Computation time and Kurtosis of Example 1

	Raw signal	MEDSS	Regular SS	ARMED
Time(seconds)	-	1.3861	0.1227	12.2267
Kurtosis	2.4492	2.9139	2.9234	16.9545

5.3.2 Example 2: Detection of impulsive fault signatures (high SNR)

To illustrate the performance of the proposed algorithm in detecting characteristic impulsive fault signatures, a decaying exponential enveloped sinusoidal impact is simulated and periodically added to the original fault-free signal. The periodic impact is formulated as Eq. (5.29):

$$d[k] = \sum_{j=0}^{\infty} d_{\text{amp}} \cdot \sin[(kT - jT_d - k_oT)\omega_s] \cdot \mathrm{e}^{-\frac{kT-jT_d-k_oT}{t_c}} \cdot H[kT - jT_d - k_oT], \qquad (5.29)$$

where $H[n]$ is the Heaviside step function [134]:

$$H[n] = \begin{cases} 1, & n \geq 0 \\ 0, & n < 0 \end{cases}, \qquad (5.30)$$

and the maximum amplitude of the impact d_{amp} is 2 mil. Each single impact is modulated to a sinusoidal form and decays exponentially. $\omega_s = 720\pi$ is the angular frequency of the sinusoidal modulation function. $t_c = 0.002$s is the time constant of the exponential decaying envelop. The period of the fault $T_d = 1/6$s, which means the simulated fault is implemented at the frequency of 6Hz. The sampling time T is 0.0002s. k_o is the sample number where the first impact appears and here $k_o = 209$. The periodic impulsive fault signatures are illustrated in Fig. 5.2.

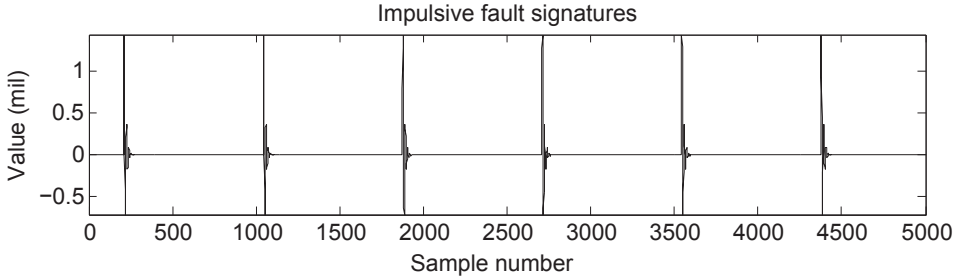

Figure 5.2: Impulsive fault signatures

The additive white Gaussian noise in this example is assumed to be at a low level to simulate the high SNR (signal to noise ratio) condition. By adding the impulsive fault signatures and the noise. Eq. (5.28) is changed to be the following Eq. (5.31).

$$y_m[k] = \sum_{i=1}^{m} A_i \cos(kT\omega_i + \phi_i) + d[k] + v_s[k], \tag{5.31}$$

where the sinusoidal components $\sum_{i=1}^{m} A_i \cos(kT\omega_i + \phi_i)$ are the same as those of Eq. (5.28). $d[k]$ is formulated in Eq. (5.29). v_s is a white noise, $v_s \sim \mathcal{N}(0, 4 \times 10^{-4})$. The fault detection results of the three methods are illustrated in Figure 5.3, where we can see that all three schemes can successfully detect the periodic characteristic impulsive fault signatures in this high SNR condition. It is worth pointing out that the 'signal' here is referred to the defect-related signal. The corresponding residual kurtosis values are shown in Table 5.2, from which it is clear that the kurtosis values rendered by all three methods increase dramatically from that of the raw signal. The increased kurtosis values show that all of the three methods indicate the existence of impulsive fault signatures.

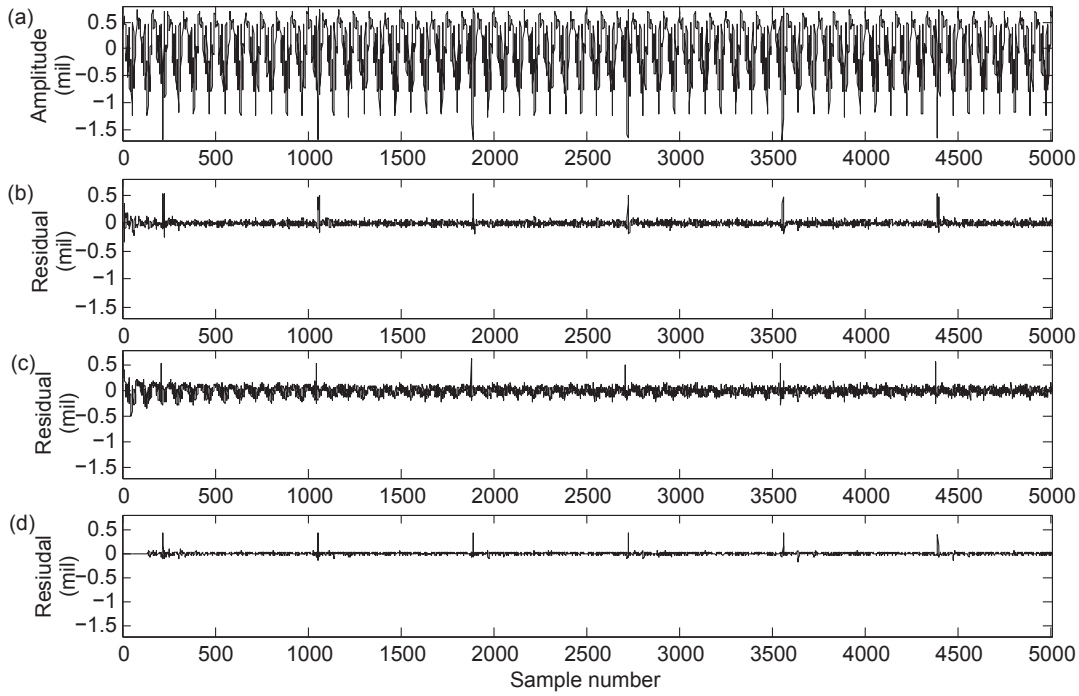

Figure 5.3: Fault detection comparison for faulty signal with high SNR: (a) simulated signal with fault (low noise); (b) residual of the $4th$ order MEDSS predictor; (c) residual of the $4th$ order regular SS predictor; (d) residual of the ARMED predictor.

Table 5.2: Kurtosis of the raw signals and the residuals in Example 2

	Raw signal	MEDSS	Regular SS	ARMED
Fault with high SNR	2.6771	41.7973	7.2264	102.4685

5.3.3 Example 3: Detection of impulsive fault signatures (low SNR)

To further model the low SNR condition for impulsive fault signatures detection, a relatively high noise is used in this example. Eq. (5.31) is changed to be the following Eq. (5.32).

$$y_m[k] = \sum_{i=1}^{m} A_i \cos(kT\omega_i + \phi_i) + d[k] + v_L[k], \tag{5.32}$$

where $v_L[k]$ represent a white noise sequence, $v_L \sim \mathcal{N}(0,\ 0.0144)$. The rest of the parameters are the same as those of Eq. (5.31).

The fault detection results are shown in Figure 5.4. When the MEDSS model or the ARMED method is used, all 6 impulsive signatures are detected. But the regular SS model cannot perform fault detection in this case, mainly due to the low SNR. The fault detection performance of the proposed MEDSS model is better than that of the ARMED method. From Figure 5.4 (d), we can see that, in addition to noises, the useful fault signature is also 'washed off' by the ARMED filter. The similar results are also obtained in kurtosis values, shown in Table 5.3. The kurtosis of the MEDSS residual is highly enhanced, while the other two methods show no obvious differences compared to the raw signal. Therefore, we can conclude that the advantage of the MEDSS filter is further illustrated in this example, where the fault signal is contaminated by strong noises.

Table 5.3: Kurtosis of the raw signal and the residuals in Example 3

	Raw signal	MEDSS	Regular SS	ARMED
Fault with low SNR	2.7235	20.9642	2.9485	3.3502

5.4 Application to Turbine Fault Diagnosis

The same steam turbine generator proposed in Chapter 4, Figure 4.8 is adopted here to demonstrate the feasibility of the proposed MEDSS method.

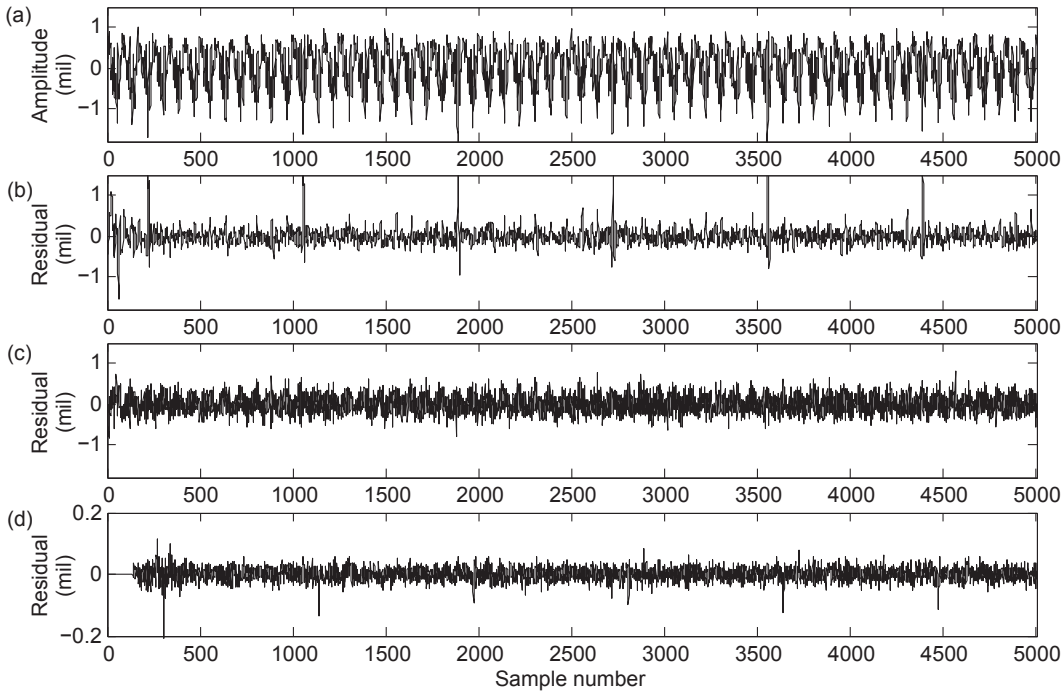

Figure 5.4: Fault detection comparison for faulty signal with low SNR: (a) simulated signal with fault (high noise); (b) residual of the $4th$ order MEDSS predictor; (c) residual of the $4th$ order regular SS predictor; (d) residual of the ARMED predictor. The y-scale of (d) is changed for clarity purposes and is one-fifth that of (a-c).

Here, we randomly select one dataset during the time period of August 10th, 2005 to January 15th, 2006 to conduct a more detailed analysis. First, the fault detection performance of the MEDSS method and the regular SS method are compared and the results are shown in Figure 5.5. Both the $4th$ order and the $6th$ order models are used to conduct fault detection. The results of the MEDSS models are shown in Figure 5.5(b) and (c), while the corresponding results of regular SS models are shown in Figure 5.5(d) and (e). We can find out that both methods are able to successfully detect the faults. However, the residuals from the regular SS method are contaminated by more noises compared to that from the MEDSS scheme.

To further illustrate the superiority of the MEDSS method in the low SNR condition, another data set is selected and the fault detection result is shown in Figure 5.6. In this data set, the 8 impulsive fault signatures can be clearly detected by the MEDSS method, while the fault signature is 'buried' in the noise in the regular SS residual. It is clear that

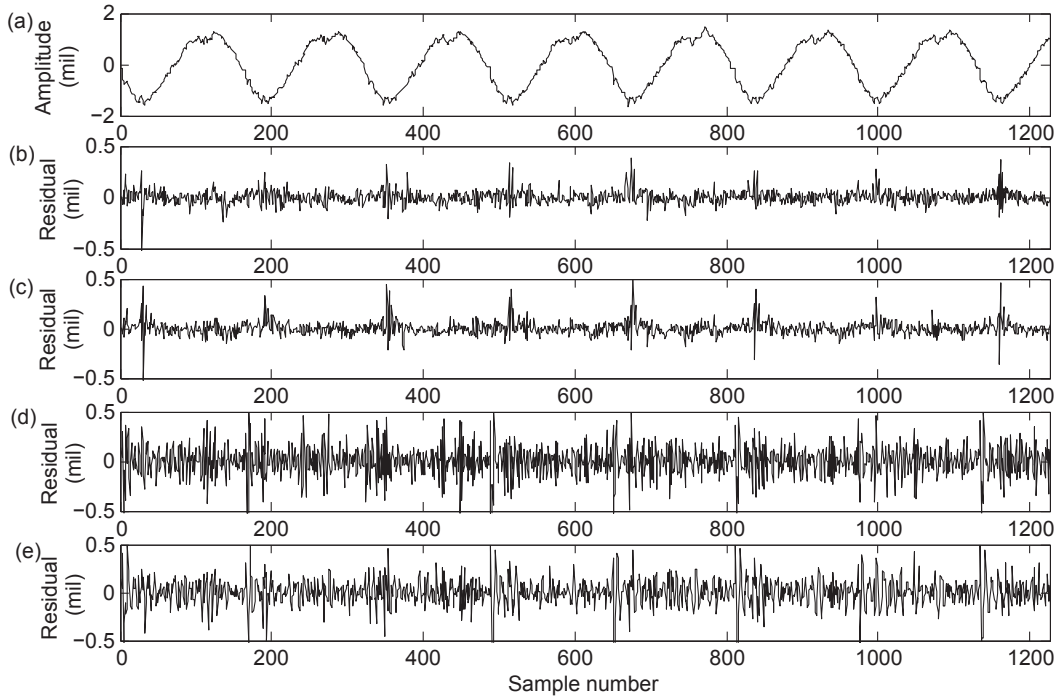

Figure 5.5: Fault detection of MEDSS vs regular SS method: (a) vibration (mil); (b) residual of the $4th$ order MEDSS predictor; (c) residual of the $6th$ order MEDSS predictor; (d) residual of the $4th$ order regular SS predictor; (e) residual of the $6th$ order regular SS predictor. The y-scales of (b-e) are changed for clarity purposes and are one-fourth that of (a).

the MEDSS can minimize the effect of the colored noise and enhance the fault information in the residual signal.

The fault detection performance of the MEDSS method and the ARMED method are compared in Figure 5.7. A $4th$ order and a $6th$ order MEDSS model are used to conduct the fault detection, and the corresponding results are shown in Figure 5.7 (b) and (c). In both cases, the MEDSS filter renders satisfactory fault detection results while the $6th$ order MEDSS performs better. The ARMED scheme is also implemented and the result is shown in Figure 5.7 (d). It can detect most of the fault impacts. However, it should be noted that the first impact fault within the first 50 samples cannot be detected. As we know, in the AR method, training (fitting) of the model in the first several iterations is needed, while the MEDSS algorithm adopts the sinusoidal characteristics and needs no history data to fit the model.

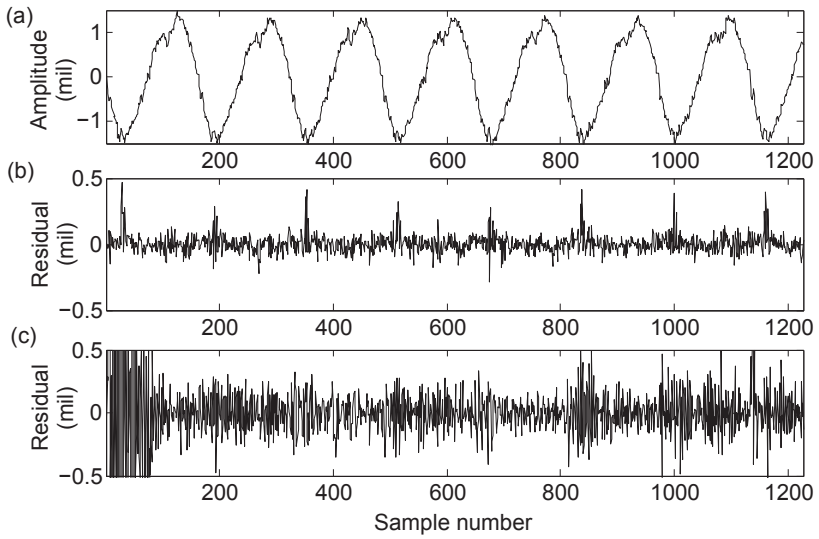

Figure 5.6: Fault detection of MEDSS vs regular SS method in low SNR condition: (a) vibration (mil); (b) residual of the $6th$ order MEDSS predictor; (c) residual of the $6th$ order regular SS predictor. The y-scales of (b-c) are changed for clarity purpose and are one-half that of (a).

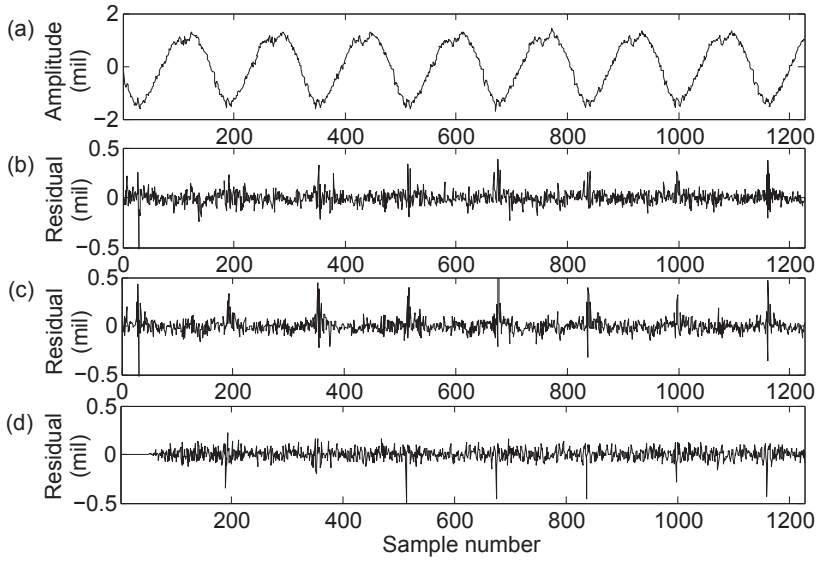

Figure 5.7: Fault detection of MEDSS vs ARMED method: (a) vibration (mil); (b) residual of the $4th$ order MEDSS predictor; (c) residual of the $6th$ order MEDSS predictor; (d) residual of the ARMED predictor. The y-scales of (b-d) are changed for clarity purpose and are one-fourth that of (a).

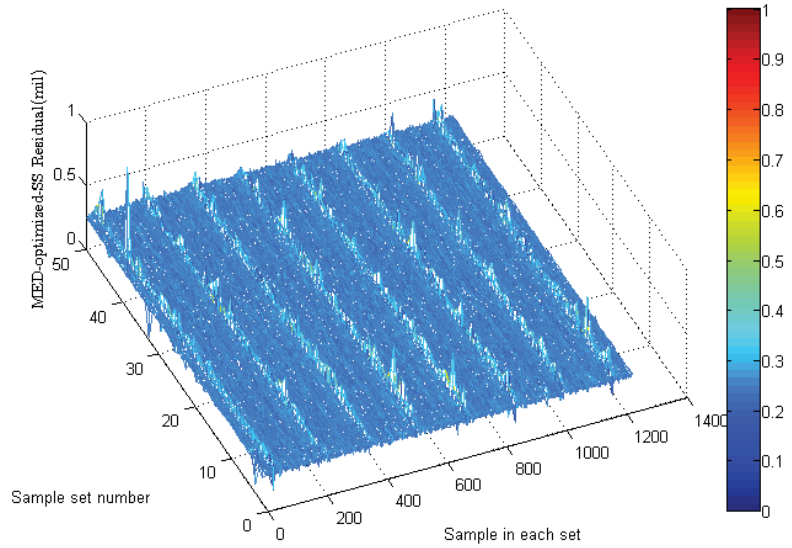

Figure 5.8: 3D plot of the residual of MEDSS predictor for 50 sample sets.

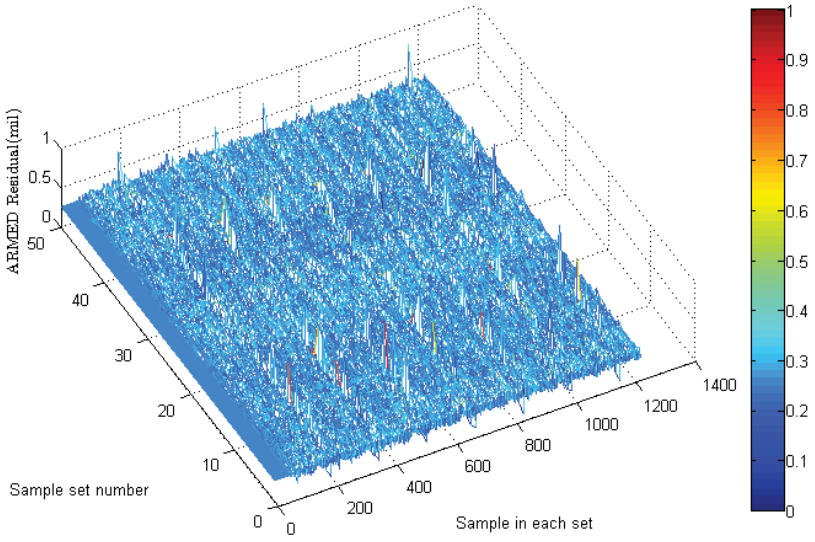

Figure 5.9: 3D plot of the residual of ARMED predictor for 50 sample sets.

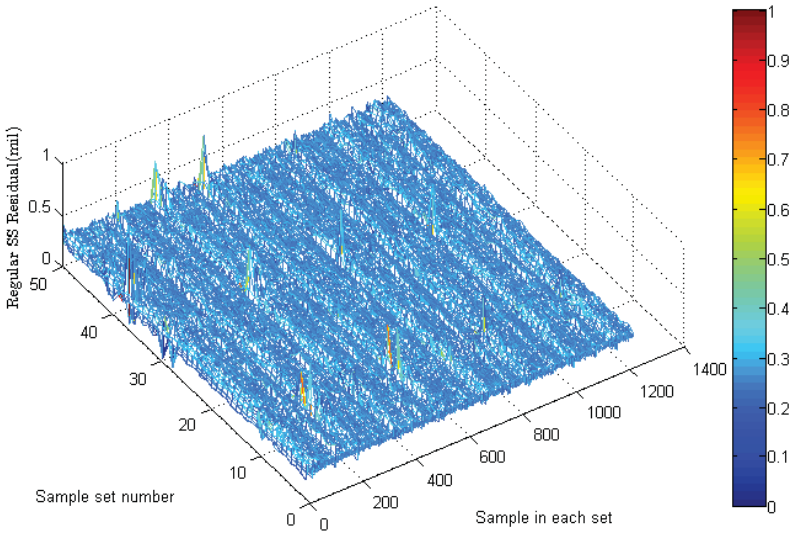

Figure 5.10: 3D plot of the residual of regular SS predictor for 50 sample sets.

Finally, in this case study, 50 datasets are tested using the three methods. The results are plotted to illustrate the detection performance in terms of rate of correct detection (or the rate of missing detection). The fault detection results of the MEDSS method are given in Figure 5.8. It is clear that the 8 impulsive fault signatures are detected in all 50 sample sets, thereby indicating an extremely high rate of detection. The results of the ARMED and regular SS methods are shown in Figure 5.9 and 5.10, respectively. We can see that the ARMED method can detect 7 faults in most of the datasets. However, the impulsive signatures between the $30th$ and the $40th$ sample sets are vague. The regular SS method can only detect a few fault impulses in some of the data sets.

5.5 Conclusion

In this chapter, an MEDSS data-driven model is proposed to improve the fault diagnosis performance of the regular SS filter. Firstly, we developed a state space form of the MEDSS filter, which can extract the nominal vibration signals from background noise and faults. Then, the system matrix of the MEDSS model is adaptively estimated using a time-weighted-error Kalman filter. Base on the identified model, the MEDSS model is used as a one-step predictor to generate the residual signal. Fault diagnosis can be realized based on the residual. Three simulation examples of fault-free, fault with high SNR, and fault with low SNR are provided to demonstrate the fault detection performance of the proposed method. Finally, the proposed MEDSS method is applied in a case study of

steam turbine rotor-stator rubbing fault diagnosis. For comparison, the regular SS method and the ARMED method are also implemented and tested in the simulation study. The MEDSS model has demonstrated superior performance over the regular SS method and it also shows comparable or even better performance than the ARMED method in the simulation examples. Specifically, the MEDSS model has shown potential in effectively detecting characteristic impulsive fault signatures in rotating machines, especially in the low SNR cases. In the future work, the stability of the proposed MEDSS filter can be studied.

Chapter 6

Conclusions and Future Work

6.1 Conclusions

In this thesis, adaptive model-based fault detection and diagnosis (FDD) and fault-tolerant control (FTC) are studied. The objective is to investigate and develop adaptive approaches to achieve better FDD and FTC performances for practical applications. The results of this research are further summarized as follows:

- In chapter 2, the fault- tolerant shape control (FTSC) problem for nonlinear and non-Gaussian stochastic distribution system is studied. An innovative adaptive observer-based fault estimation technique is firstly proposed for a stochastic distribution system with time-varying LOCE faults. Simulations under both fault-free and LOCE fault conditions validate the effectiveness of FDD in the unified framework. Then, an observer-based fault-tolerant shape controller is developed. Simulation results demonstrate that the proposed scheme can produce accurate estimation for time-varying LOCE faults, and in addition, optimized control performance can be achieved. Further, an application example of soil particle gradation control demonstrates the feasibility and effectiveness of the proposed adaptive fault estimation and FTSC approach for particle size distribution (PSD) system shape control in geotechnical processes.

- In chapter 3, the FTSC problem for PSD process under simultaneous actuator and sensor faults is researched. First, time-varying actuator and sensor faults are simultaneously estimated using a designed adaptive observer. Then, an FTSC scheme is proposed using virtual actuator and virtual sensor techniques based on estimated

faults. Simulation results for emulsion polymerization show that the proposed FTSC scheme can estimate the time-varying actuator and sensor faults simultaneously and reach a satisfactory tracking performance.

- In Chapter 4, a sinusoidal synthesis based adaptive tracking (SSBAT) fault diagnosis approach is proposed. An adaptive data-driven model is constructed based on the sinusoidal structure of the vibration signals. The utilization of physical properties into data-driven model transforms the nonlinear problem into a linear adaptive problem based on the time-frequency characteristics of sinusoids. Identified using time-series vibration data, the model then operates as an adaptive predictor for FDD design. Three simulation examples are performed to illustrate the strong SSBAT tracking ability, parameter convergence, and fault detection performance, respectively. In addition, a successful practical application to a steam turbine fault detection is also presented.

- In Chapter 5, a minimum entropy deconvolution sinusoidal synthesis (MEDSS) model is proposed to improve the fault detection performance of the regular SS filter. First, a state space form of the MEDSS filter is developed, which can extract the nominal vibration signals from background noise and faults. Then, system matrices of the MEDSS model are adaptively estimated using a time-weighted-error Kalman filter. Based on the identified model, the MEDSS filter is used as a one-step predictor to generate the residual signal between the filtered and the measured signal. Fault detection is further conducted based on the residual. Three simulation examples of fault-free, fault with high SNR, and fault with low SNR are provided to demonstrate the fault detection performance of the proposed method. The proposed MEDSS method is also applied in the steam turbine rotor-stator rubbing fault detection to demonstrate the enhanced performance.

6.2 Future Work

- Explicit analytical system models for SDC systems are assumed to be known in this thesis. However, SDC systems are generally complex and accurate analytical models are hard to derive. In this case, data-driven model based FDD and FTC can be further developed for practical applications.

- The SSBAT and MEDSS methods proposed in this thesis are currently limited to detecting impact faults like rotor rubbing, bearing inner/outer race faults, and various

gear tooth faults. In future work, these two methods can be extended to more general types of impact faults.

- In this research, a data-driven model incorporating physical properties is used to perform FDD. While an analytical rotating machine model can also be developed using physical principles with an adaptive data-driven based critical parameter identification structure, for more sophisticated FDD design.

- Considering multiple process variables, multivariate data fusion, and machine learning techniques can be applied. These techniques can relax the dependency of fault diagnostic methods on precise system modeling while maintaining the desired FDD performance.

Bibliography

[1] R. Isermann, "Supervision, fault-detection and fault-diagnosis methods–an introduction," *Control engineering practice*, vol. 5, no. 5, pp. 639–652, 1997.

[2] S. X. Ding, *Data-driven design of fault diagnosis and fault-tolerant control systems*. Springer, 2014.

[3] S. Ding, *Model-based fault diagnosis techniques: design schemes, algorithms, and tools*. Springer Science & Business Media, 2008.

[4] M. Blanke, M. Kinnaert, J. Lunze, M. Staroswiecki, and J. Schröder, *Diagnosis and fault-tolerant control*. Springer, 2006, vol. 2.

[5] J. Chen and R. J. Patton, *Robust model-based fault diagnosis for dynamic systems*. Springer Science & Business Media, 2012, vol. 3.

[6] R. V. Beard, "Failure accomodation in linear systems through self-reorganization." Ph.D. dissertation, Massachusetts Institute of Technology, 1971.

[7] H. L. Jones, "Failure detection in linear systems." Ph.D. dissertation, Massachusetts Institute of Technology, 1973.

[8] P. Frank, S. Ding, and T. Marcu, "Model-based fault diagnosis in technical processes," *Transactions of the Institute of Measurement and Control*, vol. 22, no. 1, pp. 57–101, 2000.

[9] E. Chow and A. Willsky, "Analytical redundancy and the design of robust failure detection systems," *IEEE Transactions on Automatic control*, vol. 29, no. 7, pp. 603–614, 1984.

[10] R. Isermann, "Process fault detection based on modeling and estimation methodsa survey," *Automatica*, vol. 20, no. 4, pp. 387–404, 1984.

[11] R. J. Patton, P. M. Frank, and R. N. Clark, *Issues of fault diagnosis for dynamic systems*. Springer Science & Business Media, 2013.

[12] P. M. Frank and X. Ding, "Survey of robust residual generation and evaluation methods in observer-based fault detection systems," *Journal of process control*, vol. 7, no. 6, pp. 403–424, 1997.

[13] P. M. Frank and R. Seliger, "Fault detection and isolation in automatic processes," *C. Leondes (ed.), Control and dynamic systems*, vol. 49, pp. 241–287, 2012.

[14] R. Patton and J. Chen, "Robust fault detection using eigenstructure assignment: a tutorial consideration and some new results," in *Decision and Control, 1991., Proceedings of the 30th IEEE Conference on*. IEEE, 1991, pp. 2242–2247.

[15] N. Viswanadham, V. Sarma, and M. G. Singh, "Reliability of computer and control systems," 1987.

[16] A. Emami-Naeini, M. M. Akhter, and S. M. Rock, "Effect of model uncertainty on failure detection: the threshold selector," *IEEE Transactions on Automatic Control*, vol. 33, no. 12, pp. 1106–1115, 1988.

[17] X. Ding, L. Guo, and P. Frank, "A frequency domain approach to fault detection of uncertain dynamic systems," in *Decision and Control, 1993., Proceedings of the 32nd IEEE Conference on*. IEEE, 1993, pp. 1722–1727.

[18] X. Ding, P. Frank, and L. Guo, "Fault detection via adaptive observers based on orthogonal functions," *Advanced Information Processing in Automatic Control (AIPAC'89)*, p. 95, 2014.

[19] P. M. Frank, "On-line fault detection in uncertain nonlinear systems using diagnostic observers: a survey," *International journal of systems science*, vol. 25, no. 12, pp. 2129–2154, 1994.

[20] P. Frank, X. Ding, and J. Wochnik, "Model based fault detection in diesel-hydraulically driven industrial trucks," in *American Control Conference, 1991*. IEEE, 1991, pp. 1528–1533.

[21] C. Aubrun, D. Sauter, H. Noura, and M. Robert, "Fault diagnosis and reconfiguration of systems using fuzzy logic: application to a thermal plant," *International journal of systems science*, vol. 24, no. 10, pp. 1945–1954, 1993.

[22] W. Ge and C.-Z. FANG, "Detection of faulty components via robust observation," *International Journal of Control*, vol. 47, no. 2, pp. 581–599, 1988.

[23] S. Simani, "Data-driven design of a PI fuzzy controller for a wind turbine simulated model," *IFAC Proceedings Volumes*, vol. 45, no. 3, pp. 667–672, 2012.

[24] H. Badihi, Y. Zhang, and H. Hong, "Fuzzy gain-scheduled active fault-tolerant control of a wind turbine," *Journal of the Franklin Institute*, vol. 351, no. 7, pp. 3677–3706, 2014.

[25] S. Ding, P. Zhang, A. Naik, E. Ding, and B. Huang, "Subspace method aided data-driven design of fault detection and isolation systems," *Journal of process control*, vol. 19, no. 9, pp. 1496–1510, 2009.

[26] R. Isermann, *Fault-diagnosis systems: an introduction from fault detection to fault tolerance*. Springer Science & Business Media, 2006.

[27] J. Liu, W. Luo, X. Yang, and L. Wu, "Robust model-based fault diagnosis for pem fuel cell air-feed system," *IEEE Transactions on Industrial Electronics*, vol. 63, no. 5, pp. 3261–3270, 2016.

[28] L. Wu, W. X. Zheng, and H. Gao, "Dissipativity-based sliding mode control of switched stochastic systems," *IEEE Transactions on Automatic Control*, vol. 58, no. 3, pp. 785–791, 2013.

[29] J. Liu, S. Laghrouche, M. Harmouche, and M. Wack, "Adaptive-gain second-order sliding mode observer design for switching power converters," *Control Engineering Practice*, vol. 30, pp. 124–131, 2014.

[30] J. Liu, S. Laghrouche, and M. Wack, "Observer-based higher order sliding mode control of power factor in three-phase ac/dc converter for hybrid electric vehicle applications," *International Journal of Control*, vol. 87, no. 6, pp. 1117–1130, 2014.

[31] K. Zhang, B. Jiang, V. Cocquempot *et al.*, "Adaptive observer-based fast fault estimation," *International Journal of Control Automation and Systems*, vol. 6, no. 3, p. 320, 2008.

[32] K. Zhang, B. Jiang, and P. Shi, "Fast fault estimation and accommodation for dynamical systems," *IET Control Theory & Applications*, vol. 3, no. 2, pp. 189–199, 2009.

[33] M. Liu, D. W. Ho, and P. Shi, "Adaptive fault-tolerant compensation control for markovian jump systems with mismatched external disturbance," *Automatica*, vol. 58, pp. 5–14, 2015.

[34] X. Zhao, P. Shi, X. Zheng, and L. Zhang, "Adaptive tracking control for switched stochastic nonlinear systems with unknown actuator dead-zone," *Automatica*, vol. 60, pp. 193–200, 2015.

[35] D. Koenig, "Unknown input proportional multiple-integral observer design for linear descriptor systems: application to state and fault estimation," *IEEE Transactions on Automatic control*, vol. 50, no. 2, pp. 212–217, 2005.

[36] Q. P. Ha and H. Trinh, "State and input simultaneous estimation for a class of nonlinear systems," *Automatica*, vol. 40, no. 10, pp. 1779–1785, 2004.

[37] Z. Gao and H. Wang, "Descriptor observer approaches for multivariable systems with measurement noises and application in fault detection and diagnosis," *Systems & Control Letters*, vol. 55, no. 4, pp. 304–313, 2006.

[38] Z. Gao and S. Ding, "Sensor fault reconstruction and sensor compensation for a class of nonlinear state-space systems via a descriptor system approach," *IET Control Theory & Applications*, vol. 1, no. 3, pp. 578–585, 2007.

[39] K. Helland, H. E. Berntsen, O. S. Borgen, and H. Martens, "Recursive algorithm for partial least squares regression," *Chemometrics and intelligent laboratory systems*, vol. 14, no. 1-3, pp. 129–137, 1992.

[40] S. J. Qin, "Recursive pls algorithms for adaptive data modeling," *Computers & Chemical Engineering*, vol. 22, no. 4, pp. 503–514, 1998.

[41] C. Wei *et al.*, "Adaptive prediction by least squares predictors in stochastic regression models with applications to time series," *The Annals of Statistics*, vol. 15, no. 4, pp. 1667–1682, 1987.

[42] G. Bastin and M. Gevers, "Stable adaptive observers for nonlinear time-varying systems," *IEEE Transactions on Automatic Control*, vol. 33, no. 7, pp. 650–658, 1988.

[43] R. Marino and P. Tomei, "Global adaptive output-feedback control of nonlinear systems. i. linear parameterization," *IEEE Transactions on Automatic Control*, vol. 38, no. 1, pp. 17–32, 1993.

[44] H. Wang and S. Daley, "Actuator fault diagnosis: an adaptive observer-based technique," *IEEE transactions on Automatic Control*, vol. 41, no. 7, pp. 1073–1078, 1996.

[45] H. Wang, Z. J. Huang, and S. Daley, "On the use of adaptive updating rules for actuator and sensor fault diagnosis," *Automatica*, vol. 33, no. 2, pp. 217–225, 1997.

[46] A. Xu and Q. Zhang, "Fault detection and isolation based on adaptive observers for linear time varying systems," *IFAC Proceedings Volumes*, vol. 35, no. 1, pp. 47–52, 2002.

[47] B. Jiang, M. Staroswiecki, and V. Cocquempot, "Fault diagnosis based on adaptive observer for a class of non-linear systems with unknown parameters," *International Journal of Control*, vol. 77, no. 4, pp. 367–383, 2004.

[48] B. Jiang and F. N. Chowdhury, "Parameter fault detection and estimation of a class of nonlinear systems using observers," *Journal of the Franklin Institute*, vol. 342, no. 7, pp. 725–736, 2005.

[49] R. Shahnazi and Q. Zhao, "Adaptive fuzzy descriptor sliding mode observer-based sensor fault estimation for uncertain nonlinear systems," *Asian Journal of Control*, 2015.

[50] M. Defoort, K. C. Veluvolu, J. J. Rath, and M. Djemai, "Adaptive sensor and actuator fault estimation for a class of uncertain lipschitz nonlinear systems," *International Journal of Adaptive Control and Signal Processing*, vol. 30, no. 2, pp. 271–283, 2016.

[51] B. Jiang, K. Zhang, and P. Shi, "Integrated fault estimation and accommodation design for discrete-time takagi–sugeno fuzzy systems with actuator faults," *IEEE Transactions on Fuzzy Systems*, vol. 19, no. 2, pp. 291–304, 2011.

[52] S.-P. He, "Fault estimation for ts fuzzy markovian jumping systems based on the adaptive observer," *International Journal of Control, Automation and Systems*, vol. 12, no. 5, pp. 977–985, 2014.

[53] D. Lu, X. Li, J. Liu, and G. Zeng, "Fault estimation and fault tolerant control of markovian jump system with mixed mode-dependent time-varying delays via the adaptive observer approach," *Journal of Dynamic Systems, Measurement, and Control*, 2016.

[54] K. Zhang, B. Jiang, and V. Cocquempot, "Adaptive technique-based distributed fault estimation observer design for multi-agent systems with directed graphs," *IET Control Theory & Applications*, vol. 9, no. 18, pp. 2619–2625, 2015.

[55] T. Li and Y. Zhang, "Fault detection and diagnosis for stochastic systems via output pdfs," *Journal of the Franklin Institute*, vol. 348, no. 6, pp. 1140–1152, 2011.

[56] H. Wang, *Bounded dynamic stochastic systems: modelling and control*. Springer Science & Business Media, 2012.

[57] L. Guo and H. Wang, *Stochastic distribution control system design: a convex optimization approach*. Springer Science & Business Media, 2010.

[58] T. Li, G. Li, and Q. Zhao, "Adaptive fault-tolerant stochastic shape control with application to particle distribution control," *IEEE Transactions on Systems, Man, and Cybernetics: Systems*, vol. 45, no. 12, pp. 1592–1604, 2015.

[59] G. Li and Q. Zhao, "Simultaneous actuator and sensor fault estimation for adaptive stochastic shape control," in *American Control Conference (ACC), 2016*. IEEE, 2016, pp. 3868–3873.

[60] T. Li, G. Li, and Q. Zhao, "Fault tolerant shape control for output pdfs tracking of stochastic distribution systems," in *American Control Conference (ACC), 2014*. IEEE, 2014, pp. 1945–1950.

[61] G. Li and Q. Zhao, "Robust adaptive fault estimation for nonlinear particulate process systems," in *Electrical and Computer Engineering (CCECE), 2016 IEEE Canadian Conference on*. IEEE, 2016, pp. 1–4.

[62] C. Dodson and H. Wang, "Iterative approximation of statistical distributions and relation to information geometry," *Statistical inference for stochastic processes*, vol. 4, no. 3, pp. 307–318, 2001.

[63] M. G. Forbes, J. F. Forbes, and M. Guay, "Regulatory control design for stochastic processes: shaping the probability density function," in *American Control Conference, 2003. Proceedings of the 2003*, vol. 5. IEEE, 2003, pp. 3998–4003.

[64] L. Yao, J. Qin, A. Wang, and H. Wang, "Brief paper-fault diagnosis and fault-tolerant control for non-gaussian non-linear stochastic systems using a rational square-root approximation model," *Control Theory & Applications, IET*, vol. 7, no. 1, pp. 116–124, 2013.

[65] A. F. Santos, F. M. Silva, M. K. Lenzi, and J. C. Pinto, "Monitoring and control of polymerization reactors using nir spectroscopy," *Polymer-Plastics Technology and Engineering*, vol. 44, no. 1, pp. 1–61, 2005.

[66] D. Winn and M. F. Doherty, "Modeling crystal shapes of organic materials grown from solution," *AIChE journal*, vol. 46, no. 7, pp. 1348–1367, 2000.

[67] T. Crowley, E. Meadows, A. Kostoulas, and F. Doyle III, "Control of particle size distribution in semibatch emulsion polymerization by surfactant addition," *J. Process Control*, vol. 10, pp. 419–432, 2000.

[68] P. Daoutidis and M. A. Henson, "Dynamics and control of cell populations in continuous bioreactors," in *AIChE Symposium Series*, vol. 326, 2002.

[69] H. Wang and W. Lin, "Applying observer based fdi techniques to detect faults in dynamic and bounded stochastic distributions," *International Journal of Control*, vol. 73, no. 15, pp. 1424–1436, 2000.

[70] L. Guo and H. Wang, "Fault detection and diagnosis for general stochastic systems using b-spline expansions and nonlinear filters," *IEEE Transactions on Circuits and Systems I: Regular Papers*, vol. 52, no. 8, pp. 1644–1652, 2005.

[71] L. Guo, Y.-M. Zhang, H. Wang, and J.-C. Fang, "Observer-based optimal fault detection and diagnosis using conditional probability distributions," *IEEE Transactions on Signal Processing*, vol. 54, no. 10, pp. 3712–3719, 2006.

[72] T. Li, Y. Yi, L. Guo, and H. Wang, "Delay-dependent fault detection and diagnosis using b-spline neural networks and nonlinear filters for time-delay stochastic systems," *Neural Computing and Applications*, vol. 17, no. 4, pp. 405–411, 2008.

[73] L. Yao, J. Qin, H. Wang, and B. Jiang, "Design of new fault diagnosis and fault tolerant control scheme for non-gaussian singular stochastic distribution systems," *Automatica*, vol. 48, no. 9, pp. 2305–2313, 2012.

[74] L. Yao, J. Qin, A. Wang, and H. Wang, "Brief paper-fault diagnosis and fault-tolerant control for non-gaussian non-linear stochastic systems using a rational square-root approximation model," *IET Control Theory & Applications*, vol. 7, no. 1, pp. 116–124, 2013.

[75] G. Genta, *Dynamics of rotating systems*. Springer, 2007.

[76] M. L. Adams, *Rotating Machinery Vibration: From Analysis to Troubleshooting*, 2nd ed. CRC Press, Dec 2009.

[77] T. Barszcz and R. B. Randall, "Application of spectral kurtosis for detection of a tooth crack in the planetary gear of a wind turbine," *Mechanical Systems and Signal Processing*, vol. 23, no. 4, pp. 1352–1365, 2009.

[78] W. Wang and A. K. Wong, "Autoregressive model-based gear fault diagnosis," *Journal of Vibration and Acoustics*, vol. 124, no. 2, pp. 172–179, 2002.

[79] J. Goodwin, *Dynamics of Rotor-bearing Systems*. Unwin Hyman, 1989. [Online]. Available: http://books.google.ca/books?id=L1awAAAAIAAJ

[80] A. D. Dimarogonas, S. A. Paipetis, and T. G. Chondros, *Analytical Methods in Rotor Dynamics*, 2nd ed. Springer, Feb 2013.

[81] P. H. Mathuria, A. Sainagar, M. G. Road, F. Advisor, and P. D. N. Manik, "Lateral natural frequency of a shaft rotor system by the transfer matrix method."

[82] S. Dunkerley, *On the Whirling and Vibration of Shafts*. Harrison and Sons, 1894. [Online]. Available: http://books.google.ca/books?id=MLJJYAAACAAJ

[83] G. Li, R. Pan, and Q. Zhao, "Robust imbalance fault estimation of a flexible rotor system," in *American Control Conference (ACC), 2016*. IEEE, 2016, pp. 6703–6708.

[84] M. May, N. Sepehri, and W. Kinsner, "Hydraulic actuator internal leakage detection using cross-correlation time series analysis," in *ASME/BATH 2014 Symposium on Fluid Power and Motion Control*. American Society of Mechanical Engineers, 2014, pp. V001T01A003–V001T01A003.

[85] H. Endo and R. Randall, "Enhancement of autoregressive model based gear tooth fault detection technique by the use of minimum entropy deconvolution filter," *Mechanical Systems and Signal Processing*, vol. 21, no. 2, pp. 906–919, 2007.

[86] W. Wang, "An evaluation of some emerging techniques for gear fault detection," *Structural Health Monitoring*, vol. 2, no. 3, pp. 225–242, 2003.

[87] K. Fyfe and E. Munck, "Analysis of computed order tracking," *Mechanical Systems and Signal Processing*, vol. 11, no. 2, pp. 187–205, 1997.

[88] K. Bossley, R. Mckendrick, C. Harris, and C. Mercer, "Hybrid computed order tracking," *Mechanical systems and signal processing*, vol. 13, no. 4, pp. 627–641, 1999.

[89] H. Vold and J. Leuridan, "High resolution order tracking at extreme slew rates, using kalman tracking filters," SAE Technical Paper, Tech. Rep., 1993.

[90] H. Vold, M. Mains, and J. Blough, "Theoretical foundations for high performance order tracking with the vold-kalman tracking filter," SAE Technical Paper, Tech. Rep., 1997.

[91] M.-C. Pan and Y.-F. Lin, "Further exploration of vold–kalman-filtering order tracking with shaft-speed information-i: theoretical part, numerical implementation and parameter investigations," *Mechanical systems and signal processing*, vol. 20, no. 5, pp. 1134–1154, 2006.

[92] S. Qian, "Gabor expansion for order tracking," *Sound and Vibration*, vol. 37, no. 6, pp. 18–23, 2003.

[93] G. C. Goodwin and K. S. Sin, *Adaptive filtering prediction and control*. Courier Corporation, 2014.

[94] G. Li, G. L. McDonald, and Q. Zhao, "Sinusoidal synthesis based adaptive tracking for rotating machinery fault detection," *Mechanical Systems and Signal Processing*, vol. 83, pp. 356–370, 2017.

[95] G. Li and Q. Zhao, "Minimum entropy deconvolution optimized sinusoidal synthesis and its application to vibration based fault detection," *Journal of Sound and Vibration*, vol. 390, pp. 218–231, 2017.

[96] M. Konert and J. Vandenberghe, "Comparison of laser grain size analysis with pipette and sieve analysis: a solution for the underestimation of the clay fraction," *Sedimentology*, vol. 44, no. 3, pp. 523–535, 1997.

[97] D. Shi, N. H. El-Farra, M. Li, P. Mhaskar, and P. D. Christofides, "Predictive control of particle size distribution in particulate processes," *Chemical Engineering Science*, vol. 61, no. 1, pp. 268–281, 2006.

[98] J. Zhou, H. Yue, and H. Wang, "Shaping of output pdf based on the rational square-root b-spline model," *ACTA Automatica Sinica*, vol. 31, no. 3, pp. 343–351, 2005.

[99] W. Yan and X. Li, "Mechanical response of a medium-fine-grained decomposed granite in hong kong," *Engineering geology*, vol. 129, pp. 1–8, 2012.

[100] A. Pertew, H. Marquez, and Q. Zhao, "Sampled-data stabilization of a class of nonlinear systems with application in robotics," *Journal of Dynamic Systems, Measurement, and Control*, vol. 131, no. 2, p. 021008, 2009.

[101] B. W. Silverman, *Density estimation for statistics and data analysis*. CRC press, 1986, vol. 26.

[102] D. Shi, N. H. El-Farra, M. Li, P. Mhaskar, and P. D. Christofides, "Predictive control of particle size distribution in particulate processes," *Chemical Engineering Science*, vol. 61, no. 1, pp. 268–281, 2006.

[103] M. A. Henson, "Distribution control of particulate systems based on population balance equation models," in *American Control Conference, 2003. Proceedings of the 2003*, vol. 5. IEEE, 2003, pp. 3967–3972.

[104] D. L. Boley, "Krylov space methods on state-space control models," *Circuits, Systems and Signal Processing*, vol. 13, no. 6, pp. 733–758, 1994.

[105] T.-J. Su and R. R. RAIG, "Model reduction and control of flexible structures using krylov vectors," *Journal of guidance, control, and dynamics*, vol. 14, no. 2, pp. 260–267, 1991.

[106] J. Zhang, A. K. Swain, and S. K. Nguang, "Simultaneous robust actuator and sensor fault estimation for uncertain non-linear lipschitz systems," *Control Theory & Applications, IET*, vol. 8, no. 14, pp. 1364–1374, 2014.

[107] F. J. Bejarano, M. Figueroa, J. Pacheco, and J. de Jesus Rubio, "Robust fault diagnosis of disturbed linear systems via a sliding mode high order differentiator," *International Journal of Control*, vol. 85, no. 6, pp. 648–659, 2012.

[108] L. Guo and H. Wang, *Stochastic distribution control system design: a convex optimization approach*. Springer Science & Business Media, 2010.

[109] M. Corless and J. Tu, "State and input estimation for a class of uncertain systems," *Automatica*, vol. 34, no. 6, pp. 757–764, 1998.

[110] J. Zhang, A. K. Swain, and S. K. Nguang, "Detection and isolation of incipient sensor faults for a class of uncertain non-linear systems," *Control Theory & Applications, IET*, vol. 6, no. 12, pp. 1870–1880, 2012.

[111] M. T. Dokucu, M.-J. Park, and F. J. Doyle, "Multi-rate model predictive control of particle size distribution in a semibatch emulsion copolymerization reactor," *Journal of Process Control*, vol. 18, no. 1, pp. 105–120, 2008.

[112] A. McCormick and A. Nandi, "Cyclostationarity in rotating machine vibrations," *Mechanical Systems and Signal Processing*, vol. 12, no. 2, pp. 225–242, 1998.

[113] M. E. Badaoui, F. Guillet, and J. Daniere, "New applications of the real cepstrum to gear signals, including definition of a robust fault indicator," *Mechanical Systems and Signal Processing*, vol. 18, no. 5, pp. 1031–1046, 2004.

[114] J. Antoni and R. Randall, "The spectral kurtosis: application to the vibratory surveillance and diagnostics of rotating machines," *Mechanical Systems and Signal Processing*, vol. 20, no. 2, pp. 308–331, 2006.

[115] A. S. Sait and Y. I. Sharaf-Eldeen, "A review of gearbox condition monitoring based on vibration analysis techniques diagnostics and prognostics," in *Rotating Machinery, Structural Health Monitoring, Shock and Vibration, Volume 5*, T. Proulx, Ed. Springer, 2011, pp. 307–324.

[116] C. Capdessus, M. Sidahmed, and J. Lacoume, "Cyclostationary processes: application in gear faults early diagnosis," *Mechanical Systems and Signal Processing*, vol. 14, no. 3, pp. 371–385, 2000.

[117] M. R. Bai, J. Jeng, and C. Chen, "Adaptive order tracking technique using recursive least-square algorithm," *Journal of vibration and acoustics*, vol. 124, no. 4, pp. 502–511, 2002.

[118] M.-C. Pan and C.-X. Wu, "Adaptive vold–kalman filtering order tracking," *Mechanical systems and signal processing*, vol. 21, no. 8, pp. 2957–2969, 2007.

[119] T.-C. Yeh and M.-C. Pan, "Online real-time monitoring system through using adaptive angular-velocity vkf order tracking," in *ASME 2012 International Design Engineering Technical Conferences and Computers and Information in Engineering Conference*. American Society of Mechanical Engineers, 2012, pp. 159–163.

[120] M. Bai, J. Huang, M. Hong, and F. Su, "Fault diagnosis of rotating machinery using an intelligent order tracking system," *Journal of Sound and Vibration*, vol. 280, no. 3, pp. 699–718, 2005.

[121] J.-D. Wu, Y.-H. Wang, P.-H. Chiang, and M. R. Bai, "A study of fault diagnosis in a scooter using adaptive order tracking technique and neural network," *Expert Systems with Applications*, vol. 36, no. 1, pp. 49–56, 2009.

[122] P. D. Samuel and D. J. Pines, "A review of vibration-based techniques for helicopter transmission diagnostics," *Journal of Sound and Vibration*, vol. 282, no. 1, pp. 475–508, 2005.

[123] A. Gerasimov, O. Morozov, E. Soldatov, and V. Fidelman, "Using the method of modified linear prediction for robust acoustic coding of speech," *Radiophysics and quantum electronics*, vol. 49, no. 7, pp. 535–539, 2006.

[124] E. George and M. Smith, "Generalized overlap-add sinusoidal modeling applied to quasi-harmonic tone synthesis," in *Applications of Signal Processing to Audio and Acoustics, IEEE Workshop*. IEEE, 1993, pp. 165–168.

[125] Z. Man, W. Wang, S. Khoo, and J. Yin, "Optimal sinusoidal modelling of gear mesh vibration signals for gear diagnosis and prognosis," *Mechanical Systems and Signal Processing*, vol. 33, pp. 256–274, 2012.

[126] X. Xia, "Global frequency estimation using adaptive identifiers," *IEEE Transactions on Automatic Control*, vol. 47, no. 7, p. 1189, 2002.

[127] M. Hou, "Estimation of sinusoidal frequencies and amplitudes using adaptive identifier and observer," *IEEE transactions on automatic control*, vol. 52, no. 3, pp. 493–499, 2007.

[128] S. Yang and Q. Zhao, "Real-time frequency estimation of sinusoids with low-frequency disturbances," in *American Control Conference (ACC), 2011*. IEEE, 2011, pp. 4275–4280.

[129] G. McDonald and Q. Zhao, "Model-based adaptive frequency estimator for gear crack fault detection," in *American Control Conference (ACC), 2011*. IEEE, 2011, pp. 792–797.

[130] S. Yang and Q. Zhao, "Real-time frequency estimation for sinusoidal signals with application to robust fault detection," *International Journal of Adaptive Control and Signal Processing*, vol. 27, no. 5, pp. 386–399, 2013.

[131] R. McAulay and T. F. Quatieri, "Speech analysis/synthesis based on a sinusoidal representation," *IEEE Transactions on Acoustics, Speech and Signal Processing*, vol. 34, no. 4, pp. 744–754, 1986.

[132] G. L. McDonald, Q. Zhao, and M. J. Zuo, "Maximum correlated kurtosis deconvolution and application on gear tooth chip fault detection," *Mechanical Systems and Signal Processing*, vol. 33, pp. 237–255, 2012.

[133] B. A. Francis and W. M. Wonham, "The internal model principle of control theory," *Automatica*, vol. 12, no. 5, pp. 457–465, 1976.

[134] K. Ogata, *Discrete-time control systems*. Prentice Hall Englewood Cliffs, NJ, 1995, vol. 2.

[135] H. Ma and K.-Y. Lum, "Adaptive estimation and control for systems with parametric and nonparametric uncertainties," *Adaptive Control*, pp. 15–64, 2008.

[136] S. Sastry and M. Bodson, *Adaptive control: stability, convergence and robustness*. Courier Dover Publications, 2011.

[137] S. M. Kay, *Modern spectral estimation*. Pearson Education India, 1988.

[138] Y. Yang and Q. Zhao, "Generator thermal sensitivity analysis with support vector regression," in *American Control Conference (ACC), 2010*, June 2010, pp. 944–949.

[139] O. Seryasat, M. Shoorehdeli, F. Honarvar, and A. Rahmani, "Multi-fault diagnosis of ball bearing using fft, wavelet energy entropy mean and root mean square (rms)," in *2010 IEEE International Conference on Systems Man and Cybernetics (SMC)*. IEEE, 2010, pp. 4295–4299.

[140] G. Mack and V. Jain, "Speech parameter estimation by time-weighted-error kalman filtering," *Acoustics, Speech and Signal Processing, IEEE Transactions on*, vol. 31, no. 5, pp. 1300–1303, 1983.

[141] T. Yang, J. Lee, K. Y. Lee, and K.-M. Sung, "On robust kalman filtering with forgetting factor for sequential speech analysis," *Signal Processing*, vol. 63, no. 2, pp. 151–156, 1997.

[142] R. Bighamian, H. R. Mirdamadi, and J. O. Hahn, "Damage identification in collocated structural systems using structural markov parameters," *Journal of Dynamic Systems, Measurement, and Control*, vol. 137, no. 4, p. 041001, 2015.

[143] R. A. Wiggins, "Minimum entropy deconvolution," *Geoexploration*, vol. 16, no. 1, pp. 21–35, 1978.

[144] H. Yang, J. Mathew, and L. Ma, "Vibration feature extraction techniques for fault diagnosis of rotating machinery : a literature survey," in *Asia-Pacific Vibration Conference*, Gold Coast, Australia, 2003, pp. 801–807.

[145] G. L. McDonald and Q. Zhao, "Multipoint optimal minimum entropy deconvolution and convolution fix: Application to vibration fault detection," *Mechanical Systems and Signal Processing*, vol. 82, pp. 461–477, 2017.

[146] G. Welch and G. Bishop, "An introduction to the kalman filter. 2006," *University of North Carolina: Chapel Hill, North Carolina, US*, 2006.

[147] T. J. Tarn and J. Zaborszky, "A practical nondiverging filter," *AIAA Journal*, vol. 8, no. 6, pp. 1127–1133, 1970.

[148] R. Randall, N. Sawalhi, and M. Coats, "A comparison of methods for separation of deterministic and random signals," *International Journal of Condition Monitoring*, vol. 1, no. 1, pp. 11–19, 2011.